



# Transport of TiO<sub>2</sub> nanoparticles in saturated and unsaturated porous media: experiments and modeling

Ivan Toloni

## ► To cite this version:

Ivan Toloni. Transport of TiO<sub>2</sub> nanoparticles in saturated and unsaturated porous media: experiments and modeling. Geophysics [physics.geo-ph]. Université de Strasbourg, 2015. English. NNT: 2015STRAH018 . tel-01291564

**HAL Id: tel-01291564**

**<https://theses.hal.science/tel-01291564>**

Submitted on 21 Mar 2016

**HAL** is a multi-disciplinary open access archive for the deposit and dissemination of scientific research documents, whether they are published or not. The documents may come from teaching and research institutions in France or abroad, or from public or private research centers.

L'archive ouverte pluridisciplinaire **HAL**, est destinée au dépôt et à la diffusion de documents scientifiques de niveau recherche, publiés ou non, émanant des établissements d'enseignement et de recherche français ou étrangers, des laboratoires publics ou privés.

*ÉCOLE DOCTORALE*

*SCIENCES DE LA TERRE ET ENVIRONNEMENT*

Laboratoire d'Hydrologie et de Géochimie de Strasbourg

**THÈSE** présentée par :

**Ivan TOLONI**

soutenue le : **23 Novembre 2015**

pour obtenir le grade de : **Docteur de l'université de Strasbourg**

Discipline : Géosciences

**Transport de nanoparticules de  $\text{TiO}_2$  en  
milieux poreux saturés et non saturés :  
expériences et modélisation**

**THÈSE dirigée par :**

**M ACKERER Philippe**  
**M LEHMANN François**

DR CNRS, LHYGES Strasbourg  
Pr, Université de Strasbourg

**RAPPORTEURS :**

**M GUADAGNINI Alberto**  
**M MARTINS Jean**

Pr, Politecnico di Milano  
DR CNRS, LTHE Grenoble

---

**AUTRES MEMBRES DU JURY :**

**M ROSE Jérôme**

DR CNRS, CEREGE Aix-en-Provence

# Transport de nanoparticules de $\text{TiO}_2$ en milieux poreux saturés et non saturés : expériences et modélisation

## Résumé

Le transport de nanoparticules (NP) de dioxyde de titane ( $\text{TiO}_2$ ) manufacturées a été étudié dans un milieu poreux sous différentes conditions de saturation, vitesse d'écoulement et force ionique (IS). Les courbes de percée montrent que la quantité de NP retenue diminue quand la vitesse d'écoulement augmente, et qu'elle est influencée par la teneur en eau en présence d'une IS plus grande que 3 mM KCl. On peut supposer que l'interface entre eau et air (AWI) ne retient pas de NP en présence d'IS supérieurs ou égaux à 3 mM KCl.

Les courbes de percées des expériences conduites en présence d'une IS de 5 mM, influencées par les profils de teneur en eau et de vitesse, ont été modélisées. Le modèle de transport 3P, qui tient en compte l'AWI et les effets de la vitesse, a été développé pour décrire la rétention des NP. Ce modèle dépend de trois paramètres et du profil de teneur en eau, modélisé à travers les paramètres hydrodynamiques identifiés auparavant. Le modèle 3P donne lieu à une meilleure description des données par rapport à celle du modèle classique, souvent utilisé en littérature. Il peut d'ailleurs être utilisé en milieu saturé comme insaturé.

Mots-clés : nanoparticules, dioxyde de titane, milieu poreux, rétention, transport, AWI, modélisation

## Résumé en anglais

The transport of manufactured titanium dioxide ( $\text{TiO}_2$ , rutile) nanoparticles (NP) in porous media was investigated under different saturation, water velocity and ionic strength (IS) conditions. The breakthrough curves show that the amount of retained NPs decreases when the water velocity increased and that  $\text{TiO}_2$  NP retention is influenced by the water content for values of IS larger than 3 mM KCl. It can be assumed that the interface between air and water (AWI) does not retain  $\text{TiO}_2$  NP for IS equal to, or smaller than, 3 mM KCl.

The breakthrough curves with an IS of 5mM KCl, influenced by water content profile and water velocity profile, were modeled. The 3P transport model was developed to describe the retention of  $\text{TiO}_2$  NP, taking into account the AWI and the effects of the water velocity. This model depends on three parameters and takes into account the water content profile of the porous medium, modeled through the previously identified hydrodynamic parameters. The 3P model provides a better data description than the classic Langmuirian retention model, often used in the literature. Moreover, it can be applied under both saturated and unsaturated conditions.

Key words: nanoparticles, titanium dioxide, porous medium, retention, transport, AWI, modeling

---

## Remerciements

---

*Je voudrais remercier Philippe Ackerer et François Lehmann, qui m'ont accueilli dans leurs équipe et qui ont été à mon côté pendant les durs quatre ans de ma thèse. Je remercie aussi Thierry Mara, qui a permis le financement de ma quatrième année de thèse.*

*Je remercie toutes les personnes du LHyGeS avec lesquelles j'ai collaboré : Véronique Adam, Solenn Cotel, Gaetana Quaranta, Stéphanie Lawniczak, Ti-phaine Weber.*

*Je remercie, pour l'aide dans la caractérisation des nanoparticules, Catherine Galindo et Mireille Del Nero de l'IPHC de Strasbourg et Jérôme Labille du CE-REGE de Aix-en-Provence. Je remercie également Jean-Yves Bottero et tous les partenaires du projet Mesonnet, qui a financé les premier trois ans de ma thèse.*

*Je remercie toutes les personnes qui ont égayé mes pauses dans les longues journées de travail, vous savez qui vous êtes.*

*Je remercie mes nouveaux amis de Strasbourg.*

*Ringrazio i miei genitori e mia sorella, i miei amici italiani. Nella distanza vi porto nel cuore.*

*Ringrazio Eleonora, per la nostra nuova famiglia.*

Strasbourg, 3 Décembre 2015



---

## CONTENTS

---

PREAMBLE	15
FRENCH LANGUAGE SUMMARY	19
1 INTRODUCTION	31
1.1 Nanomaterials . . . . .	31
1.1.1 Properties . . . . .	31
1.1.2 Applications . . . . .	32
1.1.3 Environmental Fate and Risks of Nanoparticles . . . . .	33
1.1.4 Colloidal Particles . . . . .	37
1.2 Surface Properties and Nanoparticles Retention . . . . .	38
1.2.1 DLVO Theory . . . . .	38
1.2.2 Particle Aggregation . . . . .	43
1.2.3 Filtration Theory . . . . .	44
1.2.4 Retention at the air-water interface . . . . .	47
1.2.5 Other retention mechanisms . . . . .	49
1.3 Flow and Mass Transfer in Porous Media . . . . .	49
1.3.1 Equation of flow . . . . .	50
1.3.2 Soil hydrodynamic properties . . . . .	51
1.3.3 Solute Transport Equation . . . . .	52
1.4 Inverse Problem Resolution . . . . .	55
1.4.1 Levenberg-Marquardt algorithm . . . . .	56
1.4.2 Gradient and Hessian calculation . . . . .	57
1.4.3 Error analysis of estimated parameters . . . . .	58
2 MATERIALS CHARACTERIZATION	61
2.1 Nanoparticles Characterization . . . . .	61
2.1.1 Zero Charge Point . . . . .	61
2.1.2 Colloidal Stability and UV-vis Spectroscopy . . . . .	62
2.1.3 DLVO Interaction Profiles . . . . .	64
2.2 Sand Characterization . . . . .	66
2.2.1 Composition and Granulometry . . . . .	66

2.2.2	Sand Cleaning Protocol . . . . .	66
2.3	Hydrodynamic Parameters . . . . .	70
2.3.1	Materials . . . . .	70
2.3.2	Calibration of the Water Content Sensors . . . . .	72
2.3.3	Experiences . . . . .	72
2.3.4	Unsaturated Hydraulic Soil Parameters Estimation . . . . .	76
2.4	Conclusion . . . . .	79
3	TRANSPORT OF NANOPARTICLES IN A SATURATED POROUS MEDIUM	81
3.1	Materials and Methods . . . . .	81
3.1.1	Column System . . . . .	81
3.1.2	Experimental Protocol for Preparation of the Saturated Porous Media . . . . .	82
3.1.3	Experimental Protocol for Preparation of TiO <sub>2</sub> Nanoparti- cle Suspension . . . . .	82
3.1.4	Experimental Protocol for Nanoparticle Transport under Saturated Conditions . . . . .	84
3.1.5	Single Collector Efficiency . . . . .	85
3.1.6	Breakthrough Curves . . . . .	86
3.1.7	Challenges Related to Saturated Experiments . . . . .	86
3.2	Modeling . . . . .	89
3.2.1	Inverse Problem Resolution . . . . .	89
3.2.2	Optimized Transport Parameters . . . . .	90
3.2.3	Attachment Efficiency Analysis . . . . .	92
3.2.4	Equation for Water Velocity Effect on Transport Parameters	93
3.3	Conclusion . . . . .	93
4	TRANSPORT OF NANOPARTICLES IN AN UNSATURATED POROUS MEDIUM	97
4.1	Materials and Methods . . . . .	97
4.1.1	Column System . . . . .	97
4.1.2	Experimental Protocol for Preparation of the Unsaturated Porous Medium . . . . .	98
4.1.3	Experimental Protocol for Nanoparticle Transport under Unsaturated Conditions . . . . .	100
4.1.4	Cumulative Water Mass . . . . .	100
4.1.5	Breakthrough Curves . . . . .	102
4.1.6	Challenges Related to Unsaturated Experiments . . . . .	103
4.2	Modeling . . . . .	104
4.2.1	Water Content Profile Modeling and K <sub>s</sub> Estimation . . . . .	104

4.2.2	Fortran Code with Transport Parameters Dependent on Water Content and Water Velocity . . . . .	107
4.2.3	Transport Modeling . . . . .	108
4.2.4	Optimized Transport Parameters . . . . .	110
4.3	Conclusion . . . . .	116
5	CONCLUSION AND PERSPECTIVES	117
5.1	Conclusion . . . . .	117
5.2	Environmental Implications . . . . .	119
5.3	Perspectives . . . . .	121
	NOTATIONS	127
	BIBLIOGRAPHY	139
	CURRICULUM VITAE	143





---

## LIST OF FIGURES

---

- 1 (a) Potentiel zeta ( $\zeta$ ) des suspensions de NP de  $\text{TiO}_2$  mesuré en fonction du pH pour différentes forces ioniques (0 mM, 3 mM, 5 mM KCl). (b) Diamètre hydrodynamique de la suspension de NP de  $\text{TiO}_2$  pour une force ionique de 0 mM. . . . . 22
- 2 (a) Profils de teneur en eau modélisés pour les expériences non saturées avec une force ionique de 5 mM. (b) Profils de vitesse d'écoulement modélisés pour les expériences non saturées avec une force ionique de 5 mM. . . . . 24
- 3 (a) Courbes de percée, et prévisions du modèle calibré, des expériences de transport de NP avec une force ionique de 5 mM et différentes vitesses d'écoulement. Les deux paramètres du modèle de rétention ( $k_a$ ,  $s_{\max}$ ) ont été optimisés pour chaque courbe. (b) Paramètres du modèle optimisés représentés en fonction de  $\eta_0$ . . . . . 26
- 4 Courbes de percée, et prévisions des modèles calibrés 3P (a) et 2P (b), des expériences de transport de NP avec une force ionique de 5 mM et différents profils de saturations. Le niveau de saturation moyen est de 70 % pour Uns4, 67 % pour Uns5 et 64 % pour Uns6. Les paramètres  $k_a$  et  $s_{\max}$  ont été optimisés pour chaque courbe pour le modèle 2P et les paramètres  $\alpha_{pc}^{AWI}$ ,  $a_2^{AWI}$  et  $a_3^{AWI}$  ont été optimisés pour chaque courbe pour le modèle 3P. . . . . 28
- 1.1 a) The percentage of atoms localized at the surface of a nanoparticle as a function of nanoparticle diameter. Non-bulk properties only emerge for diameters of less than 20-30 nm (red line)(Auffan et al. 2009b). b) SEM image of  $\text{TiO}_2$  NP (Ouyang et al. 2012). . . 34

1.2	Pathways and transformations of the nanoparticles in the environment (Batley et al. 2011). The nanoparticles released in the environment can reach the water bodies directly, e.g. via the wastewater treatment plants effluents, or indirectly, e.g. via the surface run-off. Due to their high reactivity, nanoparticles are expected to interact with each other, with other particles or with natural organic matter. They can lose their nanometrical size if subject to homoaggregation, heteroaggregation, dissolution or degradation. In case of homoaggregation or heteroaggregation, nanoparticles are removed from the water phase due to sedimentation. The fraction of nanoparticles that succeeds in seeping into the soil, can reach the aquifer or be retained by the unsaturated zone of the ground. The nanoparticle retention is controlled by several mechanisms, depending on chemical and physical parameters. . . . .	36
1.3	Two spherical particles of radii $R_1$ and $R_2$ ; the shortest surface-to-surface distance is denoted by $d$ (Hamaker 1937). . . . .	39
1.4	Simple model of double layer and its potentials where $\Phi_0$ is the surface potential, $\Phi_h$ is the potential of the Helmholtz layer and $\Phi_{edl}$ is the potential of the double layer. . . . .	41
1.5	Total interaction potential between two surfaces in DLVO theory. .	41
1.6	Attachment efficiencies of fullerene NP as a function of NaCl concentration at pH 5.2. The CCC based on these data is 120 mM NaCl (Chen and Elimelech 2006). . . . .	44
1.7	A suspended particle may leave the streamline and come in contact with a collector through three mechanisms (Yao et al. 1971). . . .	45
1.8	Schematic of the torques experienced from a transported particle that came in contact with a collector surface. The hydrodynamic torque acting on the particle, $T_{\text{hydrodynamic}}$ , is due to the drag force applied by the fluid flow, $F_H$ . The adhesive torque, $T_{\text{adhesive}}$ , is caused by the adhesive (DLVO) force acting between the collector and particle surfaces, $F_A$ (Torkzaban et al. 2007). . . . .	46
1.9	Retention mechanisms related to grains irregularities. . . . .	50
1.10	Idealized hysteretic soil water retention function (Šimunek et al. 1999). . . . .	53

2.1	a) Zeta potential ( $\zeta$ ) of the NPs suspension measured as a function of pH under different ionic strength values (0 mM, 3 mM, 5 mM KCl). b) Hydrodynamic diameter of NPs suspension at 0 mM. Both images are referred to a 50 mg/L TiO <sub>2</sub> NP suspension. Rate of increase in NP size under different NaCl (c) and KCl (d) concentrations. e) Stability ratio (W) under different KCl and NaCl concentrations. f) UV-vis absorbance spectra of TiO <sub>2</sub> NP suspensions at different concentrations and calibration curve at 280 nm. (Toloni et al. 2014).	63
2.2	a) DLVO interaction profile between NP and collector surface at 5 mM. Contributions from van der Waals and electrical double layer interactions are shown. b) DLVO interaction profiles between NP and collector surface at 5 mM, 3 mM and 1mM (Toloni et al. 2014). (c) DLVO interaction profiles between two NP surfaces at 5 mM, 3 mM and 1mM. (d) DLVO interaction profiles between NP surface and the AWI for AWI $\zeta$ potential equal to -15 mV, -50 mV and -65 mV at 5mM. (e) DLVO interaction profiles between NP surface and the AWI for AWI $\zeta$ potential equal to -50 mV and assuming an hydrophobic behavior ( $\theta = 100^\circ$ ) or an hydrophilic behavior ( $\theta = 15^\circ$ ).	65
2.3	(a) Grain size distribution of the quartz sand K30 from Kaltenhouse, France. SEM images of a grain of quartz (b) and orthoclase (c)	67
2.4	Dissolved concentrations of phosphorus (P), iron (Fe), magnesium (Mg), titanium (Ti), calcium (Ca) and aluminum (Al) measured through ICP-MS on the used solutions after each step of the sand cleaning protocol.	69
2.5	Experimental set up for the estimation of the van Genuchten soil hydrodynamic parameters. Two medium impedance probes (right side) and five tensiometers (left side and bottom) were installed in the sand packed column. The reservoir, which control the water content, in the picture is in the higher position, which corresponds to a completely saturated condition. Water content captor (b) and pressure head captor (c)	71
2.6	Linear, polynomial and square root fit of the water content values. The square root relation results to be better than the relations provided by the manufacturer.	73

2.7	Pressure head (a) and water content (b) values at -7 cm during the first drying and wetting cycle. The presence of an hysteretic behavior can be observed, since the final water content value is lower than the starting value. c) Hysteresis curve, with the data of the three cycles. Data referred to the -7 probe except where otherwise specified. The black lines describe a deep drainage, while the red lines represent a process attaining a larger $\theta_r$ value. . . . .	75
2.8	Solution of the inverse problem. . . . .	77
3.1	(a) Experimental set up for the saturated experiments. (b) Flow cell elements. (c) Sand packed flow cell ready for a NP transport experiment. At the bottom a layer of glass beads is visible. . . . .	83
3.2	a) Single collector efficiency in function of the pore water velocity. Symbols correspond to the adopted velocities. b) Single collector efficiency contributions related to diffusion (D), interception (I) and sedimentation (G). . . . .	85
3.3	Breakthrough curves for 3 mM (a) and 5 mM (b) experiments under different water velocities. The outlet NP concentration is normalised by the inlet concentration. Each BTC is the result of a single experiment and it is not the average of the replicas. . . . .	87
3.4	Breakthrough curves for 5mM under different water velocities and calibrated model previsions. The outlet NP concentration is normalised by the inlet concentration. Each BTC is the result of a single experiment and it is not the average of the replicas. The two parameters of the retention model ( $k_a$ , $s_{max}$ ) were optimized for each BTC. . . . .	91
3.5	a) Model parameters as a function of collector efficiency. Maximal solid phase concentration $s_{max}$ and attachment coefficient $k_a$ are optimized, $k_{cal}$ is calculated. $k_a$ and $s_{max}$ are linearly fitted through Equation 3.7 and 3.8. Error bars represent the 95% confidence interval. b) Model predictions for $\alpha_{pc} = 0.12$ compared to calibrated model. . . . .	94
4.1	(a) Picture of the column set up for unsaturated transport experiments. On the left the peristaltic pump and the UPC monitors can be seen. (b) Flow cell elements. A regular and a perforated end-plate can be seen in the picture. (c) Detail of the glass beads layer that replace the bottom membrane. (d) Experimental set up for the unsaturated experiments. . . . .	99

4.2	(a) Cumulative water masses of the transition between the hydrostatic profile and the steady unsaturated profile. In the miniature the data of the 5 mM KCl experiments only were represented. (b) Breakthrough curves of the unsaturated transport experiments with a Darcy velocity of 0.0012 cm/s under an ionic strength of 0-2-3-5 mM KCl. The water content profile differs from a column to another, the average saturation is between 64% and 70%. . . . .	101
4.3	Breakthrough curve of the 3 mM KCl saturated experiment with a pore water velocity of 0.002 cm/s (SAT 3 mM) and breakthrough curve of the 3 mM KCl unsaturated experiment (UNS 3 mM, average pore water velocity 0.005 cm/s). The BTC are represented as a function of the eluted pore volumes. The volume of injected NP solution is different for the two BTC: 2.5 pore volumes for the unsaturated experiment and 3 pore volumes for the saturated experiment. . . . .	102
4.4	(a) Cumulative water mass of the UNS6 unsaturated experiment with the model prediction issued from the $K_s$ estimation. (b) Modeled water content profiles for the 5 mM unsaturated experiments. (c) Modeled pressure head profiles for the 5 mM unsaturated experiments. (d) Modeled pore water velocity profiles for the 5 mM unsaturated experiments. . . . .	106
4.5	Breakthrough curves of the 5 mM unsaturated experiments modeled by the 3P model (a) and by the 2P model (b). The differences between the BTC are related to the different water content profiles. The average saturation is 70 % for Uns4, 67 % for Uns5 and 64 % for Uns6. . . . .	113
4.6	Profiles of $k_a$ (a) and $s_{\max}$ (b) obtained through the 3P model for the unsaturated experiments. . . . .	114
4.7	Comparison between the predictions of the two models: BTC and retention profiles of the experiments Uns4 (a, d), Uns5 (b, e) and Uns6 (c, f). . . . .	115



---

## LIST OF TABLES

---

1.1	Parameters used in Tufenkji and Elimelech (2004) single collector efficiency calculation and their definitions. . . . .	48
2.1	List of the parameters employed in the DLVO calculations. <sup>(a)</sup> Bergstrom (1997). <sup>(b)</sup> Israelachvili (1985). <sup>(c)</sup> Bradford and Torkzaban (2008). <sup>(d)</sup> -40 mV is referred to 5 mM and pH 10, -50 mV is referred to 1/3 mM and pH 10. . . . .	66
2.2	Dissolved concentrations (mg/L) of phosphorus (P), iron (Fe), magnesium (Mg), titanium (Ti), calcium (Ca) and aluminum (Al) measured through ICP-MS on the used solutions after each step of the sand cleaning protocol. . . . .	68
2.3	Different calibrations for sensor 2. . . . .	73
2.4	Optimized moisture sensor parameters. . . . .	74
2.5	List of the nine values of moisture content used for calibration. Each water mass was mixed with a 2700 g sand mass. . . . .	74
2.6	Optimized sand hydrodynamic parameters with errors, starting points of the inverse problem and parameters of the hysteresis curves. . . . .	78
2.7	Correlation matrix for the van Genuchten optimized parameters. .	78
3.1	Experimental and optimized parameters for the NP transport experiments at different pore water velocities under 5 mM KCl. Errors represent the 95% confidence interval. $v$ , average pore water velocity; $M$ , retained mass percentage; $\eta_0$ , calculated single collector efficiency; $s_{\max}/C_0$ , maximal solid phase concentration; $k_a$ , optimized attachment coefficient; $\text{Corr}$ , correlation between optimized parameters $s_{\max}$ and $k_a$ ; $R^2$ , Pearson's correlation coefficient for parameter optimization; $O$ , objective function value. . . . .	91



3.2	Experimental and optimized parameters for the NP transport experiments at different pore water velocities under 5 mM KCl. Errors represent the 95% confidence interval. $v$ , average water pore velocity; $k_a$ , optimized attachment coefficient; $R^2$ , Pearson's correlation coefficient for parameter optimization; $O$ , objective function value; $\alpha_{pc}$ , calculated attachment efficiency; $k_{cal}$ , attachment coefficient calculated with $\alpha_{pc} = \widetilde{\alpha}_{pc} = 0.12$ ; $R^2_{cal}$ , Pearson's correlation coefficient for new model fit; $O_{cal}$ , objective function value for new model. . . . .	92
4.1	Estimated $K_s$ values for the 5 mM unsaturated experiments and their physical parameters. Errors represent the 95% confidence interval. . . . .	107
4.2	Average ( $S_{ave}$ , $\theta_{ave}$ ) and minimum ( $S_{min}$ , $\theta_{min}$ ) values of saturation and water content modeled for the 5 mM unsaturated experiments. Percentage of NP mass retained from the porous medium (M). . .	107
4.3	Optimized parameters of the 3P and 2P models for the unsaturated transport experiments at 5 mM KCl. Errors represent the 95% confidence interval. $a_2^{AWI}$ , $a_3^{AWI}$ and $\alpha_{pc}^{AWI}$ are the empirical 3P parameters; $R^2$ , Pearson's correlation coefficient for parameter optimization; AIC, Akaike information criterion; BIC, Bayesian information criterion; $O$ , objective function value; $s_{max}/C_0$ , 2P's maximal solid phase concentration; $k_a$ , 2P's optimized attachment coefficient; Corr, correlation between optimized parameters $s_{max}$ and $k_a$ . . . . .	112
4.4	Correlation matrix for the optimization of the 3P model parameters.	112

---

## PREAMBLE

---

Manufactured nanoparticles are regularly used in many fields. Due to their small size and high reactivity, the applications of nanoparticles in industrial processes, consumer products and medical devices increase steadily. They can be found, *inter alia*, in clothes, cosmetics, food storage and paintings. The market value of these products was estimated to reach \$3 trillion in 2014. TiO<sub>2</sub> nanoparticles represent the second most important production of nanoparticles worldwide (Adam et al. 2015).

Nevertheless, scientists pointed out the remaining knowledge gaps concerning the fate of nanoparticles in the various environmental compartments, their effects on living organisms, and consequently their potential impacts and risks on the environment and human health. Risks are related especially to the antibacterial properties of many types of nanoparticles and to their ability to cross the various biological barriers that protect organisms, including the human body.

In this context, the important role of the transport of nanoparticles in the groundwater can be easily understood. It influences the mobility of nanoparticles among the ecosystems, it could result into a contamination of the drinking water and to a long distance transport of the nanoparticles.

The purpose of the present study was to evaluate the mobility of TiO<sub>2</sub> nanoparticles in the soil, studying the behavior of TiO<sub>2</sub> nanoparticles in saturated and unsaturated porous media. Transport experiments were conducted in laboratory columns and a model was developed to describe the results. This work, realized at the Laboratory of Hydrology and Geochemistry of Strasbourg (LHyGeS), was part of the interdisciplinary MESONNET research program, funded by the French National Research Agency (ANR) and dedicated to the environmental risk assessment of engineered nanomaterials.

The structure of this thesis is divided into five chapters. The **first chapter** introduces the subject of this work and the theoretical notions on which it is based. The history of the nanoparticles use is presented, together with the principal ap-

plications of the most common nanoparticles. The potential risks related to the presence of nanomaterials in the environment are introduced. Besides, a review of the current state-of-the-art on the transport of  $\text{TiO}_2$  nanoparticles in porous media contextualizes the topic of this work.

The theoretical background used to describe the nanoparticles behavior in a porous medium, mainly the DLVO theory and the filtration theory, are presented. The chapter ends with the equations used to model the water flow and the solute transport in the porous medium, followed by numerical methods for equation solving and parameter estimation.

The **second chapter** concerns the characterization of the selected materials and the development of the experimental protocols. The preliminary work, which precedes the realization of the transport experiments, includes the characterization of the  $\text{TiO}_2$  nanoparticles solution and of the quartz sand constituting the experimental porous medium.

In order to develop the experimental protocol, the influence of chemical parameters on the behavior of the nanoparticles is studied. The sand composition is analyzed and a cleaning protocol is chosen. In order to characterize the hydrodynamic parameters of the sand, experiments of drainage and imbibition are realized. The results are used to identify the hydrodynamic parameters.

In the **third chapter** the study on the transport of  $\text{TiO}_2$  nanoparticles in a saturated porous medium is presented. The chapter is divided into three sections. The Materials and Methods section describes the experimental set up and the protocols adopted for the experiments under saturated conditions. The measured breakthrough curves are presented and commented and the challenges related to the implementation of the design of the saturated experiments are discussed.

The second section explains the approach adopted to model the results of the previous section. The water flow and the nanoparticle retention are modeled through the convection-dispersion equation with a retention site. The two parameters of the retention model are optimized and an empirical relation for their calculation as a water velocity function is proposed. The Conclusion section closes the chapter.

The **fourth chapter** presents the study of the unsaturated transport of  $\text{TiO}_2$  nanoparticles in an organization similar to the previous chapter.

In the Materials and Methods section the set up differences with the saturated ex-

periments are underlined. The measured breakthrough curves and the cumulative water masses obtained during the column drainage experiments are presented and commented. The role of the interface between air and water in the nanoparticle retention for large ionic strengths is underlined. Afterward, the challenges related to the implementation of the design of the unsaturated experiments are discussed.

The second section explains the approach adopted to model the results of the previous section. A slightly different saturated hydraulic conductivity is identified from the cumulative masses of each experiment and used, along with the previously identified hydrodynamic parameters, to model the unsaturated water flow. The nanoparticle retention is modeled through two retention models, both based on a single attachment site. The 2P model corresponds to the model applied in the third chapter, while the 3P model introduces a dependence on water velocity and water content. The parameters of the two models are optimized and the superiority of the 3P model emerges. The Conclusion section closes the chapter.

The **fifth chapter** is the conclusive chapter. The major issues of the present study are summarized and the possible environmental implications are considered. Directions for future research are proposed.



---

## FRENCH LANGUAGE SUMMARY

---

### INTRODUCTION

Ce travail de thèse a été réalisé au Laboratoire d'Hydrologie et Géochimie de Strasbourg (LHYGES) et financé par le projet ANR Mesonnet.

Les nanoparticules (NP) sont des produits manufacturés dont au moins une des dimensions est inférieure à 100 nm. Elles peuvent avoir des géométries sphériques, tubulaires, ou irrégulières et exister sous une forme individuelle, agrégée ou agglomérée. Grâce aux propriétés uniques que la taille nanométrique leur confère, les NP connaissent une énorme diffusion comme additif et dans la création de nouveaux matériaux. Elles sont utilisées dans de nombreux objets d'usage quotidien, dans des produits de beauté, dans des tissus et trouvent une large application dans les processus industriels en tant que catalyseurs. L'utilisation massive des NP au niveau industriel provoque l'émission, directe ou indirecte, des nanomatériaux dans l'environnement.

Le marché mondial des NP a été évalué à 3000 milliard des dollars pour le 2014. Les NP de dioxyde de titane ( $\text{TiO}_2$ ), avec leurs grand indice de réflexion, leurs grande absorption dans le spectre ultraviolet et des propriétés photocatalytiques, sont parmi les plus produites au monde (3000 t/an, données 2012). Elles sont utilisées surtout dans la fabrication de cosmétiques (70-80 % du total) de crèmes solaires et de colorants, mais elles peuvent être retrouvées également dans un grand nombre d'autres objets, comme par exemple les cellules photovoltaïques. Elles existent sous différentes phases cristallines : rutile, brookite et anatase. Comme la plupart des NP, selon l'utilisation à laquelle elles sont destinées, les NP de  $\text{TiO}_2$  peuvent être produites nues ou enrobées. L'enrobage des NP peut permettre d'en modifier les propriétés de surface et, par conséquence, les propriétés des matériaux qui les contiennent.

Il a été estimé que le 2% environ de la production totale de NP finit dans l'environnement. Les concentrations de NP mesurées dans l'environnement sont ty-

piquement de l'ordre du  $\mu\text{g}/\text{kg}$  ou du  $\mu\text{g}/\text{L}$ . Les estimations de la concentration de NP dans l'environnement ont encore beaucoup d'incertitude : aucun protocole analytique standardisé a été créé jusqu'à aujourd'hui. La connaissance de l'impact des nanomatériaux sur l'environnement étant encore limitée, il est d'importance capitale de comprendre le comportement des NP et leur mobilité à travers les divers écosystèmes. La connaissance du cycle de vie des NP dans les différents milieux naturels joue donc un rôle fondamental dans l'évaluation de l'impact qu'ils peuvent avoir sur la santé et sur l'écosystème. Notamment, le comportement des NP dans le sous-sol est critique pour pouvoir prévenir l'éventualité d'une contamination de la ressource en eau, impliquant la possible propagation des NP dans les eaux souterraines.

Dans un milieu poreux, tel que le sol, les NP peuvent être transportées par l'écoulement de l'eau ou interagir avec les interfaces qui séparent la surface du sable de l'eau (SWI) ou l'eau de l'air (AWI). La littérature existante se concentre surtout sur l'étude du comportement des NP en milieu poreux saturé, dans lequel il n'y a pas l'AWI. L'influence sur les NP des paramètres chimiques tels que le pH et la force ionique, et l'effet de la présence de matière organique ou de colloïdes d'origine naturelle ont été l'objet de nombreux travaux. La charge de surface des NP s'est avérée être un paramètre clef, car les interactions électrostatiques jouent un rôle majeur dans les interactions avec les autres surfaces. Elles influencent fortement, avec la force attractive de van der Waals et la force répulsive de la double couche électrique, la stabilité des NP et leur interaction avec le milieu poreux. Par contre, peu d'études ont été menées sur le transport de NP en milieu non saturé. Le rôle de l'interface entre eau et air (AWI) reste peu clair : certaines études affirment que l'AWI peut retenir les NP, autres affirment qu'elle n'en retient pas.

En ce qui concernent les modèles, la rétention des NP en milieu poreux saturé a été souvent modélisé avec une relation de type Langmuir. Les modèles nécessitent par contre toujours d'être calibrés pour chaque courbe, aucun modèle prédictif n'a encore été développé. Aucun modèle n'existe non plus pour décrire la rétention de NP en milieu poreux non saturé et tenir en compte le rôle de l'AWI. Des modèles de ce type ont été créés pour la rétention des virus ou des colloïdes, mais n'ont jamais été adaptés aux NP.

Ce travail de thèse se concentre ainsi sur le comportement des NP de  $\text{TiO}_2$  dans des milieux poreux saturés et non saturés en eau, avec un intérêt particulier pour les milieux non saturés et le rôle de l'AWI sur la rétention des NP. A cause de la grande complexité des interactions des NP avec la matière organique et les colloïdes naturels, un milieu poreux simple a été adopté. L'élimination de

la matière organique et de colloïdes du milieu poreux a permis d'étudier exclusivement l'interaction des NP avec le SWI et l'AWI. Après une première caractérisation des NP, des expériences de transport ont été conduites avec différentes vitesses d'écoulement, différentes forces ioniques et différents niveaux de saturation. Le milieu poreux a été caractérisé afin de pouvoir simuler l'écoulement et le profil de saturation. Des modèles ont été développés pour simuler correctement la rétention des NP dans le milieu poreux sous les diverses conditions, en tenant en compte la présence de l'AWI. Pour la première fois un modèle pouvant être appliqué à des milieux poreux saturés ou non saturés a été créé, tenant en compte le rôle de l'AWI, de l'SWI et de la vitesse d'écoulement dans la rétention des NP.

## MÉTHODES EXPÉRIMENTALES : CARACTÉRISATIONS

Une solution industrielle de NP de  $\text{TiO}_2$  sous forme de rutile a été adoptée. L'identification des propriétés de surface de NP étant cruciale pour prévoir leur comportement face au milieu poreux, une caractérisation des NP a été effectuée initialement. La charge de surface, le diamètre hydrodynamique et la stabilité en solution des NP ont été étudiés en fonction des conditions chimiques (pH, force ionique) ( Figure 1). Un point de charge nulle autour de pH 6 a été identifié. Pour réduire les problèmes expérimentaux et se mettre dans des conditions défavorables à la rétention des NP, un pH de 10 a été adopté pour les expériences de transport. La taille primaire des NP est de 5-30 nm, mais dans la solution utilisée pour les expériences le diamètre hydrodynamique moyen mesuré est de 100 nm : la solution est constituée pour la plupart par des agglomérats, non par des NP primaires.

Un milieu poreux contrôlé, constitué de sable de quartz, a été adopté pour les expériences de laboratoire. Le sable a été convenablement purifié de sa fraction colloïdale et des traces d'oxydes métalliques à travers des cycles de lavage basés sur des solutions acides et basiques, de manière à limiter la rétention de NP dans le milieu poreux. Le sable a été caractérisé expérimentalement : paramètres telles que la porosité, la dispersivité et les paramètres de Mualem-van Genuchten ont été identifiés. Si les premiers ont été trouvés grâce à des expériences de transport d'un traceur non réactif, les paramètres de Mualem-van Genuchten ont nécessité de multiples expériences de drainage et d'imbibition. Les paramètres hydrodynamiques du milieu poreux ainsi identifiés ont permis de modéliser correctement l'écoulement de l'eau et le transport des NP à travers ce milieu.



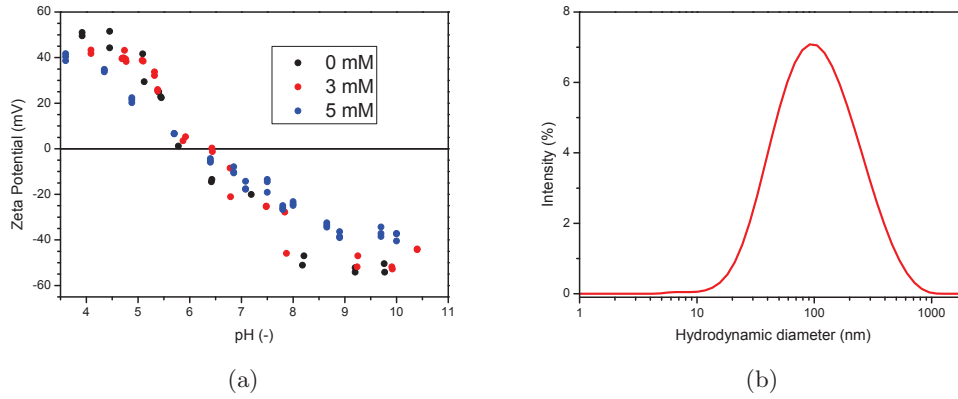


FIGURE 1 – (a) Potentiel zeta ( $\zeta$ ) des suspensions de NP de  $\text{TiO}_2$  mesuré en fonction du pH pour différentes forces ioniques (0 mM, 3 mM, 5 mM KCl). (b) Diamètre hydrodynamique de la suspension de NP de  $\text{TiO}_2$  pour une force ionique de 0 mM.

## MÉTHODES EXPÉRIMENTALES : EXPÉRIENCES DE TRANSPORT

La mobilité des NP dans un milieu poreux a été étudiée à travers des expériences de transport en colonne, conduites en milieu saturé et non saturé en eau. Des colonnes en plexiglas ont été adoptées (3.75 cm x 15.4 cm pour le milieu saturé et 3.75 cm x 30.4 cm pour le milieu non saturé), à l'intérieur desquelles le sable a été ajouté soigneusement, afin d'obtenir un milieu poreux le plus homogène et reproductible possible. Une couche de 2 cm de billes de verre à la base des colonnes est utilisée pour garder le milieu poreux en place. Le choix des billes de verre a été dicté par le fait que tous les filtres papier et les membranes en nylon testés ont modifié le transport des NP de  $\text{TiO}_2$  dans les colonnes. L'écoulement a été assuré par une pompe péristaltique. Avant chaque injection de NP le milieu poreux a été équilibré avec une solution ayant le pH et la force ionique choisis pour l'expérience. Pendant les expériences en milieu saturé, le pH, la force ionique et l'absorption UV à la longueur d'onde de 280 nm ont été mesurés 'on line' à l'entrée et à la sortie de la colonne toutes les cinq secondes.

La variation de la vitesse d'écoulement et de la force ionique de la solution entre différentes expériences de transport ont permis d'évaluer les effets de ces paramètres sur l'interaction entre sable et NP, en condition d'écoulement saturé. Aucune rétention majeure de NP n'a été observée pour des forces ioniques inférieures à 5mM KCl. En présence d'une force ionique de 3 mM, une très faible rétention a été observée. Plusieurs expériences ont été réalisées avec des vitesses de 0.07,

0.01 et 0.002 cm/s. La vitesse d'écoulement, en présence d'une force ionique suffisamment élevée (5 mM), contrôle le comportement de NP : plus la vitesse est grande, moins les NP sont retenues.

En ce qui concerne le transport de NP en condition d'écoulement non saturé, l'attention a été portée sur le rôle de la teneur en eau et de l'interface entre eau et air. Le dispositif expérimental est légèrement différent par rapport à celui utilisé avec le milieu saturé. Afin d'exposer la surface du sable à la pression atmosphérique, la tête de la colonne est percée et l'écoulement se fait du haut vers le bas, contrairement aux expériences en milieu saturé. Avant chaque expérience, après l'équilibration du milieu poreux, les colonnes ont été drainées, en imposant une pression de -15 cm à leur base, au fin d'obtenir le profil de pression souhaité.

Des expériences de transport de NP ont été conduites dans des colonnes avec différents profils de teneur en eau (saturation moyenne entre 64% et 70%). D'une manière analogue à ce qui a été trouvé pour le milieu saturé, en présence d'une force ionique de 3 mM une faible rétention de NP a été observée, tandis que pour une force ionique de 5 mM une rétention importante a été observée. En raison du contrôle partiel obtenu sur le processus instable du drainage gravitationnel, il n'a pas été possible de reproduire les expériences. Les courbes de percée obtenues diffèrent l'une de l'autre pour les expériences avec une force ionique de 5 mM, ainsi que les masses cumulées enregistrées par la balance électronique pendant les drainages des colonnes. Par contre, les courbes de percée obtenue sous une force ionique de 3mM sont reproductibles et équivalentes à celles obtenues en milieu non saturé sous la même force ionique. Ces résultats montrent donc que la rétention de NP est influencée par la présence de l'interface entre eau et air à 5 mM mais pas à 3mM. La rétention de NP à 3 mM peut ainsi être attribuée totalement à l'interface entre sable et eau.

## MODÉLISATION

L'écoulement a été modélisé à l'aide de l'équation générale de l'écoulement :

$$\frac{\partial \theta}{\partial t} = \frac{\partial}{\partial z} \left[ K(h) \left( \frac{\partial h}{\partial z} - 1 \right) \right] \quad (1)$$

et du modèle de Mualem-van Genuchten :

$$\theta(h) = \begin{cases} \theta_r + \frac{\theta_s - \theta_r}{[1 + |\alpha h|^n]^m} & h < 0 \\ \theta_s & h \geq 0 \end{cases} \quad (2)$$

$$K(h) = K_s S_e^l \left[ 1 - \left( 1 - S_e^{1/m} \right)^m \right]^2 \quad (3)$$

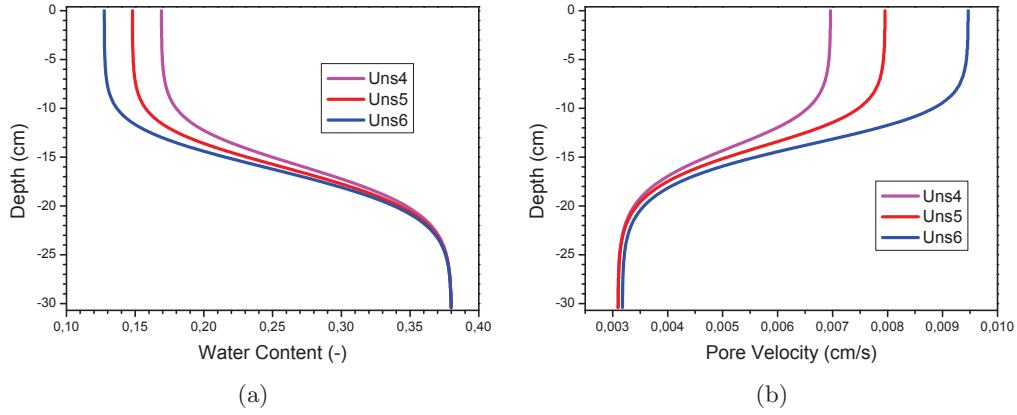


FIGURE 2 – (a) Profils de teneur en eau modélisés pour les expériences non saturées avec une force ionique de 5 mM. (b) Profils de vitesse d'écoulement modélisés pour les expériences non saturées avec une force ionique de 5 mM.

où  $\theta$  [ $\text{m}^3/\text{m}^3$ ] est la teneur en eau,  $t$  [s] est le temps,  $z$  [m] est la profondeur,  $K(h)$  [m/s] est la conductivité hydraulique,  $h$  [m] est la pression capillaire,  $\theta_s$  [ $\text{m}^3/\text{m}^3$ ] est la teneur en eau à saturation,  $\theta_r$  [ $\text{m}^3/\text{m}^3$ ] est la teneur en eau résiduelle,  $m = 1 - 1/n$ ,  $n > 1$ ,  $n$  [-] est l'indice de distribution de la taille des pores,  $\alpha$  [ $\text{m}^{-1}$ ] est lié à l'inverse du rayon caractéristique des pores et  $l$  [-] est le paramètre de connectivité porale. Les profils de saturation et teneur en eau modélisés (Figure 2), montrent que il y a une variation sensible de la vitesse d'écoulement le long des profils, ainsi qu'une différence assez forte du niveau de saturation entre l'entrée et la sortie des colonnes. Également, les profils changent entre une colonne et l'autre. Considéré que dans des conditions non saturés la teneur en eau influence directement la rétention des NP, cela montre l'importance de modéliser correctement l'écoulement.

Les courbes de percée obtenues en milieu saturé ont été modélisées à l'aide de l'équation de Convection-Dispersion couplée à un terme de rétention qui dépend de deux paramètres :

$$\begin{cases} \frac{\partial \theta C}{\partial t} + \rho \frac{\partial s}{\partial t} = \frac{\partial}{\partial z} \left( \theta D \frac{\partial C}{\partial z} \right) - \frac{\partial q_D C}{\partial z} \\ \rho \frac{\partial s}{\partial t} = \theta k_a \psi C \\ \psi = 1 - \frac{s}{s_{max}} \end{cases} \quad (4)$$

où  $\rho$  [ $\text{kg}/\text{m}^3$ ] est la densité apparente du milieu poreux,  $C$  [ $\text{kg}/\text{L}$ ] est la concentration de NP dans la phase liquide,  $s$  [ $\text{kg}/\text{kg}$ ] est la concentration de NP dans la phase solide,  $D$  [ $\text{m}^2/\text{s}$ ] est le coefficient de dispersion,  $q_D$  [m/s] est la vitesse de Darcy,  $k_a$  [ $\text{s}^{-1}$ ] est le coefficient d'attachement et  $s_{max}$  [ $\text{kg}/\text{kg}$ ] est la valeur

maximale que  $s$  peut assumer.

Les paramètres ont été déterminés grâce à la résolution du problème inverse effectuée avec le logiciel HYDRUS 1D, utilisé aussi pour modéliser l'écoulement. La modélisation ainsi obtenue décrit de manière satisfaisante le comportement de NP pour les deux vitesses les plus élevées (Figure 3). La courbe de percée obtenue pour la vitesse la moins élevée a été décrite en manière moins satisfaisante, due à l'incapacité du modèle adopté à décrire correctement une courbe non-monotone.

Les paramètres optimisés ont été interprétés à l'aide de la théorie classique de la filtration. Cette analyse a permis de montrer que les paramètres dépendent de manière linéaire de l'efficacité de contact ( $\eta_0$ ), un paramètre calculé en fonction de la vitesse d'écoulement et de caractéristiques physiques du système ( Figure 3b). Il est possible aussi d'affirmer que les paramètres dépendent en manière non linéaire de la vitesse. Des équations ont été développées pour calculer les paramètres pour toutes vitesses dans une gamme entre 0.07 et 0.002 cm/s, et probablement dans une gamme plus large aussi, permettant ainsi de simuler la rétention de NP sous ces conditions.

A partir des paramètres optimisés, la théorie de la filtration a permis aussi de calculer l'efficacité d'attachement ( $\alpha_{pc}$ ), un paramètre représentant la probabilité de chaque NP de rentrer en contact avec un grain de sable et d'y rester collée. L'efficacité d'attachement a résulté être indépendante de la vitesse d'écoulement, dans la gamme des vitesses considérées.

Les résultats obtenus en milieu non saturé ont été modélisés de deux manières différentes. Les deux modèles développés, appelés 2P et 3P, ont respectivement deux et trois paramètres. Le modèle 2P correspond à l'approche utilisée pour le milieu saturé : les deux paramètres de rétention sont optimisés à l'aide de HYDRUS 1D. Le modèle 3P, par contre, tient en compte les profils de vitesse et de teneur en eau du milieu poreux. Le modèle 2P décrit seulement implicitement l'effet de la présence de l'interface entre eau et air, alors que le modèle 3P en tient compte explicitement :

$$\begin{cases} k_a^{uns} = \frac{3(1-\theta)q_D}{2d_c\theta}\alpha_{pc}\eta_0 + \left(\frac{3q_D}{2d_c\theta}\alpha_{pc}^{AWI}\eta_0 + a_2^{AWI}\right)\left(1 - \frac{\theta}{\theta_s}\right) \\ s_{max}^{uns} = a_3\eta_0\left(\frac{\theta}{\theta_s}\right)^{2/3} + a_3^{AWI}\eta_0\left(1 - \frac{\theta}{\theta_s}\right)^3 \end{cases} \quad (5)$$

où  $d_c$  [m] est la taille moyenne des grains de sable,  $\alpha_{pc}^{AWI}$  [-],  $a_2^{AWI}$  [s<sup>-1</sup>] et  $a_3^{AWI}$  [cm<sup>3</sup>/g] sont des paramètres empiriques. Les paramètres  $a_3$  [cm<sup>3</sup>/g] et  $\alpha_{pc}$  [-] ont été identifié précédemment pour décrire la rétention de NP dans un milieu poreux

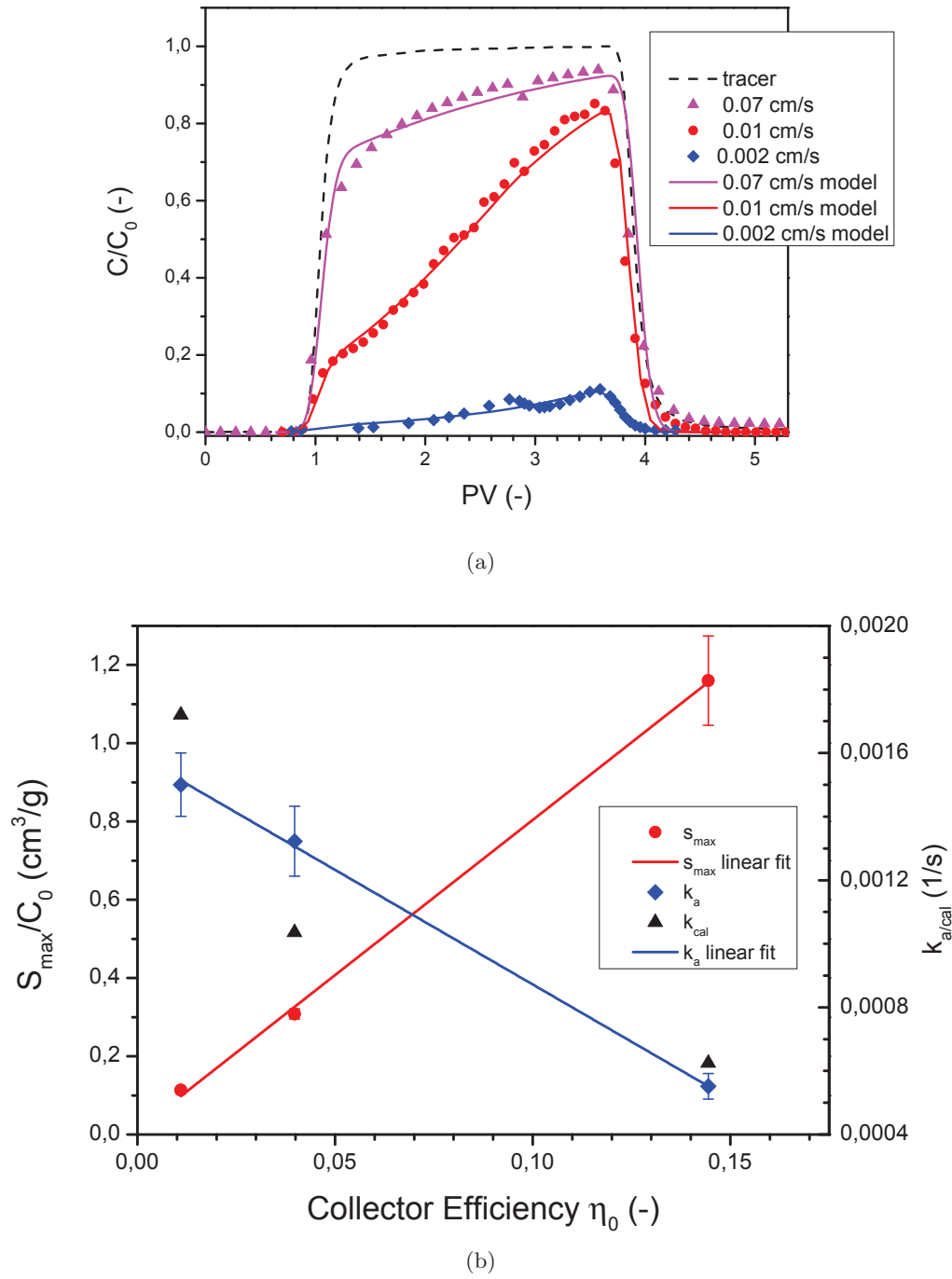


FIGURE 3 – (a) Courbes de percée, et prévisions du modèle calibré, des expériences de transport de NP avec une force ionique de 5 mM et différentes vitesses d'écoulement. Les deux paramètres du modèle de rétention ( $k_a$ ,  $S_{max}$ ) ont été optimisés pour chaque courbe. (b) Paramètres du modèle optimisés représentés en fonction de  $\eta_0$ .

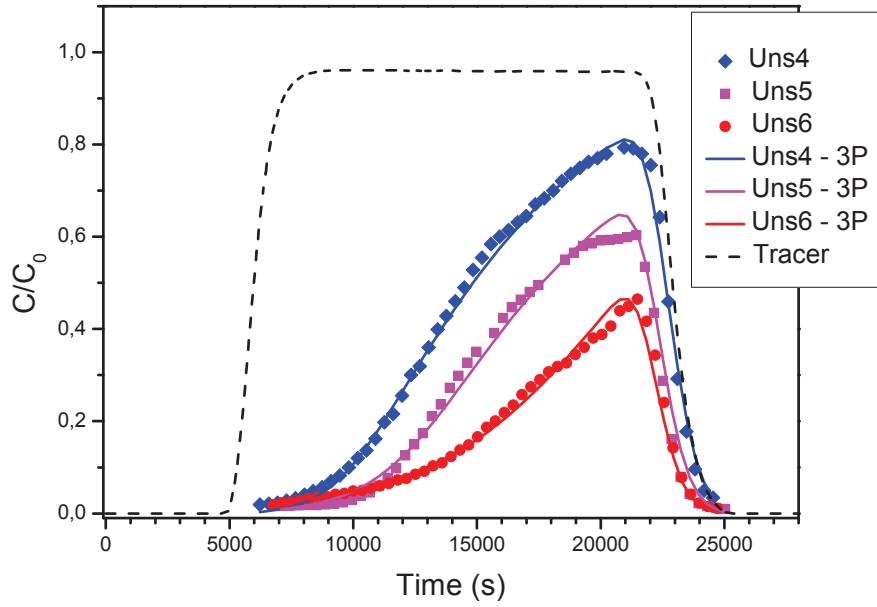
saturé.

Le modèle 3P a été développé à partir des équations qui décrivent les paramètres de rétention en fonction de la vitesse pour un milieu poreux saturé. Les équations ont été modifiées de manière à tenir compte de la présence de l'interface entre eau et air. Les hypothèses à la base de ce modèle sont (1) la rétention à la surface des grains de sable peut être décrite par les mêmes équations dans un milieu saturé et non saturé et (2) la rétention à l'interface entre eau et air est proportionnelle à la fraction du milieu poreux occupée par l'air. Le modèle dépend de trois paramètres, qui ont été optimisés par un code fortran. Il donne lieu à une simulation des données meilleure que celle obtenue par le modèle 2P, d'après les critères AIC et BIC, pour deux des trois courbes modélisées (Figure 4). Le modèle 3P peut être utilisé pour un milieu non saturé comme pour un milieu saturé car, quand la teneur en eau tend à la saturation, ses équations tendent vers les équations pour le milieu saturé.

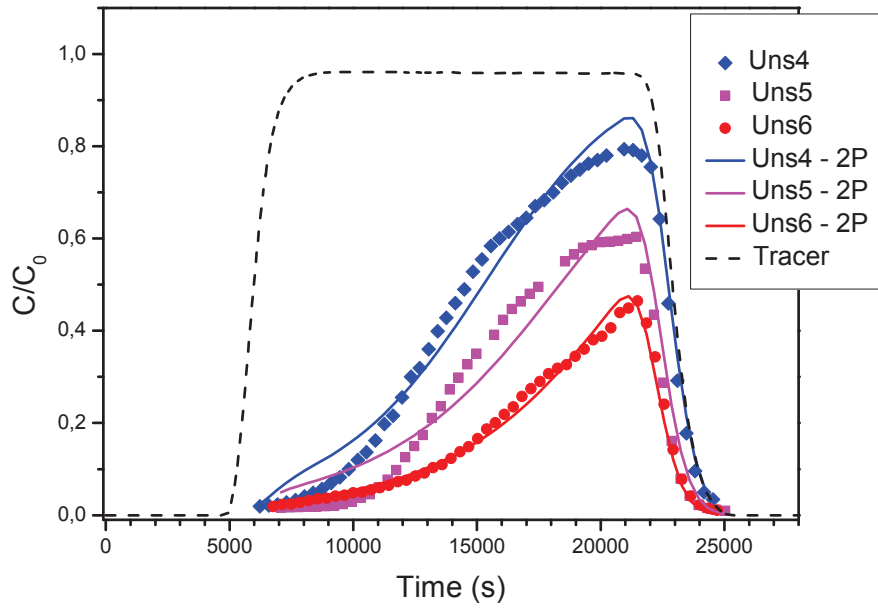
## CONCLUSIONS ET IMPLICATIONS ENVIRONNEMENTALES

Dans ce travail de thèse un protocole expérimentale pour réaliser des expériences de transport avec de NP de  $\text{TiO}_2$ , dans des milieu poreux saturé et non saturés en eau, a été développé. Un modèle empirique a été également développé pour décrire la rétention des NP observé en condition saturée ou non saturée. Ce modèle tiens en compte le profil de teneur en eau et de vitesse du milieu poreux, ainsi que la présence de l'interface entre l'eau et l'air en milieu non saturé. C'est la première fois qu'un modèle qui considère l'AWI est appliqué à la rétention des NP.

Les expériences de transport effectuées en conditions non saturées ont mis en lumière que, dans le milieu poreux étudié, la rétention de NP a lieu à l'interface entre eau et air exclusivement en présence d'une force ionique supérieure à 3 mM KCl. Compte tenu de ce résultats, des NP de  $\text{TiO}_2$  émises à la surface du sol, dans les conditions chimiques appliquées dans cet étude, auront très peu de chances de traverser la zone non saturée et contaminer les eaux souterraines. Dans la zone non saturée, l'eau s'infiltre en descendant de la surface du sol vers la zone saturée, ou remonte de la zone saturée par effet de capillarité. Étant donné que, d'après notre étude, les NP sont fortement retenues par l'interface entre eau et air, elles sont fortement retenues par la zone non saturée. Il faut aussi rappeler que dans cette étude, des conditions chimiques défavorables à la rétention des NP ont été adoptée ce qui réduit d'autant la potentielle contamination de ces NP des eaux souterraines dans des conditions de milieu naturel.



(a)



(b)

FIGURE 4 – Courbes de percée, et prévisions des modèles calibrés 3P (a) et 2P (b), des expériences de transport de NP avec une force ionique de 5 mM et différents profils de saturations. Le niveau de saturation moyen est de 70 % pour Uns4, 67 % pour Uns5 et 64 % pour Uns6. Les paramètres  $k_a$  et  $s_{\max}$  ont été optimisés pour chaque courbe pour le modèle 2P et les paramètres  $\alpha_{pc}^{AWI}$ ,  $a_2^{AWI}$  et  $a_3^{AWI}$  ont été optimisés pour chaque courbe pour le modèle 3P.

Dans le scénario le plus probable, les NP de  $\text{TiO}_2$  émises à la surface du sol seront retenues dans les premiers centimètres de sol. Les NP retenues, si bio-disponibles, peuvent représenter un risque pour la santé des plantes, de la rhizosphère et pour l'écosystème du sol en général. Il est plutôt sur l'impact des NP sur ces organismes qu'il faudrait investiguer.





# CHAPTER 1

## INTRODUCTION

### CONTENTS

1.1	Nanomaterials . . . . .	31
1.2	Surface Properties and Nanoparticles Retention . . . . .	38
1.3	Flow and Mass Transfer in Porous Media . . . . .	49
1.4	Inverse Problem Resolution . . . . .	55

## 1.1 NANOMATERIALS

### 1.1.1 PROPERTIES

NANOPARTICLES (NP) are manufactured products having at least one dimension measuring 100 nm or less. This is a particularly interesting size range, which bridges the gap between small molecules (with discrete energy states) and bulk materials (with continuous energy states). They can be spherical, tubular or irregularly shaped and can exist in single, aggregated or agglomerated forms. Naked NP can be employed, but often they present various coatings and surface functionality (Nowack and Bucheli 2007). According to the International Organization for Standardization (ISO), manufactured nanomaterials comprise seven main classes: carbonaceous nanomaterials (e.g., carbon nanotubes (CNTs)); semiconductors (e.g., quantum dots); metal oxides (e.g., titanium oxide); nanopolymers (e.g., dendrimers); nanoclays; emulsions (e.g., acrylic latex); and metals (e.g., silver) (Batley et al. 2011).

The potential of this technology is hidden in the huge specific surface of NP. In bulk materials, only a relatively small percentage of atoms will be at the surface. In NP, the small size ensures a large percentage of surface atoms, sometimes 50% or more in some cases (size < 5 nm) (see Figure 1.1). This confers to NP characteristics that are not shared by non-nanoscale particles with the same

chemical composition. There is a critical size, typically around 20-30 nm, beneath which NP behavior changes. These smaller NP have a size dependent crystallinity that gives them properties drastically different from the bulk material (Auffan et al. 2009b).

Most of the size effects are predictable in part from thermodynamics, as a direct consequence of the Laplace equation. Since NP below 20-30 nm in size are characterized by an excess of energy at the surface and are thermodynamically unstable, this affects the interfacial reactivity. Optical and electronic properties, thermal properties and photocatalytic activity result to be size dependent. Moreover, the extremely small size at the nano scale is of the same scale as the critical size for physical phenomena: for example, the radius of the tip of a crack in a material may be in the range 1-100 nm. The way a crack grows in a larger scale material is likely to be different from crack propagation in a nanomaterial where crack and particle size are comparable (Liu 2010).

### 1.1.2 APPLICATIONS

Metal NP have been unknowingly used for many centuries, primarily for their optical properties. For example, gold, copper and silver NP confer colors to many stained glass windows dating from the middle ages. The Romans used NP to color glass and colloidal gold NP were used in cosmetics by the ancient Egyptians. Silver and copper NP have also been used since the Middle Ages to give luster to ceramics. Moreover, the use of silver NP as bactericide in ancient medicine predates the discovery of antibiotics and, more recently, silver NP were important in the photographic process (Johnston 2012).

Nowadays, NP are present, inter alia, in sunscreens, coatings, paintings, sports clothing, alimentary packaging, solar cells and fuel cells, just to give a few examples of well-known consumer products. Some of the most employed NP are titanium dioxide NP ( $\text{TiO}_2$  NP) (Figure 1.1), carbon nanotubes (CNT), silver NP (Ag NP) and iron NP (Fe NP).

$\text{TiO}_2$  NP. Titanium dioxide NP have a very high refractive index ( $n = 2.7$ ), surpassed only by a few other materials, and are strong UV absorbers and photocatalysts, i.e. catalysts in photoreactions.  $\text{TiO}_2$  NP brightness, related to the refractive index, is very useful in inks, paints and coatings. Due to their UV resistant properties,  $\text{TiO}_2$  NP are present in plastics and other applications where they act as UV absorbers, efficiently transforming destructive UV light energy into heat. The above-mentioned properties make  $\text{TiO}_2$  NP excellent for sunscreens. As catalysts of photolysis,  $\text{TiO}_2$  NP are incorporated into building materials such as cement and surface coatings in order to reduce nitrogen oxides ( $\text{NO}_x$ ) levels in ambient air. This property is

also applied in water disinfection, in crude oil decomposition, in antifouling marine paints and to sterilize surgical instruments. The list of  $\text{TiO}_2$  NP applications is even longer: self-cleaning glasses, solar cells, high-density data storage and many more (Godinez and Darnault 2011)

**CNT.** Carbon nanotubes are carbon nanomaterials that belong to the fullerene family, i.e., cylindrical fullerenes with a high length-to-diameter ratio. The novel properties of CNT prompt their applications in many emerging technologies, particularly in creating new materials with extraordinary strength and unique electrical and thermal properties. They are employed in the production of maritime vessels, bicycle components and a variety of sport implements. CNT have also bio-medical and nanoelectronics applications (Tian et al. 2010).

**Ag NP.** The antibacterial properties of Ag NP are well-known and they are now commonly used in wound dressings and in other disinfectant and antiseptic applications due to the increase in antibiotic-resistant bacteria. Ag NP inhibit the growth of bacteria and fungi on clothing, such as socks, and are therefore added to reduce odors and the risk of bacterial and fungal infection. Their antibacterial properties are also exploited in cosmetics, food storage, toys, and even food supplements (Navarro et al. 2008).

**Fe NP.** The great reactivity and reductive power of iron NP (zerovalent iron or iron oxides) is useful in the field of groundwater and soil remediation. Being an electron acceptor for contaminant oxidation, iron NP can remove from subsurface environments or immobilize a variety of organic contaminant, contaminant metals and metalloids by reducing them to less soluble forms (Tosco et al. 2012).

Moreover, the combination of the size of NP and the possibility of modifying their surfaces by coordinating surfactants to increase their lipophilicity or hydrophilicity, or to target specific cells, make them particularly attractive in biomedical applications, including: biodiagnostics (e.g. taking advantage of the sensitivity of plasmon resonances and other physical properties to the coordination of biomolecules), imaging (e.g. in fluorescence microscopy and Magnetic Resonance Imaging), drug delivery (typically employing relatively inert hollow gold NP and nanorods) and other therapeutic applications (e.g. using the NP as an agent for localized heating, radiation, etc.)(Johnston 2012).

### 1.1.3 ENVIRONMENTAL FATE AND RISKS OF NANOPARTICLES

Inevitably, as a consequence of the widespread use of NP in technological applications and even in consumer goods, direct and indirect emissions in the environ-

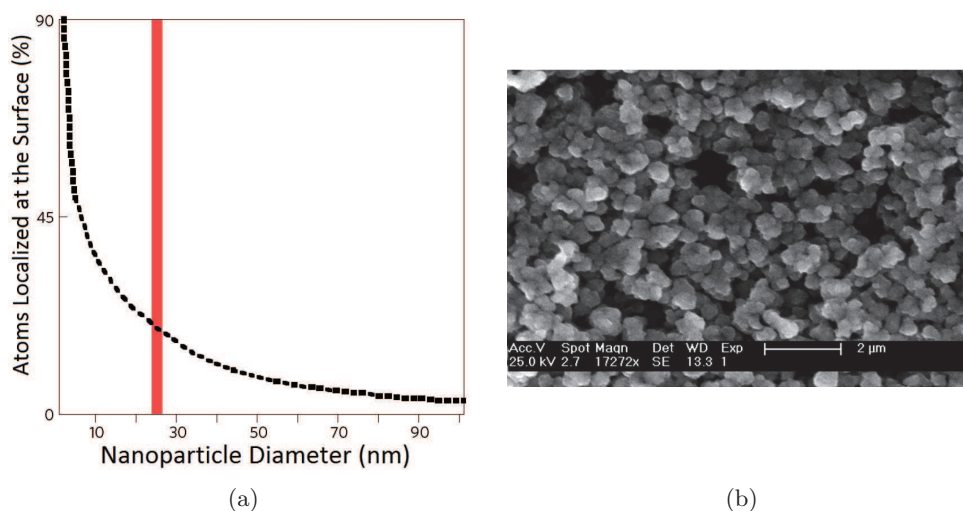


Figure 1.1: a) The percentage of atoms localized at the surface of a nanoparticle as a function of nanoparticle diameter. Non-bulk properties only emerge for diameters of less than 20-30 nm (red line)(Auffan et al. 2009b). b) SEM image of TiO<sub>2</sub> NP (Ouyang et al. 2012).

ment occur, leading to a NP presence in air, water and soil. Besides intentional NP environmental emissions for remediation and agricultural purposes, NP can be present in municipal solid waste, construction waste, industrial waste and wastewater. These NP can remain in the environment for long periods and can be potentially dangerous, both medically and environmentally. Upon release, NP are likely to interact with aquatic surfaces and biological species as well as aggregate, depending on the interplay between electrostatic and van der Waals interactions (Brar et al. 2010).

A better understanding of the NP life cycle could allow a better evaluation of their movements among ecosystems and of the transformations that may occur. In this scenario, the environmental risk assessment of NP is important to ultimately develop adequate regulations for NP applications (Auffan et al. 2009a). NP ecotoxicology takes into account parameters such as the type of NP, size, surface properties and possible coatings (Kahru and Dubourguier 2010). Focusing our analysis on the aquatic environment, it is quite difficult to evaluate the fate and environmental impact of NP due to the number of transformations that NP can be subject to, e.g., coagulation, interactions with the humic fraction of natural organic matter (NOM), interactions with clays and natural colloids and many surface property modifications (Figure 1.2) (Lowry et al. 2012; Lin et al. 2010). NP behavior in groundwater is of great importance due to the possible underground accumulation of NP and the consequent risk of contamination of drinking water. TiO<sub>2</sub> NP are among the most used manufactured NP and, con-

sequently, are among the most released in the environment.

Many studies, mainly conducted under simplified conditions with cleaned sand packed into columns, have investigated ionic strength (IS) and pH influences on the transport and retention of  $\text{TiO}_2$  NP in saturated porous media. Chemical parameters are fundamental to the understanding of retention mechanisms because they influence the nanoparticles' surface charge and, consequently, their electrostatic interactions with porous media. Experimental results show that  $\text{TiO}_2$  deposition in sand-packed columns is favored by an acidic or neutral pH, which gives NP a positive or slightly negative surface charge (Chowdhury et al. 2012; Chowdhury et al. 2011; Fang et al. 2013; Godinez and Darnault 2011; Liang et al. 2013b; Solovitch et al. 2010; Wang et al. 2012). Deposition is also enhanced by increased IS, the effects of which depend on the type of ions in solution (Chowdhury et al. 2012; Chowdhury et al. 2011; Fang et al. 2013; Godinez et al. 2013; Godinez and Darnault 2011; Liang et al. 2013b; Solovitch et al. 2010; Wang et al. 2012; Chen et al. 2012; Chen et al. 2011). Other parameters, such as concentration, porous media grain size and pore water velocity, modify the probability that NP will come into contact with collector grains, affecting the deposition rate. Specifically, NP retention increases with a decrease in NP solution concentration and pore water velocity (Chowdhury et al. 2011; Godinez and Darnault 2011; Liang et al. 2013b). According to previous studies, the presence of surfactants, natural organic matter and bacteria can modify the interactions between NP and porous media, resulting in a reduction of NP retention (Chen et al. 2012; Chowdhury et al. 2012; Godinez et al. 2013; Godinez and Darnault 2011; Wang et al. 2012). For more complex porous media, columns of soil (Liang et al. 2013a; Cornelis et al. 2013; Fang et al. 2009) and sand with reactive coatings (Wang et al. 2012; El Badawy et al. 2013) have been used. It was found that  $\text{TiO}_2$  NP are more retained in soils with a high clay content and strong salinity. According to Chrysikopoulos and Syngouna (2014), dense NP transport could be influenced by water flow modifications due to gravity effects.

Few studies were published on the retention of  $\text{TiO}_2$  NP in unsaturated porous media (Fang et al. 2013; Chen et al. 2010; Chen et al. 2008). While the presence of the interface between air and water (AWI), according to Fang et al. (2013), does not enhance the retention of  $\text{TiO}_2$  NP, Chen et al. (2008) shows that the water content influence the retention. According to studies on the transport of other kind of NP and colloids, the AWI, depending on the chemical parameters, can be a collector for charged particles, as  $\text{TiO}_2$  NP are (Kumahor et al. 2015; Bradford and Torkzaban 2008; DeNovio et al. 2004; Corapcioglu and Choi 1996).

One way to evaluate retention mechanism effects is to apply filtration theory (El Badawy et al. 2013; Petosa et al. 2012; Li et al. 2011), which takes into account

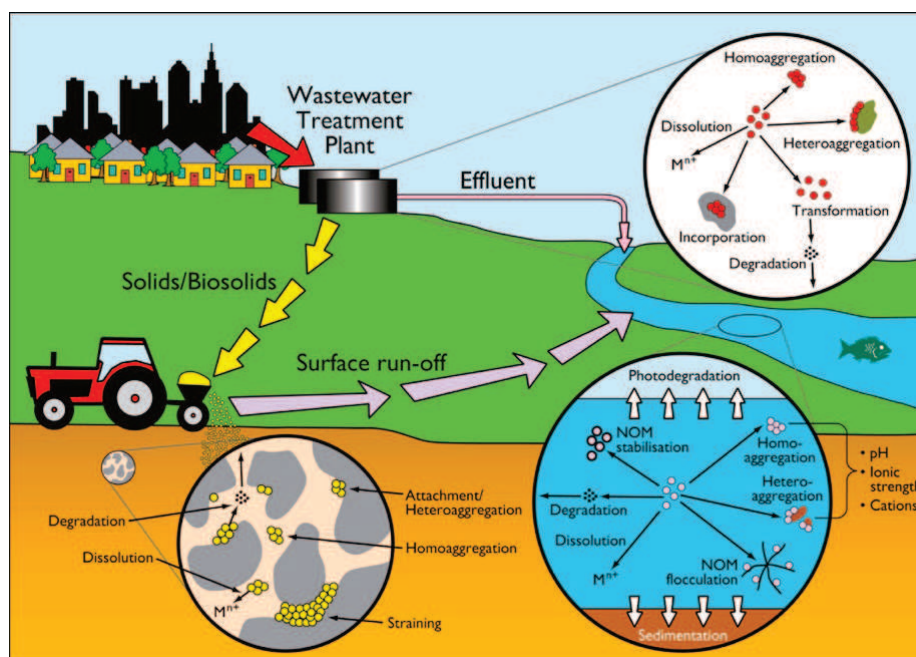


Figure 1.2: Pathways and transformations of the nanoparticles in the environment (Batley et al. 2011). The nanoparticles released in the environment can reach the water bodies directly, e.g. via the wastewater treatment plants effluents, or indirectly, e.g. via the surface run-off. Due to their high reactivity, nanoparticles are expected to interact with each other, with other particles or with natural organic matter. They can lose their nanometrical size if subject to homoaggregation, heteroaggregation, dissolution or degradation. In case of homoaggregation or heteroaggregation, nanoparticles are removed from the water phase due to sedimentation. The fraction of nanoparticles that succeeds in seeping into the soil, can reach the aquifer or be retained by the unsaturated zone of the ground. The nanoparticle retention is controlled by several mechanisms, depending on chemical and physical parameters.

physicochemical conditions and describes the frequency of collisions between NP and collector grains. The parameters of filtration theory offer a simple description of deposition dynamics but can be quite imprecise in some cases. Deviations between predictions and experimental observations are mainly due to repulsive interactions related to the presence of collector surface heterogeneity and of the secondary minima expected by the Derjaguin-Landau-Verwey-Overbeek (DLVO) theory (Tufenkji and Elimelech 2005a). Many studies (Fang et al. 2013; Liang et al. 2013b; El Badawy et al. 2013; Li et al. 2011) have fitted NP breakthrough curves (BTC) to models based on convection-dispersion transport and deposition kinetics, which can simulate different retention mechanisms, such as blocking and straining (Bradford et al. 2011; Bradford et al. 2006). Optimization of the model parameters permits the researcher to better understand the role of the different retention mechanisms and their relevance under different experimental conditions. With regard to the modeling of NP retention under unsaturated conditions, contrary to what was done for colloids (Lenhart and Saiers 2002) and virus transport (Zhang et al. 2012; Anders and Chrysikopoulos 2009), the interface between air and water was never directly taken into account.

#### 1.1.4 COLLOIDAL PARTICLES

All the manufactured NP, due to their size range, fall within the category of colloidal particles. The colloids are suspended particles, natural or synthetic, with a size comprised between 1 nm to 1  $\mu\text{m}$ . Therefore, NP can be seen as a colloid subset. Natural colloids, as clays, metal oxides, the finer sand fraction and organic colloids (e.g., humus, bacterial cells), are fundamental soil components. Their mobility in soils can affect the soil hydraulic properties and, besides, organic and inorganic contaminants are often transported via colloidal particles.

The interest on colloids dates back to the nineteenth century, when Thomas Graham coined the term *colloid* after the Greek word for glue, *κόλλα*. The studies on NP environmental fate are quite recent instead and were born as a branch of the colloid sciences. The theoretical framework used for examining NP transport is the same developed for investigating colloidal transport in porous media. The studies on surface properties, the use of the DLVO theory and of the filtration theory (Section 1.2), which are commonly applied to NP, are drawn from the colloid sciences literature (Vitorge et al. 2013; Huang et al. 2012; Lecoanet et al. 2004; Lyklema 2005).



## 1.2 SURFACE PROPERTIES AND NANOPARTICLES RETENTION

### 1.2.1 DLVO THEORY

The theory that describes the total interaction between charged surfaces in a liquid media was first developed in Derjaguin and Landau (1941) and Verwey and Overbeek (1948). Essentially, the van der Waals attraction and the electric double layer repulsion (EDL) are assumed to be additive and combined to give the total interaction between particles as a function of separation distance. The total potential of interaction  $\Phi_{dlvo}$  [J], is calculated as the sum of the van der Waals attraction  $\Phi_{vdw}$  and of the EDL interaction  $\Phi_{edl}$ :

$$\Phi_{dlvo}(d) = \Phi_{vdw}(d) + \Phi_{edl}(d) \quad (1.1)$$

#### 1.2.1.1 VAN DER WAALS INTERACTION

To understand the interaction potential between charged surfaces, it is necessary to analyze the mutual interaction between molecules. There are three types of interactions at the molecular scale that cause the intermolecular attraction and that are grouped under the name of van der Waals potential (Israelachvili 1985). The sum of these potentials is always attractive, resulting in a short-range attraction that decays rapidly to zero away from a surface and has a range between 0.2 nm and 10 nm. The three types of potentials concerned originate from interaction between different couples of randomly oriented permanent dipoles and induced dipoles:

1. Keesom interaction between permanent dipoles ( $\Phi_{pp}$ );
2. Debye interaction between a dipole and an induced dipole ( $\Phi_{pi}$ );
3. London interaction between two induced dipoles ( $\Phi_{ii}$ ).

$$\Phi_{vdw} = \Phi_{pp} + \Phi_{pi} + \Phi_{ii} \quad (1.2)$$

Hamaker (1937) has derived the following expression for the van der Waals interaction potential between two spheres, assuming that the particle separation distance  $d$  [m] is much larger compared to the two particle radii  $R_1$  and  $R_2$  [m] (Derjaguin approximation) (Figure 1.3):

$$\Phi_{vdw}(x) = -\frac{A_H}{12} \left( \frac{y}{x^2 + xy + x} + \frac{y}{x^2 + xy + x + y} + 2 \ln \frac{x^2 + xy + x}{x^2 + xy + x + y} \right) \quad (1.3)$$

where

$$x = -\frac{d}{2R_1}, \quad y = -\frac{R_2}{R_1} \leq 1 \quad (1.4)$$

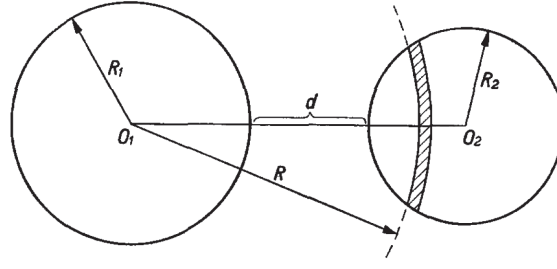


Figure 1.3: Two spherical particles of radii  $R_1$  and  $R_2$ ; the shortest surface-to-surface distance is denoted by  $d$  (Hamaker 1937).

and  $A_H$  [J] is the Hamaker constant, which accounts for materials properties. Its value is comprised between  $10^{-19}$  and  $10^{-20}$  J. For  $x \ll 1$  Equation 1.3 reduces to:

$$\Phi_{vdw}(d) = -\frac{A_H}{6d} \frac{R_1 R_2}{R_1 + R_2} \quad (1.5)$$

Owing to the electromagnetic nature of van der Waals interaction, there is a finite time of propagation between bodies which leads to retardation and to reduced interaction. This effect can become very important at separation distances greater than a few nanometers. Gregory (1981) presents a complete review of the retarded equations for both sphere-sphere and sphere-plate van der Waals interactions:

$$\Phi_{vdw \ s-s}(d) = -\frac{A_H}{6d} \frac{R_1 R_2}{R_1 + R_2} \left[ 1 - \frac{b_1 d}{\lambda_d} \ln \left( 1 + \frac{\lambda_d}{b_1 d} \right) \right], \quad (1.6)$$

$$\Phi_{vdw \ s-p}(d) = -\frac{A_H R}{6d} \left( 1 + \frac{b_2 d}{\lambda_d} \right) \quad (1.7)$$

where  $b_1 = 5.32$ ,  $b_2 = 14.02$  and  $\lambda_d = 100$  nm. The calculation of  $A_H$  for a given material is based on the dielectric permittivity, which is dependent on the frequency of the propagating electromagnetic waves. The combining rules are frequently used to determine approximate values for the unknown Hamaker constant in terms of known constants. For example, the Hamaker constant  $A_{132}$  of the interaction between two materials 1 and 2 immersed in medium 3 can be calculated by:

$$A_{12} = -\sqrt{A_{11} A_{22}}, \quad (1.8)$$

$$A_{132} = A_{12} + A_{33} - A_{13} - A_{23} = \left( \sqrt{A_{11}} - \sqrt{A_{33}} \right) \left( \sqrt{A_{22}} - \sqrt{A_{33}} \right) \quad (1.9)$$

where  $A_{ii}$  is the Hamaker constant of a material in vacuum and  $A_{ij}$  is the Hamaker constant related to the interaction between the materials  $i$  and  $j$  in vacuum. Note

that the van der Waals interaction directly depends on the Hamaker constant: when components 1 and 2 are identical,  $A_{132}$  is positive, therefore, the interaction between identical bodies, in any medium, is always attractive.

### 1.2.1.2 ELECTRICAL DOUBLE LAYER REPULSION

The interaction of charged surfaces in a liquid media is also driven by electrostatic repulsion. Generally, the surfaces are charged and in contact with a solution containing ions that, attracted from the surface or diffused by thermal agitation, form a layer on the interface that screens the charges below. This configuration is called electrical double layer (EDL) (Figure 1.4) and is composed from the Stern or Helmholtz layer, fixed on the surface, and from the diffuse layer of semi-mobile ions. The thickness of double layer, which is called Debye length ( $\kappa^{-1}$  [m]), has a value between 1 nm and 10 nm and depends on the ionic strength  $I$  [mol/m<sup>3</sup>](see section 1.2.2):

$$\kappa^{-1} = \left( \frac{\varepsilon_0 \varepsilon_r k_B T}{2e^2 N_{Av} I} \right)^{1/2} \quad (1.10)$$

where  $e$  [C] is the electron charge,  $k_B$  [J/K] is the Boltzmann constant,  $T$  [K] is the absolute temperature,  $N_{Av}$  [-] is the Avogadro number,  $\varepsilon_0$  [F/m] is the free space permittivity and  $\varepsilon_r$  [-] the liquid relative permittivity. This relation shows that if the ions concentration increases in the fluid, the thickness of the double layer decreases, i.e. the range of the electrostatic forces decreases. If we consider a particle in motion into a fluid, there is a zone around it where the fluid velocity is equal to zero: it is called shear surface and its electric potential is the so-called zeta potential ( $\zeta$  [V]). The surface potential is usually approximated with  $\zeta$ , which can be obtained from electrophoretic mobility measurements.

Hogg et al. (1966) derived an expression for the electrostatic interaction between two spheres, assuming that the EDLs are thin compared with the particle radii ( $\kappa^{-1} \ll R_1, R_2$ ) and in conjunction with the Derjaguin approximation:

$$\Phi_{edl \ s-s}(d) = \frac{\pi \varepsilon_r \varepsilon_0 R_1 R_2}{R_1 + R_2} \left\{ 2\zeta_1 \zeta_2 \ln \left[ \frac{1 + e^{-\kappa d}}{1 - e^{-\kappa d}} \right] + (\zeta_1^2 + \zeta_2^2) + \ln [1 - e^{-2\kappa d}] \right\} \quad (1.11)$$

Equation 1.11 holds exactly for  $|\zeta| < 25$  mV and solution conditions such that the EDL thickness is small compared to the particle size. It can be considered a good approximation until 50-60 mV. Replacing the term  $\frac{R_1 R_2}{R_1 + R_2}$  with the sphere radius  $R$ , we obtain the expression for the sphere-plate interaction.

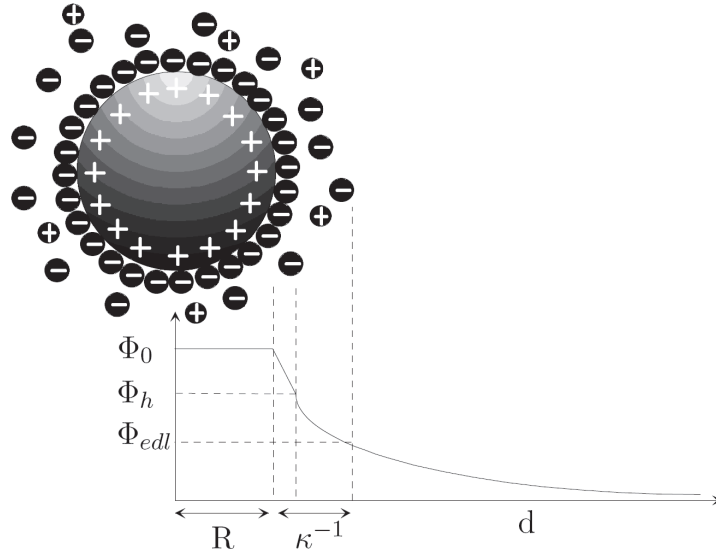


Figure 1.4: Simple model of double layer and its potentials where  $\Phi_0$  is the surface potential,  $\Phi_h$  is the potential of the Helmholtz layer and  $\Phi_{edl}$  is the potential of the double layer.

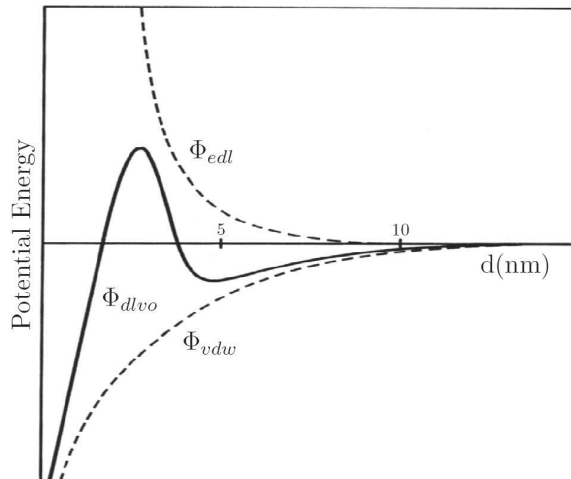


Figure 1.5: Total interaction potential between two surfaces in DLVO theory.

### 1.2.1.3 DLVO ENERGY BARRIER AND NON-DLVO FORCES

Depending on the relative strength of both contributions, the potential versus distance DLVO profile typically displays one of the following three patterns:

1. an infinitely deep minimum, called the primary minimum, at close separation, followed by a maximum, called the energy barrier, and another minimum, called the secondary minimum, occurring at a larger distance (Figure 1.5);
2. an infinitely deep (primary) minimum only;
3. an infinitely deep (primary) minimum plus a large maximum (the energy barrier) but no significant secondary minimum.

The shape of the interaction profile has a direct influence on the kinetics of colloidal aggregation and deposition. In the case of a DLVO profile presenting an infinitely deep minimum only, the interested surfaces will adhere at each contact, due to the van der Waals attraction. If a particle is close to a charged surface with a secondary minimum, it interacts at first with the secondary minimum; then, if the particle energy is large enough to pass the potential barrier, the particle can approach the surface and reach the stronger first minimum, which in the classical DLVO theory has infinite magnitude. The secondary minima are weaker than the primary minima: in a colloidal suspension, they can be responsible for the formation of fairly weak aggregates or, in particle transport through porous media, for reversible deposition. Once the barrier is overcome, the particles are held by van der Waals attraction in a deep primary minimum, from which escape would be very unlikely (Elimelech et al. 1995).

The classical DLVO theory can give physically unrealistic results and cannot describe properly interactions at very small separation distances. The non-DLVO interactions that may occur at the interfaces are still incompletely understood and quantitative theory has not been generally accepted to describe such interactions (Bradford and Torkzaban 2008). For example, hydrophobic interactions may have an important role in colloids and NP attachment at the air-water interface. The origins of hydrophobic forces are still debated but an empirical expression, based on their contact angles, has been proposed to quantify this interaction (Crist et al. 2005; Schafer et al. 1998; Yoon et al. 1997):

$$\Phi_{hyd\ s-p}(d) = -\frac{K_{123}R}{d} \quad (1.12)$$

where  $\Phi_{hyd\ s-p}$  is the interaction potential for a sphere-plate system and  $K_{123}$  can be determined through the following empirical relation:

$$\log K_{123} = a \left( \frac{\cos \theta_p + \cos \theta_2}{2} \right) + b \quad (1.13)$$

where  $\theta_p$  and  $\theta_2$  are the contact angles on the particle surface and on a second surface (e.g., the AWI) and  $a$  and  $b$  are system-specific constants. For the AWI  $\theta_2$  is assumed to be  $180^\circ$ , while  $\theta_p$  depends on the particle nature. Hydrophilic particles have a contact angle  $\theta_p < 30^\circ$ , partially hydrophobic particles have  $30^\circ < \theta_p < 90^\circ$  and hydrophobic particles have  $\theta_p > 90^\circ$  (Lazouskaya et al. 2011).

### 1.2.2 PARTICLE AGGREGATION

In a colloidal suspension, e.g. a  $\text{TiO}_2$  NP suspension, the nature of the interaction profile between the particles is governed by various physicochemical parameters such as particle size, zeta potential, electrolyte composition, ionic strength, pH and Hamaker constant. It is important to understand the role played by each of the parameters in controlling the nature of the interaction profile. Two of the most important parameters are pH and ionic strength. The solution's pH can greatly affect the electric repulsion because, generally, there may be oxygen or nitrogen atoms at the particle surface. In presence of hydrogen, these atoms can be protonated or deprotonated and acquire an electric charge. Thus, as the pH changes, so does the surface charge of the particles. At a given pH, the zeta potential will be equal to zero; this is known as the isoelectric point or point of zero charge (PZC). Clearly, the more the pH is close to the PZC, the more the suspension will tend to aggregate.

The ionic strength of a solution represents the concentration of ions in that solution and is proportional to the salt concentration:

$$I = \frac{1}{2} \sum_{i=1}^n z_i^2 c_i \quad (1.14)$$

where  $n$  [-] is the number of species and  $z_i$  [-] and  $c_i$  [M, mol/L] are the valence and the concentration of the  $i^{\text{th}}$  species. The ionic strength affects both the zeta potential and the double layer thickness: an increase of ionic strength produce a decrease in double layer thickness and a decrease in zeta potential, resulting in a decrease of the electric repulsion.

The potential barrier, preventing contact of particles, prevents aggregation. As the electric repulsion decreases, e.g. for an increase in the salt concentration, the energy barrier becomes lower and contact of the particles can occur more readily. Eventually, the barrier disappears altogether and, in principle, particles can then adhere each time they collide. Such particles are said to be fully destabilized and undergo rapid aggregation. The latter term implies that the rate cannot be further increased by the addition of more salt. The fraction of collisions that are effective is known as the attachment efficiency or sticking factor,  $\alpha_{pp}$  [-]. The

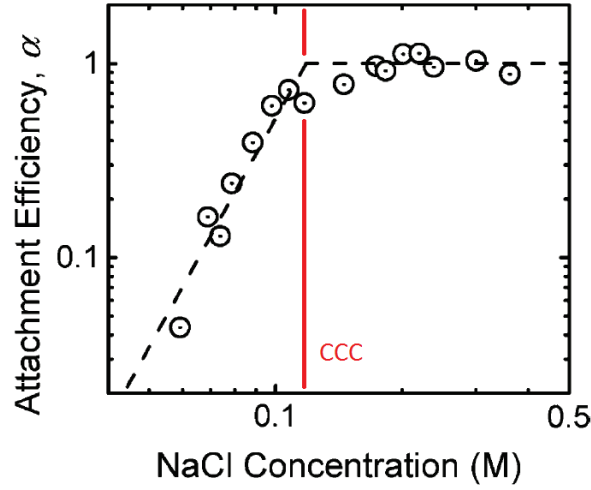


Figure 1.6: Attachment efficiencies of fullerene NP as a function of NaCl concentration at pH 5.2. The CCC based on these data is 120 mM NaCl (Chen and Elimelech 2006).

reciprocal of this value is known as the stability ratio,  $W$  [-]:

$$W = \frac{1}{\alpha_{pp}} = \frac{\left(\frac{dR(t)}{dt}\right)_{t \rightarrow 0}}{\left(\frac{dR(t)}{dt}\right)_{t \rightarrow 0, fast}} \quad (1.15)$$

where the fast term is the rate of aggregation under most favorable aggregation conditions. By measuring the rate of aggregation as a function of salt concentration, it is possible to find the critical concentration at which the onset of rapid flocculation occurs. The transition from kinetic stability to rapid aggregation occurs over a very narrow range of electrolyte concentrations, around the critical coagulation concentration (CCC) which may be estimated by assuming that no energy barrier exists. The salt concentration at which  $W$  (or  $\alpha_{pp}$ ) plot changes the slope is the CCC (Figure 1.6).

### 1.2.3 FILTRATION THEORY

In classical filtration theory, the porous media is idealized as a bed of spherical collectors (grains) each completely surrounded by a film of fluid (Happel sphere). Particles transported within the film of fluid surrounding the idealized collector may intercept the surface through three mechanisms (Figure 1.7):

1. The particle may leave the streamline due to his own size (*interception*);
2. The particle, if it has a density greater than that of water, may leave the streamline due to the gravitational force (*sedimentation*);

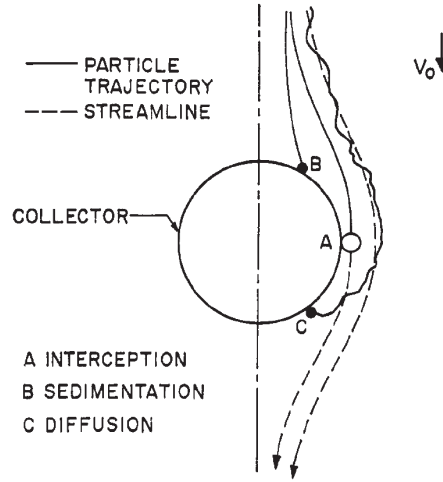


Figure 1.7: A suspended particle may leave the streamline and come in contact with a collector through three mechanisms (Yao et al. 1971).

3. The particle may leave the streamline due to its Brownian movement, when larger than the fluid drag (*diffusion*).

The deposition kinetic is determined from the rate at which collisions occur between particles and collectors (single collector efficiency  $\eta_0$  [-]), and from the probability that collisions result in adhesion (attachment efficiency  $\alpha_{pc}$  [-]).

$$\eta_0 = \frac{\text{rate of particle-collector collisions}}{\text{rate of approaching particles}} \quad (1.16)$$

$$\alpha_{pc} = \frac{\text{rate of collisions resulting in adhesion}}{\text{rate of particle-collector collisions}} \quad (1.17)$$

#### 1.2.3.1 ATTACHMENT EFFICIENCY

Since in the literature there is no consensus about  $\alpha_{pc}$  behavior, it is often empirically determined. Attachment efficiency  $\alpha_{pc}$  has been traditionally considered as related to physical-chemical factors only (e.g., solution ionic strength and surface potentials). Elimelech (1992) developed a semiempiric model predicting  $\alpha_{pc}$  from the surface potentials of collector and particles. Its dependence on hydrodynamic factors is still a controversial topic: if  $\alpha_{pc}$  is assumed to be unaffected by water velocity in Elimelech (1992), elsewhere, a decrease (Anders and Chrysikopoulos 2005; Lecoanet et al. 2004) or an increase (Kim and Lee 2014) is observed when the water velocity increases. Other studies reported the existence of a critical flow velocity (Shen et al. 2010; He et al. 2009), justified through the torque balance.

The torque analysis approach compares the adhesive torque ( $T_{\text{adhesive}}$  [N m]) and the hydrodynamic torque ( $T_{\text{hydrodynamic}}$ ) that a particle experiences on a collector surface, in order to predict his behavior (Figure 1.8). The adhesive



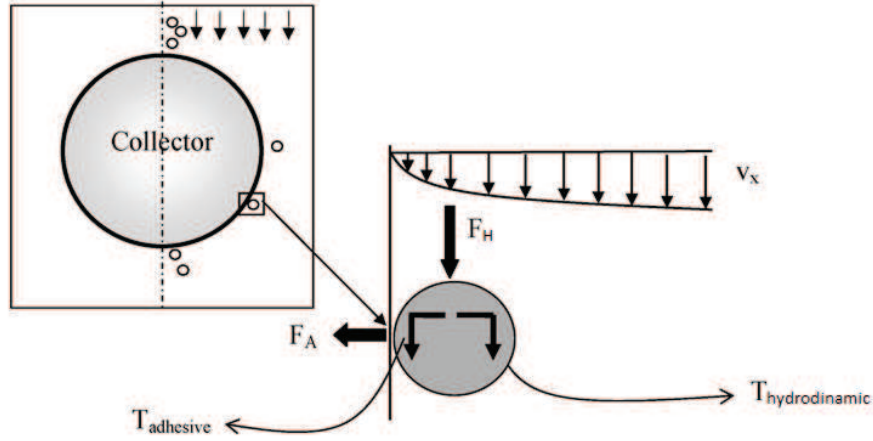


Figure 1.8: Schematic of the torques experienced from a transported particle that came in contact with a collector surface. The hydrodynamic torque acting on the particle,  $T_{hydrodynamic}$ , is due to the drag force applied by the fluid flow,  $F_H$ . The adhesive torque,  $T_{adhesive}$ , is caused by the adhesive (DLVO) force acting between the collector and particle surfaces,  $F_A$  (Torkzaban et al. 2007).

torque depends on the surface properties of collectors and particles, whereas the hydrodynamic torque increases with the water velocity. According to Shen et al. (2010), water velocity can increase without affecting the attachment efficiency until the hydrodynamic drag attains the adhesive torque (due to the primary or secondary minimum). Once the hydrodynamic torque is larger than the adhesive torque, any further water velocity increase affects  $\alpha_{pc}$ . Kim and Lee (2014) too argue about a water velocity critical value, but, while Shen et al. (2010) affirm that beneath the critical value,  $\alpha_{pc}$  is constant, Kim and Lee (2014) consider that  $\alpha_{pc}$  increases beneath the critical value and decreases for larger velocities. According to Kim and Lee (2014),  $\alpha_{pc}$  increases with water velocity, when hydrodynamic torque is smaller than the adhesion torque, presumably because an increase of mass transfer from NP to the collectors could result in a higher chance of particle collisions and therefore an increase in  $\alpha_{pc}$ . It should be noted that the last statement is quite in conflict with the definition of attachment efficiency.

### 1.2.3.2 SINGLE COLLECTOR EFFICIENCY

The single collector efficiency  $\eta_0$  depends on physicochemical parameters (e.g., collector size, particle size, Hamaker constant, etc) and hydrodynamic parameters (water velocity). A model for  $\eta_0$  based on five dimensionless parameters ( $N_R$ ,  $N_{Pe}$ ,  $N_{vdw}$ ,  $N_A$ ,  $N_G$ ) is developed in Tufenkji and Elimelech (2004):

$$\eta_0 = \eta_D + \eta_I + \eta_G \quad (1.18)$$

$$\eta_D = 2.4A_S^{1/3}N_R^{-0.081}N_{Pe}^{-0.0715}N_{vdw}^{0.052} \quad (1.19)$$

$$\eta_I = 0.55A_S N_R^{1.675} N_A^{-0.125} \quad (1.20)$$

$$\eta_G = 0.22N_R^{-0.24}N_G^{1.11}N_{vdw}^{0.053} \quad (1.21)$$

where subscripts D, I, and G represent contributions related to diffusion, interception and sedimentation. The dimensionless parameters are defined in Table 1.1. The model accounts for the different forces that act on a particle following the streamline (contributions of convective and diffusive transports, van der Waals force, thermal agitation, gravitational force) evaluating the probability of a particle-collector contact. For small size particles, such as NP,  $\eta_0$  is mainly determined from molecular diffusion ( $\eta_D$ ), while interception ( $\eta_I$ ) is dominant for larger particles. Under these conditions the single collector efficiency is strongly dependent on water velocity: it decreases when the water velocity increases. This is because the probability of a small particle, whose main removal mechanism is diffusion, to leave the streamline is inversely proportional to the ratio of convective to diffusive transport (Peclet number).

#### 1.2.4 RETENTION AT THE AIR-WATER INTERFACE

Unsaturated porous media are more complex than saturated porous media due to the presence of an additional phase. The solid phase and the liquid phase coexist in fact with a third phase, the gaseous phase. The presence of air in the poral space adds a surface of contact, which increases the number of retention sites: a suspended particle can interact with both the interface between the liquid phase and the solid phase and the interface between the liquid phase and the gaseous phase. The air-water interface (AWI) has been reported to be negatively charged, with measured zeta potential values that range from -15 mV to -65 mV (Bradford and Torkzaban 2008).

The nature of the forces experienced from a particle at the AWI is still poorly understood. The DLVO theory cannot explain any particle retention at the AWI, since the potential of interaction of a particle in its neighborhood is repulsive. Just adding hydrophobic interactions or other non-DLVO forces it is possible to obtain an attractive interaction. Several studies have shown that during drainage and imbibition events the movement of the AWI can result in particle remobilisation. The particles retained at the AWI are concerned, but also those retained at

Parameter	Definition
$A_s = \frac{2(1 - \gamma^5)}{2 - 3\gamma + 3\gamma^5 - 2\gamma^6}$	Porosity ( $\phi$ [-]) dependent parameter, where $\gamma = (1 - \phi)^{1/3}$ .
$N_R = \frac{d_p}{d_c}$	Aspect ratio, where $d_p$ [m] is the nanoparticle diameter and $d_c$ the collector diameter.
$N_{Pe} = \frac{q_d d_c}{D_\infty}$	Peclet number, where $q_d$ [m/s] is the Darcy velocity and $D_\infty$ is the diffusion coefficient. Ratio of convective to diffusive transport.
$D_\infty = \frac{k_B T}{3\pi\mu d_p}$	Diffusion coefficient described from the Stokes-Einstein equation, where, $k_B$ is the Boltzmann constant, $T$ is absolute temperature and $\mu$ [Pa s] is fluid viscosity.
$N_{vdw} = \frac{A_H}{k_B T}$	van der Waals number, where $A_H$ is the Hamaker constant. Ratio of van der Waals interaction energy to particle's thermal energy.
$N_A = \frac{N_{vdw} D_\infty}{d_p}$	Attraction number, which represents combined influence of vdW attraction forces and fluid velocity on particle deposition rate due to interception.
$N_G = \frac{d_p^2 (\rho_p - \rho_f) g}{18\mu q_d}$	Gravity number, where $g$ [m/s <sup>2</sup> ] is the gravitational acceleration, $\rho_p$ [kg/m <sup>3</sup> ] and $\rho_f$ are particle and fluid density. Ratio of Stokes particle settling velocity to Darcy velocity.

Table 1.1: Parameters used in Tufenkji and Elimelech (2004) single collector efficiency calculation and their definitions.

the sand water interface (SWI) can be mobilized from the moving contact line between the AWI and the SWI (Lazouskaya et al. 2011).

Several methods for measuring AWI have been proposed, but the results are not always consistent with each other (Costanza-Robinson and Brusseau 2002). Mathematical models to quantify the specific AWI are based on the Mualem-van Genuchten parameters or on the surface tension and capillary force. Roughly, the AWI is expected to increase when saturation decreases.

#### 1.2.5 OTHER RETENTION MECHANISMS

Idealizing the porous media as composed of isolated spherical collectors, filtration theory neglects pore structure and grain-grain junctions, and thus cannot account for retention mechanisms related to the irregular shape of grains and pores, such as *straining* and *wedging* (Figure 1.9).

In case of particles with a diameter larger than the pore size, the particles are completely mechanically filtered. Similar to mechanical filtration, straining of particles occurs in pores and depends on the ratio of the particle and pore size. In contrast to mechanical filtration, straining only occurs in a fraction of the pore space, and particle transport can still occur in the larger portions of the continuous pore networks. If particles encounter these smaller pores, they can become physically entrapped as a result of straining, potentially producing *size exclusion*. Size exclusion affects the mobility of particles by constraining them to more conductive flow domains and larger pore networks that are physically accessible. As a result, colloids can be transported faster than a conservative solute tracer (Bradford et al. 2006).

Wedging of particles occurs in zones of flow stagnation, as grain to grain contacts and blind pores. Since convection is not possible in null water velocity zones, they can be reached through molecular diffusion only. For the same reason, flow stagnation zones are expected to be the ultimate locations of retention of secondary-minimum associated particles (Johnson et al. 2007).

Often, even under unfavorable conditions, i.e. in presence of a DLVO energy barrier, attachment may occur. A valuable body of research has been generated demonstrating that surface charge heterogeneity and nanoscale roughness can reduce or eliminate the energy barrier that would otherwise be expected, allowing thus particle attachment (Shen et al. 2014; Bradford et al. 2006; Shellenberger and Logan 2002).

### 1.3 FLOW AND MASS TRANSFER IN POROUS MEDIA

In general, a porous medium is defined as a set of solid grains, surrounded by empty spaces that can communicate with each other or not. These spaces con-

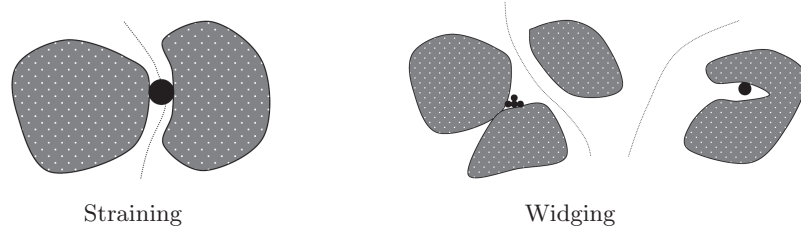


Figure 1.9: Retention mechanisms related to grains irregularities.

stitute the so-called pore space, which can be occupied by air, water or other fluids. In unsaturated porous media, the hydraulic state can be defined by two main variables: the volumetric water content  $\theta$  [m<sup>3</sup>/m<sup>3</sup>] and the pressure head  $h$  [m]:

$$h = \frac{p - p_a}{\rho_f g}, \quad \theta = \frac{V_w}{V_t} \quad (1.22)$$

where  $p_a$  [Pa] is the atmospheric pressure,  $V_t$  [m<sup>3</sup>] is the total volume of the porous medium,  $V_w$  is the volume of water,  $\rho_f$  [kg/m<sup>3</sup>] is the water density,  $g$  [m/s<sup>2</sup>] is the acceleration due to gravity and  $p$  [Pa] is the water pressure in the pores. The water content at saturation,  $\theta_s$ , never reaches the porosity  $\phi$  [-], i.e., the ratio between pore volume and  $V_t$ , since some air bubbles are always present. The pressure head  $h(\theta)$  in unsaturated condition has negative values and loses its physical meaning of pressure: it is replaced by the matric potential  $\Psi(\theta)$  [Pa]. This matric potential takes into account the contribution of the interactions between water and the solid grains to the energy state of pore water.

For a formal mathematical description of water flow in porous media, we assume the porous medium as rigid and continuous and the fluid phase as continuous. The value of each physical variable assigned to a point in continuum space is obtained by locally averaging the actual physical property over a representative elemental volume (REV). This hypothesis of continuity allows to employ the differential equation that describes the water flow in porous media, based on a combination of the mass conservation law and a law of dynamic behavior called Darcy's law.

### 1.3.1 EQUATION OF FLOW

If  $\theta_r$  is the minimum water quantity that cannot be extracted from a porous media sample and  $\theta_s$  the maximum quantity of water contained in the same sample, the dimensionless effective saturation  $S_e$  [-] is defined as:

$$S_e = \frac{\theta - \theta_r}{\theta_s - \theta_r} \quad (1.23)$$

where  $0 \leq S_e \leq 1$ , being  $0 < \theta_r < \theta_s < \phi < 1$ . Therefore the conservation of mass, if grains can be considered incompressible, is expressed from the continuity equation:

$$\frac{\partial(\phi S_e)}{\partial t} = -\nabla \cdot \vec{q}_D \quad (1.24)$$

where  $\vec{q}_D$  [m/s] is the Darcy flux, which is the product of the pore water velocity  $\vec{v}$  [m/s], averaged over the REV, and the water content  $\theta$ . The vector  $\vec{q}_D$  is related to the gradient of the hydraulic head  $H = h - z$  [m] ( $z$  represents the soil depth and therefore increases downwards) from the Darcy's law:

$$\vec{q}_D = -K(h)\nabla H \quad (1.25)$$

The hydraulic head is the sum of the gravity potential and of the pressure or matric potential. It represents the energy of the water in the soil and his gradient is responsible for water flow. The hydraulic conductivity  $K(h)$  [m/s] represents the capacity of the porous medium to drive the water and depends on the structure of the solid matrix, on fluid properties and, for unsaturated condition, on the water content. If the medium is saturated, every pore is involved in the flow and the conductivity has the highest value ( $K = K_s$ ):

$$K_s = \kappa_i \frac{\rho_f g}{\mu} \quad (1.26)$$

where the intrinsic permeability of the soil  $\kappa_i$  [m<sup>2</sup>] depends just on solid matrix properties. On the contrary, in an unsaturated medium, the pores are partially occupied by air and, therefore, only a portion of the pore space is involved in the flow. The movement of water in an unsaturated medium is described by the general equation of flow, which comes from (1.24) and (1.25) and is called Richards equation (here in its vertical one-dimensional form):

$$\frac{\partial \theta}{\partial t} = \frac{\partial}{\partial z} \left[ K(h) \left( \frac{\partial h}{\partial z} - 1 \right) \right] \quad (1.27)$$

where water is assumed incompressible, air phase is assumed highly mobile and its equilibrium with the atmosphere instantaneously attained.

### 1.3.2 SOIL HYDRODYNAMIC PROPERTIES

A definition of  $K(h)$  and  $\theta(h)$  is required to solve the Richards Equation. Several empirical relations are proposed in the literature, involving hydrodynamic parameters that characterize the porous medium. The number of parameters is variable and some of them cannot be directly measured. The van Genuchten-Mualem model is one of the most widely used (van Genuchten 1980):

$$\theta(h) = \begin{cases} \theta_r + \frac{\theta_s - \theta_r}{[1 + |\alpha h|^n]^m} & h < 0 \\ \theta_s & h \geq 0 \end{cases} \quad (1.28)$$

$$K(h) = K_s S_e^l \left[ 1 - \left( 1 - S_e^{1/m} \right)^m \right]^2 \quad (1.29)$$

with  $m = 1 - 1/n$ ,  $n > 1$ , where  $n$  [-] is the pore size distribution index,  $\alpha$  [ $\text{m}^{-1}$ ] is related to the inverse of the characteristic pore radius and  $l$  [-] is the pore connectivity parameter. The parameters cannot be determined unambiguously for a soil because of the hysteretic effect, which is described in the next section. Therefore the parameters of the model must be empirically determined for each process of drainage or imbibition.

#### 1.3.2.1 HYSTERESIS

Hysteresis refers to the nonunique relationship between the pressure head ( $h$ ) and the water content ( $\theta$ ), in the soil water retention function  $\theta(h)$  (figure 1.10). This relationship displays considerable variations in  $\theta$  for the same  $h$ , depending upon the history of soil wetting and drying. During wetting, when the water content and the pressure head are monotonically increasing, the retention curve can be described by a unique function. Similarly, during drying, when the water content and the pressure head are monotonically decreasing, the retention curve can also be described by a unique but different function. When drying reverses into a wetting process and vice versa,  $\theta(h)$  is no longer unique and hysteresis must be introduced (Russo et al. 1989). This behavior is due to several factors (Hillel 1982):

1. geometric nonuniformity of individual pores, resulting in the so called *ink bottle effect*;
2. different spatial connectivity of pores during drying or wetting process;
3. variations in liquid-solid contact angle;
4. air entrapment.

#### 1.3.3 SOLUTE TRANSPORT EQUATION

The transport in porous media is a process governed by the principle of conservation of mass and by three basic mechanisms: convection, hydrodynamic dispersion and molecular diffusion.

For convection, the solute is transported by the general movement of water with a discharge  $\vec{q}_{conv}$  [ $\text{kg}/\text{m}^2/\text{s}$ ]:

$$\vec{q}_{conv} = C \vec{q}_D = \theta C \vec{v} \quad (1.30)$$

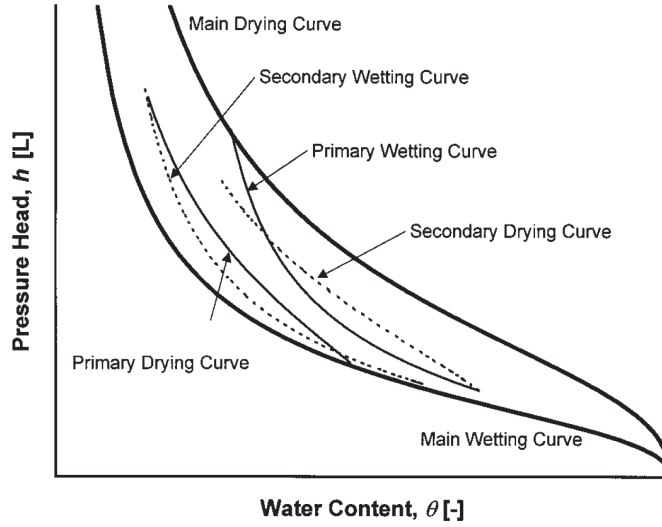


Figure 1.10: Idealized hysteretic soil water retention function (Šimunek et al. 1999).

where  $C$  is the solute concentration [kg/L],  $\vec{q}_D$  is the Darcy flux and  $\vec{v}$  the pore water velocity. Even in absence of fluid flow, solutes diffuse in all directions of space, from the highest concentrations to the lowest concentrations. The result is a process of molecular diffusion with discharge  $\vec{q}_{dif}$ :

$$\vec{q}_{dif} = -\theta d_m \cdot \nabla C \quad (1.31)$$

where the  $d_m$  [m<sup>2</sup>/s] coefficient is the diffusion coefficient in the porous medium. It depends on the porosity of the medium and on the water content and can be expressed as:

$$d_m = D_\infty \tau_w(\theta), \quad \tau_w(\theta) = \frac{\theta^{\frac{7}{3}}}{\phi^2} \quad (1.32)$$

where  $D_\infty$  [m<sup>2</sup>/s] is the molecular diffusion coefficient (Table 1.1),  $\tau_w$  [-] is the tortuosity factor and the relation on the right is the model proposed by Millington and Quirk (Dane and Topp 2002).

Solutes cannot move along a straight line, but must follow the tortuous pore network. In case of movement of water, the dispersion of solutes is increased due to the variability of speed within a single pore and between different pores and due to the tortuosity of the medium. The mixing is improved substantially in the direction of flow. This process is called hydrodynamic dispersion and is often related to the concentration gradient by a linear relationship (Freeze and Cherry 1979):

$$\vec{q}_{disp} = \theta \cdot \hat{D} \cdot \nabla C \quad (1.33)$$



where  $\widehat{D}$  [m<sup>2</sup>/s] is the hydrodynamic tensor.  $\widehat{D}$  can be related to the properties of the solid matrix and of the flow by a linear relationship with longitudinal and transverse dispersivity ( $\alpha_L, \alpha_T$  [m]) and Darcy flux ( $|q_D|$ ):

$$\begin{cases} \widehat{D}_L = \alpha_L \cdot |q_D| \\ \widehat{D}_T = \alpha_T \cdot |q_D| \end{cases} \quad (1.34)$$

The dispersivity depends directly on the scale of the studied porous medium. Its value can vary from millimeters in a laboratory experiment to meters in a large scale field experiment. According to some studies (Nutzmann et al. 2002; Maraqa et al. 1997), the dispersivity values under unsaturated conditions are expected to be higher than under saturated conditions because of the increased velocity fluctuations for different pathways. The presence of air in the pore space could make the path more tortuous for water and solutes and thus increase the apparent tortuosity and dispersivity of the medium. Nevertheless, there is no general agreement in the literature on this behavior (Vanderborght and Vereecken 2007).

The effects of the different mechanisms are summarized in the convection-dispersion equation (CDE), which, in its one dimensional form, is written as:

$$\frac{\partial \theta C}{\partial t} = \frac{\partial}{\partial z} \left( \theta D \frac{\partial C}{\partial z} \right) - \frac{\partial q_D C}{\partial z} \quad (1.35)$$

The left term of the equation represents the variation of the stock of solute, the right term is the sum of a dispersive term (first term) and a convective term (second term). The dispersive term  $D$  contains both hydrodynamic dispersion and molecular diffusion. Unless for very small velocities, molecular diffusion can be neglected and  $D$  approximated with  $D_L$ .

During the transport of NP, kinetic retention can occur. The dynamic deposition process can be described by a first order attachment rate, with a blocking function:

$$\rho \frac{\partial s}{\partial t} = \theta k_a \psi C \quad (1.36)$$

where  $s$  [kg/kg] is the particle concentration in the solid phase,  $k_a$  [s<sup>-1</sup>] is the particle attachment rate and  $\psi$  [-] is the blocking function. The attachment coefficient  $k_a$  can be obtained empirically or through filtration theory (Ma et al. 2009):

$$k_a = \frac{3(1-\phi)q_D}{2d_c\phi} \alpha_{pc}\eta_0 \quad (1.37)$$

Since the idealized porous medium has a limited amount of attachment sites, an attached particle reduces the sites available for deposition: this is the so-called *blocking* process. Deposited particles may therefore prevent the future

attachment of further particles. The blocking function  $\psi$  models this behavior, inducing a decrease in the deposition rate as the amount of attached particles increases. A linear Langmuirian approach can be used to derive the form of the blocking function, obtaining (Adamczyk et al. 1994):

$$\psi = 1 - \frac{s}{s_{max}} \quad (1.38)$$

where  $s_{max}$  is the maximum retention capacity of the porous medium, or the number of available attachment sites. It must be empirically determined.

The Langmuirian model is based on the assumption that monolayers of particles are deposited, it does not take into account the possibility that attached particles could act as collectors for other particles deposition. This phenomenon, termed *ripening*, induces the increase of the number of available attachment sites and can be important for large surface coverage or high degree of surface heterogeneity (Camesano et al. 1999).

The retention term with a Langmuirian dynamic can be added to Equation 1.35, obtaining:

$$\begin{cases} \frac{\partial \theta C}{\partial t} + \rho \frac{\partial s}{\partial t} = \frac{\partial}{\partial z} \left( \theta D \frac{\partial C}{\partial z} \right) - \frac{\partial q_D C}{\partial z} \\ \rho \frac{\partial s}{\partial t} = \theta k_a \psi C \\ \psi = 1 - \frac{s}{s_{max}} \end{cases} \quad (1.39)$$

The equations of flow and transport can be analytically solved only in particular cases, with simple geometry domains, simple boundary conditions and for homogeneous media. In more general conditions, it is necessary to employ a numerical solution of the equations. Furthermore, the physical data are available in a limited number of points and characterized from a fixed sampling rate, so that only a discretized model of simulation gives a solution that can be validated from the data. The discretization of the differential equations can be seen as a numeric approximation of the solution or as a discrete model that replaces the differential equations with a system of algebraic equations. The most frequently employed techniques of modeling in the geophysical field are the finite differences and the finite elements approaches.

## 1.4 INVERSE PROBLEM RESOLUTION

In order to apply a model to an experimental set of data, it is necessary to calibrate it by means of the parameter optimization. Parameter optimization is an indirect approach for the estimation of soil hydraulic and/or solute transport parameters from transient flow and/or transport data. Inverse methods are

typically based upon the minimization of a suitable objective function, which expresses the discrepancy between the observed values and the predicted system response. Firstly, it is necessary to select a proper objective function and the minimization method. In this work the adopted objective function  $O(\mathbf{p})$  is the sum of the square residuals between the observed and the calculated  $N$  values, and  $\mathbf{p} = \{p_1, \dots, p_{np}\}$  is the vector of the  $np$  parameters to be optimized:

$$O(\mathbf{p}) = [\mathbf{h}(\mathbf{p}) - \hat{\mathbf{h}}]^T \mathbf{W} [\mathbf{h}(\mathbf{p}) - \hat{\mathbf{h}}] \quad (1.40)$$

where  $\hat{\mathbf{h}}$  is the vector of the measured values,  $\mathbf{h}(\mathbf{p})$  is the vector of the values computed with the parameter set  $\mathbf{p}$  and  $\mathbf{W}$  is the inverse of the covariance matrix of the measurement errors. The best fitting parameters are those that minimize this objective function through the Levenberg-Marquardt optimization algorithm (Marquardt 1963).

#### 1.4.1 LEVENBERG-MARQUARDT ALGORITHM

The minimization of the objective function is conducted by searching, in an iterative manner, the minimum of  $O(\mathbf{p})$ , by varying the  $\mathbf{p}$  value. We approximate  $O(\mathbf{p})$  locally with a quadratic expansion (Roth 2012):

$$O(\mathbf{p} + \Delta\mathbf{p}) = O(\mathbf{p}) + [\nabla O(\mathbf{p})]^T \Delta\mathbf{p} + \Delta\mathbf{p}^T [\nabla^2 O(\mathbf{p})] \Delta\mathbf{p} + \dots \quad (1.41)$$

The objective function minimum is reached when the gradient is null:

$$\nabla O(\mathbf{p} + \Delta\mathbf{p}) = \nabla O(\mathbf{p}) + [\nabla^2 O(\mathbf{p})]^T \Delta\mathbf{p} + \dots = 0 \quad (1.42)$$

that is:

$$[\nabla^2 O(\mathbf{p})]^T \Delta\mathbf{p} = -\nabla O(\mathbf{p}) \quad (1.43)$$

If the starting point is close to the minimum, where we can assume the difference between computed values and measured values as small, Equation (1.43) can be written as follows:

$$(J^T W J) \Delta\mathbf{p} = -[\mathbf{h}(\mathbf{p}) - \hat{\mathbf{h}}]^T W J \quad (1.44)$$

where  $J$  is the Jacobian matrix of the derivatives of  $\mathbf{h}(\mathbf{p})$  with respect to parameters. The assumption of being near to the minimum can be relaxed through the Levenberg-Marquardt approach, that brings:

$$(J^T W J + \lambda I) \Delta\mathbf{p} = -[\mathbf{h}(\mathbf{p}) - \hat{\mathbf{h}}]^T W J \quad (1.45)$$

where  $\lambda$  is a number,  $I$  is the identity matrix. Equations (1.44) and (1.45) are systems of  $np$  equations that can be solved providing the  $np$  increments  $\Delta\mathbf{p}$ .

The choice of the value of  $\lambda$  is not straightforward and it determines the speed of convergence, but not the final result. A simple approach is to initially set to a high value the Marquardt parameter  $\lambda$  to start with, and to check whether the the objective function decreases or not. If the objective function decreases,  $\lambda$  can be decreased, otherwise we are too far away from the minimum and  $\lambda$  must be increased.

The iterations stop when either of the following conditions is met (Toride et al. 1995):

1. the relative change in each estimation parameter ( $\Delta p_i/p_i$ ) is less than  $5.0 \times 10^{-4}$ ;
2. the relative decrease in  $O(\mathbf{p})$  is less than  $1.0 \times 10^{-6}$  for three successive iterations;
3.  $O(\mathbf{p})$  decreases more than 100 times without meeting either condition (1) or (2);
4.  $O(\mathbf{p})$  fails to decrease during 50 consecutive iterations.

#### 1.4.2 GRADIENT AND HESSIAN CALCULATION

An important role in the algorithm is played by the derivatives calculation. The gradient of the objective function is obtained with (1.40):

$$\nabla O(\mathbf{p}) = 2 \left[ \mathbf{h}(\mathbf{p}) - \hat{\mathbf{h}} \right]^T \mathbf{W} \frac{\partial \mathbf{h}(\mathbf{p})}{\partial \mathbf{p}} = 2 \left[ \mathbf{h}(\mathbf{p}) - \hat{\mathbf{h}} \right]^T \mathbf{W} \mathbf{J}(\mathbf{p}) \quad (1.46)$$

where  $\mathbf{J}(\mathbf{p})$  is the Jacobian matrix. If we take a further derivative:

$$\nabla^2 O(\mathbf{p}) = 2 \left\{ \left[ \mathbf{h}(\mathbf{p}) - \hat{\mathbf{h}} \right]^T \mathbf{W} \frac{\partial^2 \mathbf{h}(\mathbf{p})}{\partial \mathbf{p}^2} + \mathbf{J}(\mathbf{p})^T \mathbf{W} \mathbf{J}(\mathbf{p}) \right\} \quad (1.47)$$

Ignoring the term with the second derivative in the right hand side of (1.47) and writing  $\mathbf{J}(\mathbf{p}) = \mathbf{J}$  (Press et al. 1992), we obtain:

$$\nabla^2 O(\mathbf{p}) = 2 \mathbf{J}^T \mathbf{W} \mathbf{J} \quad (1.48)$$

The approximation is motivated by the following facts:

- Calculating the second derivative is computationally expensive;
- In the neighborhood of the minimum and for a correct model, the deviations  $\mathbf{h}(\mathbf{p}) - \hat{\mathbf{h}}$  approach a random noise that is not correlated with the model parameters; this part of the equation thus tends to cancel out when summed over  $N$ ;
- Approximations of  $H$ , even very crude ones, only affect the path to the result, but not its final value.

### 1.4.3 ERROR ANALYSIS OF ESTIMATED PARAMETERS

The squared uncertainty of the optimal parameter set  $\hat{\mathbf{p}}$ , when the measurement errors are unknown, can be defined as:

$$(\mathbf{p} - \hat{\mathbf{p}})^T (\mathbf{p} - \hat{\mathbf{p}}) = \frac{O(\hat{\mathbf{p}})}{N - np} F_\alpha (\mathbf{J}^T \mathbf{W} \mathbf{J})^{-1} \quad (1.49)$$

When  $F_\alpha$  value is set to the unity, the right hand side of Equation (1.49) corresponds to the covariance matrix ( $\text{Cov}_{ij}$ ), whose diagonal elements, root squared, provide an estimation of the *standard error*.  $F_\alpha$  depends on the accepted risk (in statistical sense), on the number of degrees of freedom  $N - np$  and on a  $\chi^2$  distribution. When the number of degrees of freedom reaches a large value (e.g. 100),  $F_\alpha$  can be determined through a Fisher's distribution, since the  $\chi^2$  distribution became a normal distribution. For a *confidence interval* which will have the 95% of probability of containing the true values,  $F_\alpha = 1.96$ . From the covariance matrix, the correlation matrix is calculated as:

$$\text{Cor}_{ij} = \frac{\text{Cov}_{ij}}{\sqrt{\text{Cov}_{ii} \text{Cov}_{jj}}} \quad (1.50)$$

This square matrix is symmetric and dimensionless and its diagonal elements are always equal to the unity. The off-diagonal elements have values between -1 and 1. The closer an element is to the extremes, the more correlated or anti-correlated are the involved parameters. A strong correlation between two parameters means that it is not possible to identify them uniquely and it is better to fix the value of one of them. The correlation coefficients must be less than the critical value 0.95 (Hill 1998).

Important measures of the goodness of fit are given by the value of the objective function, which must be small, and by the  $R^2$  value for regression of the observed ( $\hat{h}_i$ ) versus fitted ( $h_i$ ) values:

$$R^2 = \frac{\left[ \sum \hat{h}_i h_i - \sum \hat{h}_i \sum h_i \right]^2}{\left[ \sum \hat{h}_i^2 - \left( \sum \hat{h}_i \right)^2 \right] \left[ \sum h_i^2 - \left( \sum h_i \right)^2 \right]} \quad (1.51)$$

There is not a parameter that is alone sufficient to determine the best fit. It is necessary, looking to data and model graphics, to adjust the starting point for the parameter optimization searching for an  $R^2$  value as near as possible to the unity and, at the same time, an objective function value as near as possible to zero.

Other criteria, which include the number of parameters  $np$ , can be used to compare different models. The Akaike information criterion (AIC) and the Bayesian

information criterion (BIC) give a measure of the relative quality of a model for a given set of data. Both are function of the residual sum of squares:

$$AIC = N \log \frac{\sum (\hat{h}_i - h_i)^2}{N} + 2np \quad (1.52)$$

$$BIC = N \log \frac{\sum (\hat{h}_i - h_i)^2}{N} + np \log N \quad (1.53)$$

Both criteria take into account the number of parameters  $np$ , but the BIC introduce a larger penalty term for the number of parameters, to prevent overparameterization and overfitting. Models associated with smaller values of a given criterion are ranked higher than those associated with larger values. These criteria do not provide an absolute evaluation of the quality of a fit, the absolute value of the criterion being irrelevant, but just a means for model selection (Riva et al. 2011; Ye et al. 2008).



## CHAPTER 2

---

### MATERIALS CHARACTERIZATION

---

#### CONTENTS

2.1	Nanoparticles Characterization . . . . .	61
2.2	Sand Characterization . . . . .	66
2.3	Hydrodynamic Parameters . . . . .	70
2.4	Conclusion . . . . .	79

### 2.1 NANOPARTICLES CHARACTERIZATION

#### 2.1.1 ZERO CHARGE POINT

THIS study adopted TiO<sub>2</sub> NP in the anatase mineral form. Aqueous suspensions of TiO<sub>2</sub> NP were prepared by diluting commercial anatase dispersion (NanoAmor 7012WJWR, 15 wt%, 5-30 nm) with deionized (DI) water and setting ionic strength (IS) and pH values with KCl and KOH. In agreement with manufacturer's statement, a primary particle size of 5 nm was determined through transmission electron microscopy. The zeta potential ( $\zeta$ ) of the NPs, which, as previously seen in section 1.2, is a parameter that controls the colloidal stability of a suspension, was measured as a function of pH under different IS values (Figure 2.1a). The measure was obtained by means of a Zeta-Sizer Nano ZS (Malvern Instruments Ltd, Malvern, UK), through electrophoretic mobility measurements and using the Smoluchowski approximation, yielding an isoelectric point (IEP) around pH 6. This means that a very acidic or basic solution is necessary to have a stable suspension. Considering that, as reported in the literature, the zeta potential of quartz is around -50 mV at pH 10 (Liang et al. 2013b; Solovitch et al. 2010; Yukselen-Aksoy and Kaya 2011), column experiences were conducted at pH 10. Under very basic pH conditions, NP are negatively charged and the electrostatic repulsion between NP and sand grains



is maximized. Column experiences are therefore conducted under unfavorable attachment conditions.

### 2.1.2 COLLOIDAL STABILITY AND UV-VIS SPECTROSCOPY

The NP hydrodynamic diameter was measured by means of a Malvern ZetaSizer Nano ZS, through Dynamic Light Scattering. The size is expressed in terms of the Z-average, the most stable number produced by the DLS technique, based on cumulants analysis (Tscharnutter 2000). Since the calculation of the Z-average is mathematically stable, the Z-average result is relatively insensitive to experimental noise, and that makes it a preferred DLS size parameter and the accepted norm for presenting particle sizing results by DLS. It is important to note that this mean size is an intensity mean, it is not a mass or number mean because it is calculated from the signal intensity. It gives a good description of the size that is comparable with other methods of analysis for spherical, reasonably narrow monomodal samples. In DLS, the sample dispersion is expressed from the polydispersity index. A sample can be considered reasonably monodisperse for polydispersity values below 0.1.

The stability ratio ( $W$ ) of the  $\text{TiO}_2$  NP suspension was determined measuring the rate of increase in NP size under different KCl and NaCl concentrations (Figure 2.1c, 2.1d). The critical coagulation concentration (CCC), corresponding to the transition from kinetic stability to rapid aggregation, results to be approximately 30 mM for KCl and 300 mM for NaCl (Figure 2.1e). The large difference in CCC between KCl and NaCl, which are both monovalent salts, suggests  $\text{TiO}_2$  having more affinity with  $\text{Na}^+$  than with  $\text{K}^+$ . The  $\text{TiO}_2$  NP suspension prepared for column experiments, with a concentration of 50 mg/L, pH 10 and a KCl concentration of 5 mM, resulted in a Z-average NP size between 70 and 100 nm (Figure 2.1b). The suspension is therefore composed of conglomerates of NP, which have a primary size of 5 nm.

UV-vis absorbance spectra of  $\text{TiO}_2$  NP suspensions at different concentrations were measured over a wavelength ( $\lambda$ ) range of 220-400 nm (Figure 2.1f). The more the concentration is high the more the absorbance is elevated for UV wavelengths. Once verified the linearity between the absorbance value and the NP concentration, a  $\lambda$  of 280 nm was chosen to detect NP concentration at the outlet of the column during column experiments.

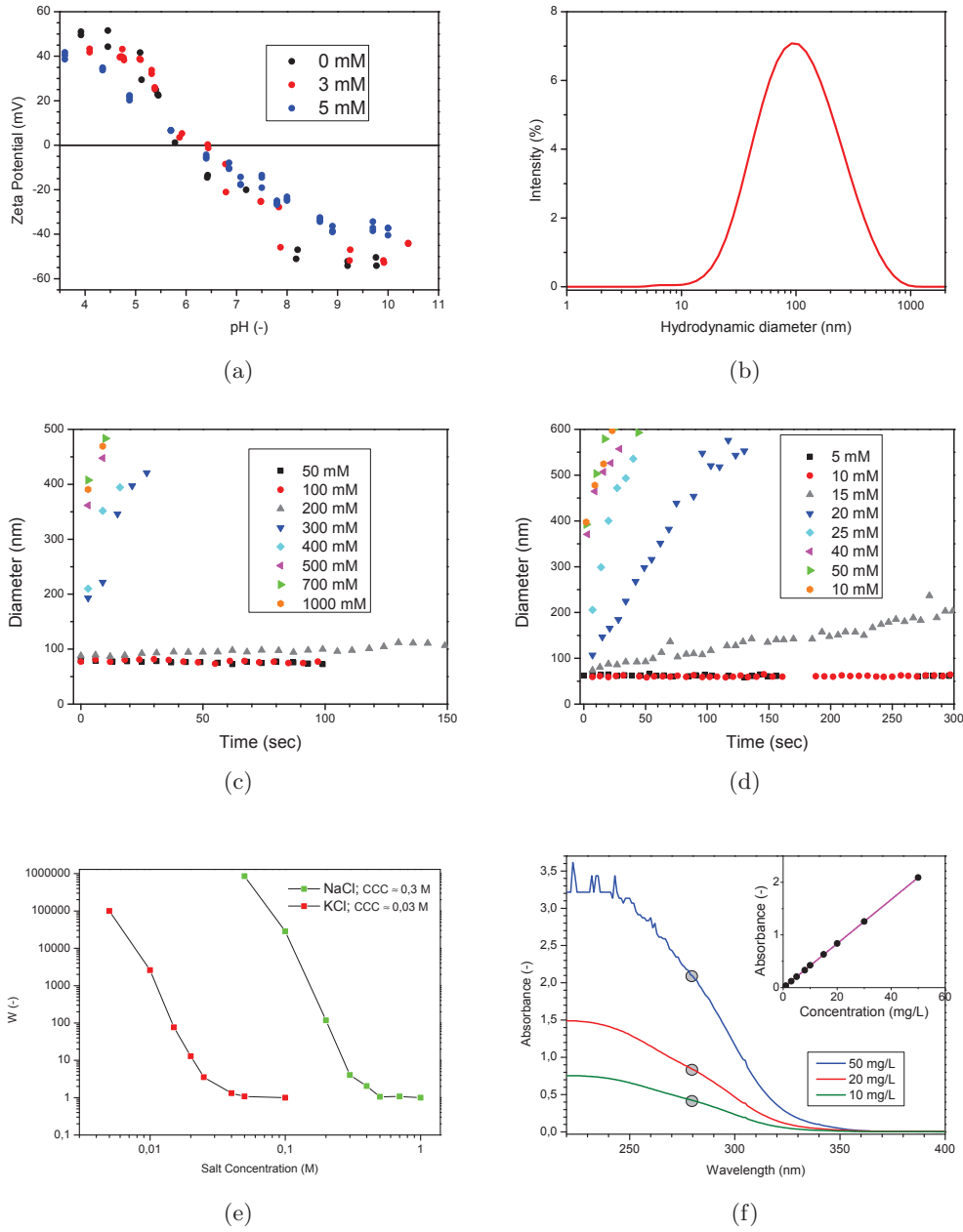


Figure 2.1: a) Zeta potential ( $\zeta$ ) of the NPs suspension measured as a function of pH under different ionic strength values (0 mM, 3 mM, 5 mM KCl). b) Hydrodynamic diameter of NPs suspension at 0 mM. Both images are referred to a 50 mg/L TiO<sub>2</sub> NP suspension. Rate of increase in NP size under different NaCl (c) and KCl (d) concentrations. e) Stability ratio ( $W$ ) under different KCl and NaCl concentrations. f) UV-vis absorbance spectra of TiO<sub>2</sub> NP suspensions at different concentrations and calibration curve at 280 nm. (Toloni et al. 2014).

### 2.1.3 DLVO INTERACTION PROFILES

The classical Derjaguin-Landau-Verwey-Overbeek (DLVO) theory (section 1.2.1) was used to estimate the interaction profiles. The interactions between particles and collectors, between two particles and between particles and the air-water interface (AWI) were taken into account. The first two types of interactions are present in both saturated and unsaturated porous media, while the particle-AWI interaction concerns exclusively unsaturated media, because of the presence of air in the poral space. In order to obtain reliable DLVO profiles,  $\zeta$  potentials and Hamaker constants measurements or estimations are of primary importance.  $\text{TiO}_2$  NP  $\zeta$  potentials at different IS are referred to Figure 2.1a, while, for what concerns quartz sand and AWI, data were obtained from the literature. The  $\zeta$  potential of quartz was assumed to be -50 mV at pH 10 (Liang et al. 2013b; Solovitch et al. 2010; Yukselen-Aksoy and Kaya 2011). The AWI has been reported to be negatively charged too, within a range from -15 mV to -65 mV (Bradford and Torkzaban 2008; Najafi et al. 2007). Calculations are presented for AWI  $\zeta$  potential equal to -15 mV, -50 mV and -65 mV. The Hamaker constants were calculated through Equation 1.9: results are presented in Table 2.1.

The van der Waals interaction is attractive for positive values of  $A_H$ , while is repulsive for negative values. Being water  $A_H$  null, the value of  $A_H$  for  $\text{TiO}_2$ -water-AWI systems is negative, implying that the van der Waals interaction is repulsive for  $\text{TiO}_2$  NP at the AWI. The DLVO profiles in Figure 2.2 show first and secondary minima for the  $\text{TiO}_2$ -water-Sand and  $\text{TiO}_2$ -water- $\text{TiO}_2$  systems, while no minima are expected for the  $\text{TiO}_2$ -water-AWI systems. NP are thus not expected to be retained from the AWI according to the DLVO theory. This is in accordance with the literature (Mitropoulou et al. 2013; Bradford and Torkzaban 2008). In order to better understand NP behavior, it is possible to include in the calculations the hydrophobic repulsion too. Since  $\text{TiO}_2$  NP can be either hydrophobic or hydrophilic depending on their production process and on their surface properties, in Figure 2.2e the results assuming an hydrophobic behavior ( $\theta = 100^\circ$ ) and an hydrophilic behavior ( $\theta = 15^\circ$ ) are compared. Values of  $a = -7.0$  and  $b = -18.0$  were taken from Yoon et al. (1997). It can be observed that the interaction profile for the  $\text{TiO}_2$ -water-AWI systems exhibits a secondary minimum when the  $\text{TiO}_2$  NP are assumed hydrophobic.

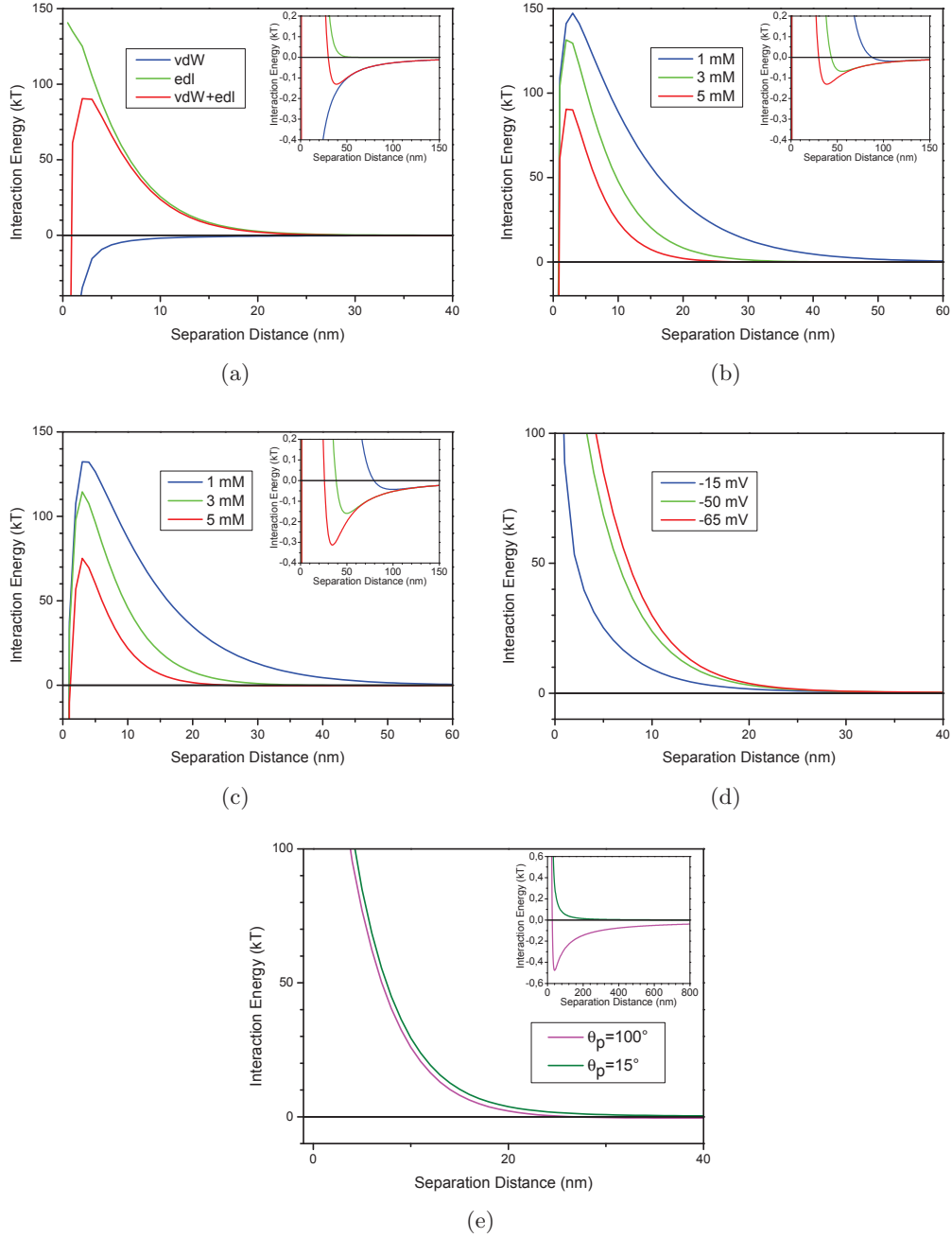


Figure 2.2: a) DLVO interaction profile between NP and collector surface at 5 mM. Contributions from van der Waals and electrical double layer interactions are shown. b) DLVO interaction profiles between NP and collector surface at 5 mM, 3 mM and 1 mM (Toloni et al. 2014). c) DLVO interaction profiles between two NP surfaces at 5 mM, 3 mM and 1 mM. d) DLVO interaction profiles between NP surface and the AWI for AWI  $\zeta$  potential equal to -15 mV, -50 mV and -65 mV at 5 mM. e) DLVO interaction profiles between NP surface and the AWI for AWI  $\zeta$  potential equal to -50 mV and assuming an hydrophobic behavior ( $\theta = 100^\circ$ ) or an hydrophilic behavior ( $\theta = 15^\circ$ ).

	$A_H$ ( $10^{-20}$ J)	$\zeta$ potential (mV)
TiO <sub>2</sub>	15 <sup>(a)</sup>	-40/-50 <sup>(d)</sup>
Quartz sand	8.5 <sup>(a)</sup>	-50
Water	3.7 <sup>(b)</sup>	-
Air	0 <sup>(b)</sup>	-
AWI	-	-15/-50/-65 <sup>(c)</sup>
TiO <sub>2</sub> -Water-Sand	1.93	-
TiO <sub>2</sub> -Water-TiO <sub>2</sub>	3.8	-
TiO <sub>2</sub> -Water-AWI	-3.5	-

Table 2.1: List of the parameters employed in the DLVO calculations.

<sup>(a)</sup>Bergstrom (1997). <sup>(b)</sup>Israelachvili (1985). <sup>(c)</sup>Bradford and Torkzaban (2008).

<sup>(d)</sup>-40 mV is referred to 5 mM and pH 10, -50 mV is referred to 1/3 mM and pH 10.

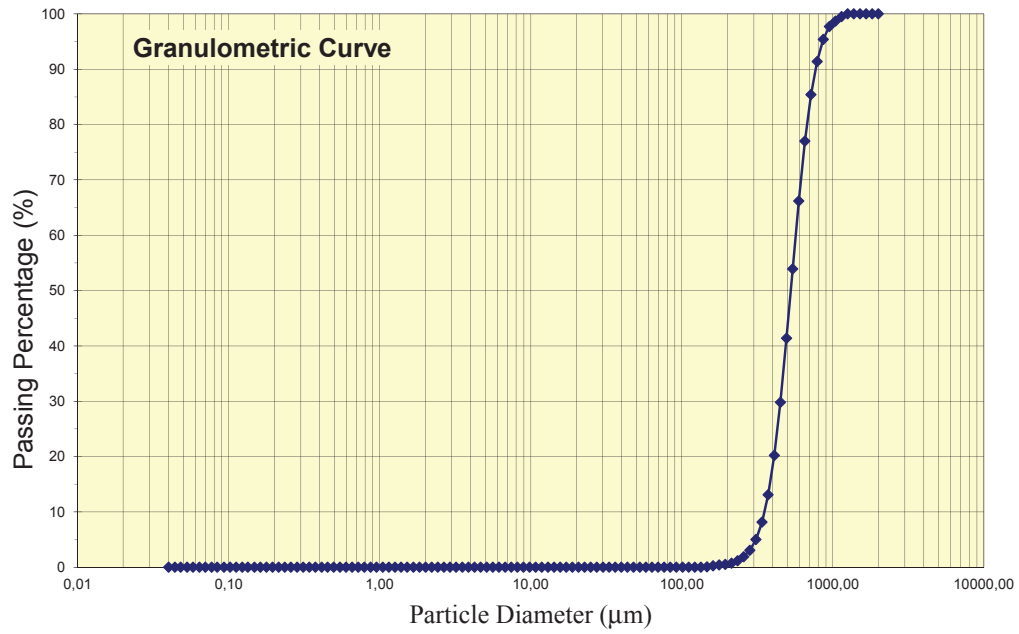
## 2.2 SAND CHARACTERIZATION

### 2.2.1 COMPOSITION AND GRANULOMETRY

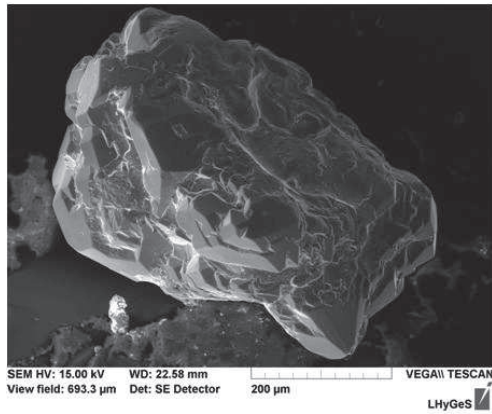
The porous medium was composed of quartz sand K30 from Kaltenhouse, France. It consists mainly of quartz (silicate, 96.69%) with traces of orthoclase (feldspar, 2.89%) and variscite (phosphate, 0.42%). The granulometric curve (Figure 2.3) shows an average grain diameter ( $d_{50}$ ) of 490  $\mu\text{m}$  and a coefficient of uniformity ( $C_u = d_{60}/d_{10}$ ) of 1.595. The surface of the grains is not uniform and scanning electron microscope images (SEM) (Figure 2.3) reveal that the feldspar grains are much rougher than those of quartz. Since a rough surface enhances colloid deposition, feldspar can increase significantly the number of attachment sites for NP (Darbha et al. 2012).

### 2.2.2 SAND CLEANING PROTOCOL

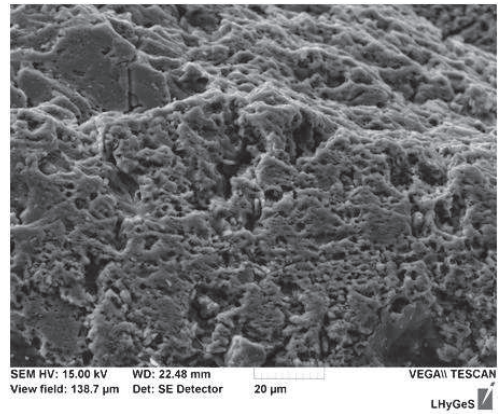
To remove metal oxides, impurities and natural colloidal particles, the sand was cleaned through three cycles of washings with a 0.5 M HCl, a 0.5 M KOH and DI water, then oven-dried at 60 °C. Each washing lasted 15 minutes: during this time an amount of about 400 g of sand was covered in solution and sonicated. Between each step of the cleaning protocol the sand was flushed with DI water in a 200  $\mu\text{m}$  sieve. During the first two basic washings, the solution turned to brown/red, presumably due to the large amount of dissolved metal oxides. ICP-MS analysis of solutions sampled after each step of the cleaning protocol showed that the cycles result in a gradual decrease of the dissolved concentration of Iron,



(a)



(b)



(c)

Figure 2.3: (a) Grain size distribution of the quartz sand K30 from Kaltenhouse, France. SEM images of a grain of quartz (b) and orthoclase (c)

	Solution	Al	Mg	Ca	Fe	Ti	P
1	HCl	2.05	0.046	0.84	1.25	0.022	0.06
2	KOH	1.45	0.013	0.03	0.33	0.017	0.13
3	DI	0.82	0.038	0.0	0.24	0.058	0.03
4	HCl	0.43	0.017	0.18	0.88	0.014	0.0
5	KOH	0.27	0.0	0.03	0.13	0.009	0.03
6	DI	0.32	0.019	0.0	0.14	0.020	0.0
7	HCl	0.23	0.015	0.16	0.38	0.007	0.0
8	KOH	0.17	0.007	0.03	0.05	0.008	0.02
9	DI	0.23	0.013	0.0	0.11	0.014	0.0
10	DI	0.04	0.005	0.0	0.01	0.004	0.0

Table 2.2: Dissolved concentrations (mg/L) of phosphorus (P), iron (Fe), magnesium (Mg), titanium (Ti), calcium (Ca) and aluminum (Al) measured through ICP-MS on the used solutions after each step of the sand cleaning protocol.

Aluminum and Titanium (Table 2.2, Figure 2.4).

The elimination of metal oxides and colloidal particles is important, especially in the absence of coatings or organic matter, in order to minimize the number of attachment sites in the porous medium. Moreover, the sieving removes the colloidal fraction of the sand, which could facilitate the transport of the NP.

In the literature a similar protocol can be found in Solovitch et al. (2010), but the cycle was repeated ten times. Others adopted more aggressive protocols, which include soaking the sand in 12 M HCl and baking it at 800 °C or boiling the sand in HNO<sub>3</sub> (Redman et al. 2004; Lenhart and Sayers 2002). Nevertheless, taking into account the analysis in Figure 2.4, the adopted protocol was judged sufficient to ensure the sand quality.

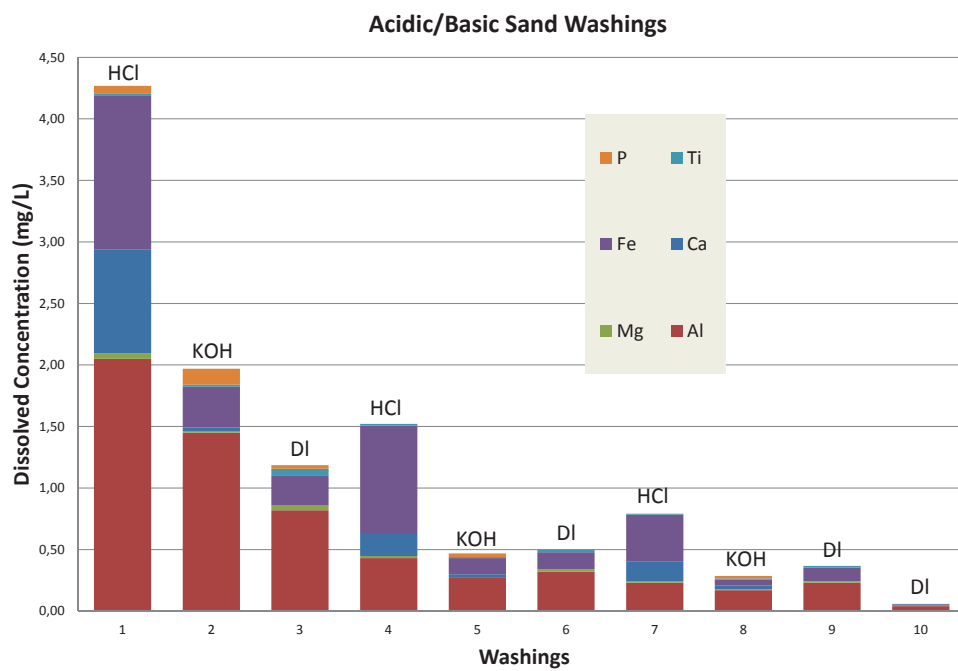


Figure 2.4: Dissolved concentrations of phosphorus (P), iron (Fe), magnesium (Mg), titanium (Ti), calcium (Ca) and aluminum (Al) measured through ICP-MS on the used solutions after each step of the sand cleaning protocol.



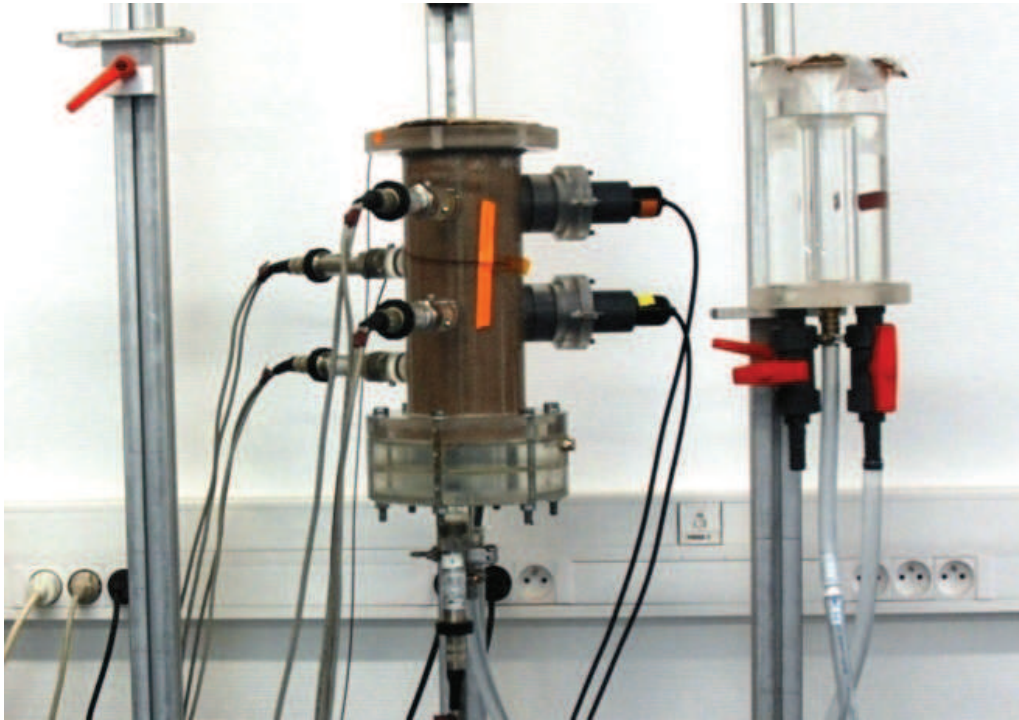
## 2.3 HYDRODYNAMIC PARAMETERS

### 2.3.1 MATERIALS

The estimation of the van Genuchten soil hydrodynamic parameters is necessary to solve the Richards Equation. In the relationship between pressure head ( $h$ ) and water content ( $\theta$ ) expressed by the hydrodynamic parameters, different  $\theta$  values can be found for the same  $h$  value, depending upon the history of soil wetting and drying. In order to better understand the processes of drainage and imbibition, the hysteresis curve (presented in Section 2.7) was reconstructed.

A plexiglass column (10 cm in diameter and 28 cm in length) was employed for drainage and imbibition experiments. The bottom of the column was linked by a plastic tube to a water reservoir, vertically mobile, allowing to control the water saturation level (Figure 2.5a). Sensors were placed along the column, to monitor water content, pressure head and temperature. The necessity of accommodating the sensors justifies the relatively large column diameter. Water content was measured by the medium impedance sensors ThetaProbes ML2x (Delta-T Devices Ltd, Cambridge, UK). Two impedance sensors were installed 7 cm and 17 cm below the sand surface. Each ThetaProbe consists of a waterproof housing which contains the electronics and four sharp stainless steel rods that are inserted into the sand (Figure 2.5b). A 100MHz sinusoidal signal is applied at the array of rods and is reflected from the soil in function of its impedance. These reflections combine with the applied signal to form a voltage standing wave along the transmission line. The output voltage is proportional to the difference in amplitude of this standing wave at two points, and this gives a sensitive and precise measure of soil water content, after the calibration that is described in section 2.3.2.

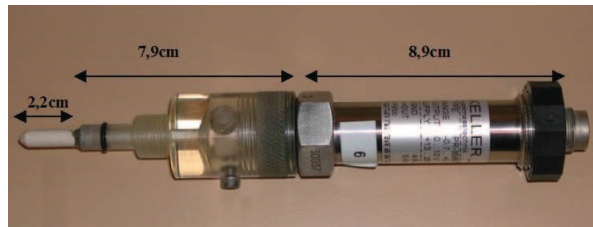
The pressure head was measured by five tensiometers, installed 7 cm, 12 cm, 17 cm, 22 cm, and 28 cm below the sand surface. Each tensiometer is composed of a porous ceramic cup inserted into the soil column, of a plexiglass cylinder and of a pressure transmitter (Figure 2.5c). The plexiglass cylinder was filled with water, in contact with the water in the porous medium via the porous ceramic cup. The pressure head of the water in the cylinder, measured by the pressure transducer, is supposed to attain the equilibrium with the pressure head of the water in the porous medium. The pressure transmitter, a 35 X (Keller AG, Winterthur, Switzerland), with an accuracy of 2 cm, requires a negligible transfer of water to record the suction in the column, thus minimizing the disturbance of the flow. The sensor signal was directly converted into water column height by the pressure transmitter before being sent to the PC for data acquisition. Each sensor was set to zero at the atmospheric pressure before the experiences.



(a)



(b)



(c)

Figure 2.5: Experimental set up for the estimation of the van Genuchten soil hydrodynamic parameters. Two medium impedance probes (right side) and five tensiometers (left side and bottom) were installed in the sand packed column. The reservoir, which control the water content, in the picture is in the higher position, which corresponds to a completely saturated condition. Water content captor (b) and pressure head captor (c)

### 2.3.2 CALIBRATION OF THE WATER CONTENT SENSORS

In order to obtain the best estimate of water content, sensors were characterized and the parameters of conversion from output tension to water content were identified. Ten samples with different moisture contents, prepared with a known amount of water and sand, were used for the calibration. Then, data of each captor were fitted by three different functions.

The sensor manufacturer provided two possible functions, based on two relationships between the ThetaProbe output tension ( $U$ ) and the square root of the dielectric constant of the porous medium ( $\sqrt{\varepsilon_r}$ ): either a linear relationship:

$$\sqrt{\varepsilon_r} = 1.1 + 4.44U \quad (2.1)$$

or a polynomial one:

$$\sqrt{\varepsilon_r} = 1.07 + 6.4U - 6.4U^2 + 4.7U^3 \quad (2.2)$$

It has been shown (Topp et al. 1980) that a simple linear relationship between the complex refractive index (which is equivalent to  $\sqrt{\varepsilon_r}$ ) and water content, of the form:

$$\sqrt{\varepsilon_r} = c_0 + c_1 \cdot \theta \quad (2.3)$$

is a good approximation for several soil types. Relation (2.3) with (2.1) and (2.2) allows to obtain the equations:

$$\theta = \frac{(1.1 + 4.44U) - c_0}{c_1} \quad (2.4)$$

$$\theta = \frac{(1.07 + 6.4U - 6.4U^2 + 4.7U^3) - c_0}{c_1} \quad (2.5)$$

Since the water content depends on the square root of the dielectric constant, another relation was tested in this experiment:

$$\theta = \sqrt{\frac{U - c_0}{c_1}} \quad (2.6)$$

The evaluation by least-squares regression of the parameters of (2.3), (2.4) and (2.6) (Tables 2.3 and 2.4) resulted in the best fit of the square root model (2.6) (Figure 2.6).

### 2.3.3 EXPERIENCES

The column was wet-packed as uniformly as possible with cleaned sand: 1 cm of sand was added at a time, gently tapping the column from time to time and

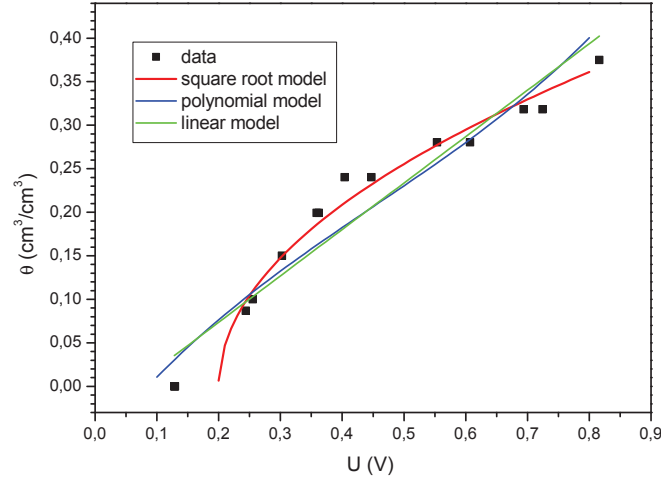


Figure 2.6: Linear, polynomial and square root fit of the water content values. The square root relation results to be better than the relations provided by the manufacturer.

	$c_0$	$c_1$	$R^2$
Linear model	$1.4 \pm 0.1$	$8.3 \pm 0.6$	0.930
Polynomial model	$1.6 \pm 0.1$	$7.3 \pm 0.5$	0.937
Square root model	$0.19 \pm 0.02$	$4.8 \pm 0.4$	0.962

Table 2.3: Different calibrations for sensor 2.

maintaining the water level 1 cm over the sand level throughout the process. A correct and uniform sand packing is important for water content sensors and tensiometers to work properly, since a very good contact with the sand grains is required.

In the sand packed column, the water level is controlled by the position of the water reservoir. Once the column filled, the reservoir position met with the top of the column. If, from this position, the reservoir is lowered, the water level is consequently lowered, inducing a decrease in  $\theta$ . The reservoir was then moved down by steps and then moved in the same manner up with different drying and wetting cycles. Before each movement of the reservoir it was necessary to wait for the equilibrium to be achieved. The more the position of the reservoir was low, the longer it took to achieve stable values for water content and pressure head: a complete drainage and imbibition cycle required 12 hours. Three cycles were realized: two cycles of drainage and imbibition conducted step by step from

	$c_0$	$c_1$
Sensor 1	$0.199 \pm 0.009$	$4.6 \pm 0.2$
Sensor 2	$0.19 \pm 0.02$	$4.8 \pm 0.4$

Table 2.4: Optimized moisture sensor parameters.

$\theta$ (-)	Water mass (g)
0.0000	0.00
0.0868	139.45
0.0999	160.43
0.1500	240.84
0.1993	320.17
0.2403	386.00
0.2802	450.00
0.3182	511.00
0.3748	602.00

Table 2.5: List of the nine values of moisture content used for calibration. Each water mass was mixed with a 2700 g sand mass.

28 cm until -10 cm, one cycle conducted from 28 cm until -20 cm in a single step.

The presence of an hysteretic behavior can be observed in the water content data of the first drainage (Figure 2.7), since the final water content value is lower than the starting value (8% difference). The hysteresis curve was then obtained representing the water content values at the equilibrium in function of the pressure head values, for each position of the reservoir. All the data are referred to the -7 cm probe, except for the third cycle (Figure 2.7c). In fact the smallest  $\theta_r$  value (0.11) is achieved in the single step drainage, the only that permitted to modify the water content at -17 cm. The real  $\theta_r$  value would require the total drainage of the column, difficult to be realized in the laboratory. The van Genuchten model parameters were optimized for each drying and wetting cycle (Table 2.6). In Figure 2.7c the black lines describe a deep drainage, while the red lines represent an incomplete process, attaining a larger  $\theta_r$  value. It should be noted that, despite the hysteretic behavior is often neglected, the water content values are strongly dependent on the history of the porous medium (up to a 30% difference).

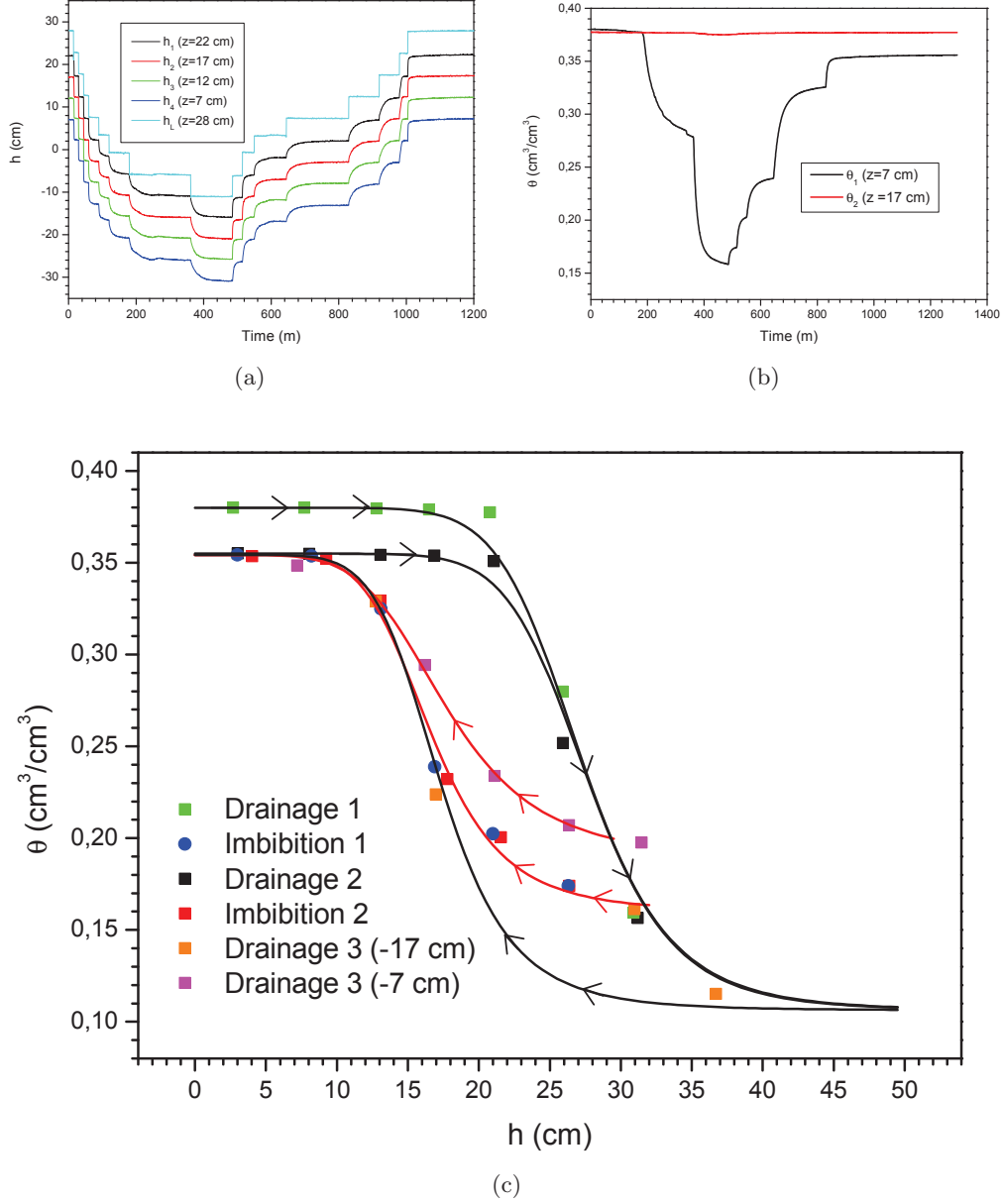


Figure 2.7: Pressure head (a) and water content (b) values at -7 cm during the first drying and wetting cycle. The presence of an hysteretic behavior can be observed, since the final water content value is lower than the starting value. c) Hysteresis curve, with the data of the three cycles. Data referred to the -7 probe except where otherwise specified. The black lines describe a deep drainage, while the red lines represent a process attaining a larger  $\theta_r$  value.

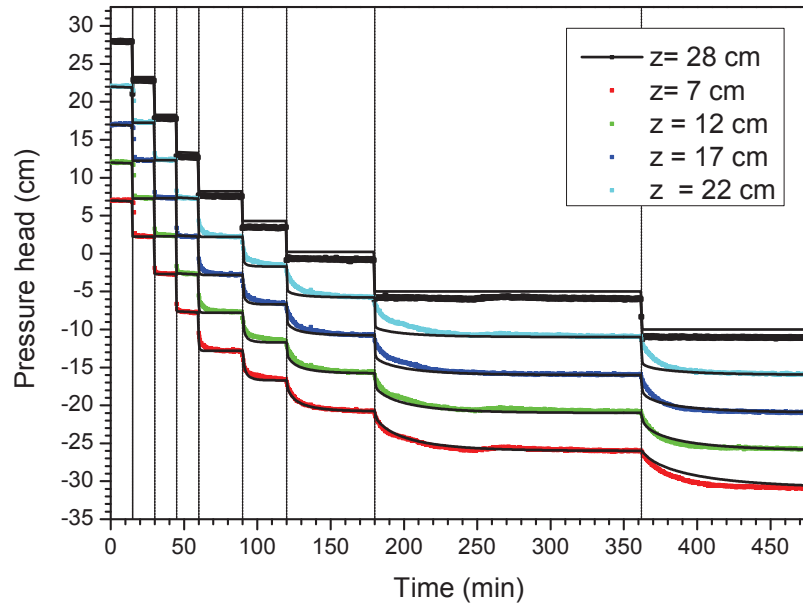
### 2.3.4 UNSATURATED HYDRAULIC SOIL PARAMETERS ESTIMATION

The van Genuchten model parameters ( $\alpha$ ,  $\theta_r$ ,  $\theta_s$ ,  $n$ ,  $l$ ,  $K_s$ ) were estimated from observed sand water content data and pressure head data. The inverse problem was solved through the Levenberg-Marquardt optimization algorithm (Section 1.4.1) for the first drainage (Figure 2.8).

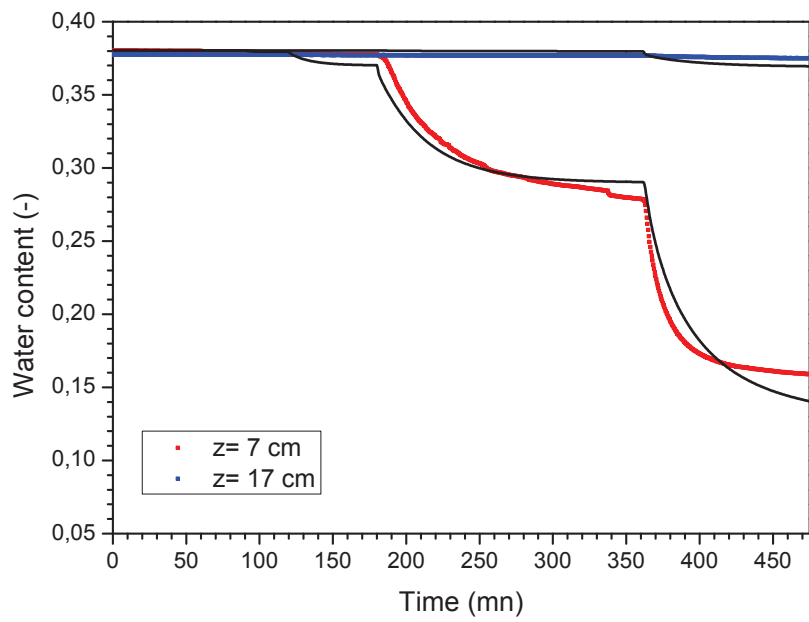
The 28 cm deep profile of the column was discretized into equidistant 281 nodes. At the top of the column a zero flow boundary condition was applied, while the pressure head measures of the tensiometer installed 28 cm below the sand surface were taken as lower boundary conditions. An hydrostatic profile was taken as initial condition.

In order to reduce the dimensionality of the problem, considering that the van Genuchten parameters are correlated, the value of the pore connectivity parameter  $l$  was set to 0.5 and the residual water content  $\theta_r$  was set to zero. The chosen  $l$  value is often adopted in the literature (Abbaspour et al. 2001, Wollschlaeger et al. 2009). The residual water content is a parameter that is very difficult to measure directly, because measurements at very low saturation values are time consuming in order to ensure equilibrium. In the literature values between zero and 0.05 can be found. For simplicity, and because it gave a small objective function,  $\theta_r$  was fixed to zero.

In the evaluation, two sets of initial parameter values were tested. The first set was composed of the parameters obtained for the hysteresis curve ( $\alpha$ ,  $\theta_r$ ,  $\theta_s$ ,  $n$ ,  $l$ ), specifically the parameters of the first drainage, and of a  $K_s$  value experimentally determined by a constant head permeameter. The second set was obtained through the ROSETTA pedotransfer function (Schaap et al. 2001) with the model SSC for a porous medium composed of 100% sand. The solution of the inverse problem (Table 2.6), which resulted to be the same for the two sets of initial parameters, corresponds to an objective function for the pressure head data of 0.01344 and for the water content data of 0.01366. The  $R^2$  has a value of 0.997799 and a correlation matrix as in Table 2.7.



(c)



(d)

Figure 2.8: Solution of the inverse problem.



	$\theta_r$ (-)	$\theta_s$ (-)	$\alpha$ (cm <sup>-1</sup> )	$K_s$ (cm/s)	$n$ (-)	$l$ (-)
Hyst - Drain	0.1	0.379	0.037	-	9	0.5
Hyst - Drain	0.1	0.354	0.0366	-	10	0.5
Hyst - Imb	0.1	0.354	0.0595	-	7.3	0.5
Hyst - Imb 3 (-17 cm)	0.167	0.354	0.0628	-	7.4	0.5
Hyst - Imb 3 (-7 cm)	0.188	0.354	0.0059	-	5.7	0.5
Permeameter test	-	-	-	0.074	-	-
ROSETTA	0	0.38	0.04	0.016	2	0.5
Optimized parameters	0	0.38	0.0366	0.23	12.24	0.5
Error	-	$\pm 0.0003$	$\pm 0.00006$	$\pm 0.0003$	$\pm 0.05$	-

Table 2.6: Optimized sand hydrodynamic parameters with errors, starting points of the inverse problem and parameters of the hysteresis curves.

	$K_s$	$\theta_s$	$\alpha$	$n$
$K_s$	1.0000	0.1524	-0.4067	-0.0931
$\theta_s$	0.1524	1.0000	0.3024	-0.3940
$\alpha$	-0.4067	0.3024	1.0000	-0.0888
$n$	-0.0931	-0.3940	-0.0888	1.0000

Table 2.7: Correlation matrix for the van Genuchten optimized parameters.

## 2.4 CONCLUSION

The  $\text{TiO}_2$  NP solution was characterized and its colloidal stability was studied. Through the DLVO theory, the homo and hetero aggregation of the NP were estimated. A sand cleaning protocol was developed to remove metal oxides, impurities and natural colloid particles. The porous media was characterized ( $\theta$ ,  $\alpha_L$ , Mualem-van Genuchten model parameters) through non-reactive tracer transport experiments and drainage experiments.



## CHAPTER 3

---

# TRANSPORT OF NANOPARTICLES IN A SATURATED POROUS MEDIUM

---

### CONTENTS

3.1	Materials and Methods . . . . .	81
3.2	Modeling . . . . .	89
3.3	Conclusion . . . . .	93

---

## 3.1 MATERIALS AND METHODS

### 3.1.1 COLUMN SYSTEM

A PLEXIGLAS flow cell from Soil Measurement Systems, Tucson USA (3.75 cm in diameter and 15.2 cm in length) was wet-packed as uniformly as possible with cleaned sand (Section 2.2.2). The flow cell consists of a tube, which holds the porous medium, and two removable end-plate assemblies, one mounted on each end of the tube (Figure 3.1). The tube and the top and bottom end-plate assemblies are held together with 3 rods. Each end-plate assembly consists of two parts: a round doughnut shaped part containing an o-ring slides over the end of the column, and a flat round plate which holds a perforated aluminum support disc. There is a flat o-ring between the two plates.

The water velocity was ensured by the peristaltic pump Masterflex Easy Load 3 (Cole-Palmer, Vernon Hills, USA) with L/S 13 or L/S 14 pump tubing and verified by a digital balance. Water flux was imposed from the bottom to the top of the column, to avoid air trapping. At the bottom of the column a 2 cm layer of 2 mm glass beads held the porous medium in place. The protocol exposed in Section 3.1.2 was adopted to prepare the columns for the saturated experiments. As regards conductivity, pH and ultraviolet absorption, values were measured automatically, every 5 s, throughout the experiments for both inlet and outlet

flows by means of on-line sensors. All the flow cells and electrodes were connected to a Monitor UPC-900 and a Monitor pH/C-900 (GE Healthcare Bio-Sciences AB, Uppsala, Sweden). In order to ensure a constant water flow and prevent any tube deformation, the peristaltic pump tube was replaced before each experiment.

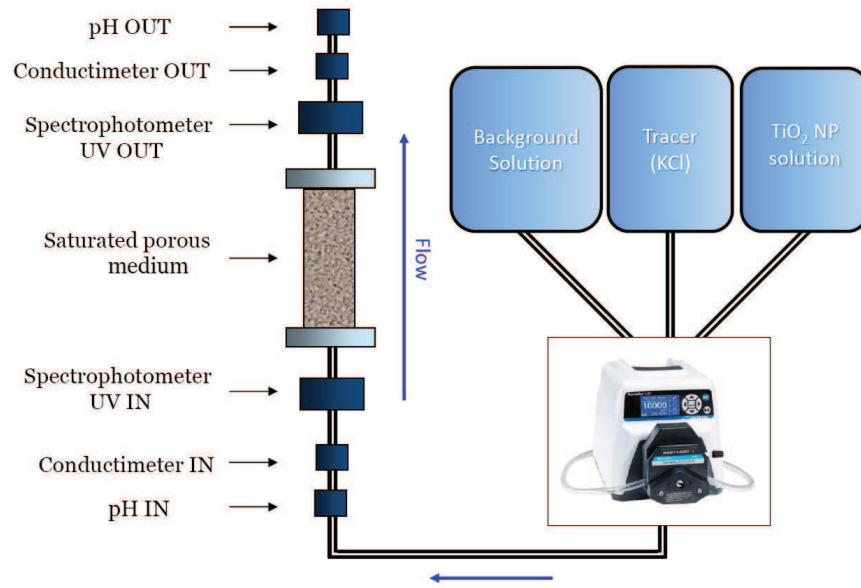
### 3.1.2 EXPERIMENTAL PROTOCOL FOR PREPARATION OF THE SATURATED POROUS MEDIA

- Water flux was imposed from the bottom to the top of the column. A 8 $\mu$ m paper filter (GE Healthcare Bio-Sciences AB, Uppsala, Sweden) was placed at the bottom of the column, on a regular end-plate, in order to hold the sand in place;
- The column was wet-packed as uniformly as possible with cleaned sand (Section 2.2.2), adding 1 cm of sand at a time, gently tapping the column from time to time and maintaining the water level 1 cm over the sand level throughout the process;
- The last 2 cm of the column were packed with 2 mm glass beads, cleaned with the same protocol used for the sand. A regular top was put in place;
- The column was turned upside down and, once sealed the outlet of the column with a clamp, the top end-plate of the column, previously at the bottom, was temporarily demounted and the paper filter removed;
- The clamp was removed, the direction of the water flow of the peristaltic pump was inverted and the porous medium was equilibrated at the desired IS and pH 10 with approximately 20 pore volumes (PV) of electrolyte solution;
- The water flow planned for the experiment was applied;
- A saturated porous media was obtained, with a flux from the bottom to the top of the column. A 2 cm layer of glass beads held the porous media in place.

### 3.1.3 EXPERIMENTAL PROTOCOL FOR PREPARATION OF TiO<sub>2</sub> NANOPARTICLE SUSPENSION

Before each experiment, 0.5 L of 50 mg/L TiO<sub>2</sub> fresh suspension was prepared in a graduated glass flask:

- 0.5 L of DI water was adjusted to the desired IS using KCl, and then the flask was placed on a magnetic stirrer;



(a)



(b)



(c)

Figure 3.1: (a) Experimental set up for the saturated experiments. (b) Flow cell elements. (c) Sand packed flow cell ready for a NP transport experiment. At the bottom a layer of glass beads is visible.

- 4 mL of 2 g/L KOH solution was added;
- 167  $\mu\text{L}$  of the stock 15 wt% NanoAmor suspension was added;
- The pH of the solution was checked (it should be around pH 10.2), as well as the UV absorbance at  $\lambda = 280 \text{ nm}$ ;
- The solution was finally injected in the column system.

#### 3.1.4 EXPERIMENTAL PROTOCOL FOR NANOPARTICLE TRANSPORT UNDER SATURATED CONDITIONS

- Before each NP injection, the column was wet-packed and equilibrated as in Section 3.1.2. It was checked whether pH and conductivity remain approximately constant between inlet and outlet of the column;
- A tracer injection of 3 PV (1 g/L KCl) was effectuated to control the repeatability of the hydrodynamic parameters (porosity  $\phi = 0.390 \pm 0.005$ ; longitudinal dispersivity  $\alpha_L = 0.069 \pm 0.006 \text{ cm}$ ).
- Each experiment resulted in a 3 PV injection of the 50 mg/L  $\text{TiO}_2$  NP suspension, at pH 10. Experiments were conducted with an IS of 3 and 5 mM and with three average water pore velocities ( $0.002 - 0.012 - 0.07 \text{ cm/s}$ ). The NP suspension was stirred throughout the experiments. To exclude the possibility that measurements were distorted due to NP fixed inside the sensors, outlet flow was sampled through a fraction collector and analyzed by a bench top spectrophotometer if necessary;
- The electrolyte solution was injected until a complete breakthrough curve (BTC) was attained (approximately 2 additional PV);
- The tracer experiment was repeated to check whether hydrodynamic parameters were affected by NP deposition.

All column experiments were conducted, in duplicate or additional replicates, at a room temperature of  $22^\circ\text{C}$ . Due to the huge reactivity of the  $\text{TiO}_2$  NP and to their sensitivity to any small difference in the experimental conditions, many experiments were needed to achieve a good repeatability of the BTC under the different conditions. It has been necessary to eliminate the paper filter that sustained the sand at the bottom of the column, since it was noticed that it disturbed the BTC, and to check that the quality of the DI water was constant.

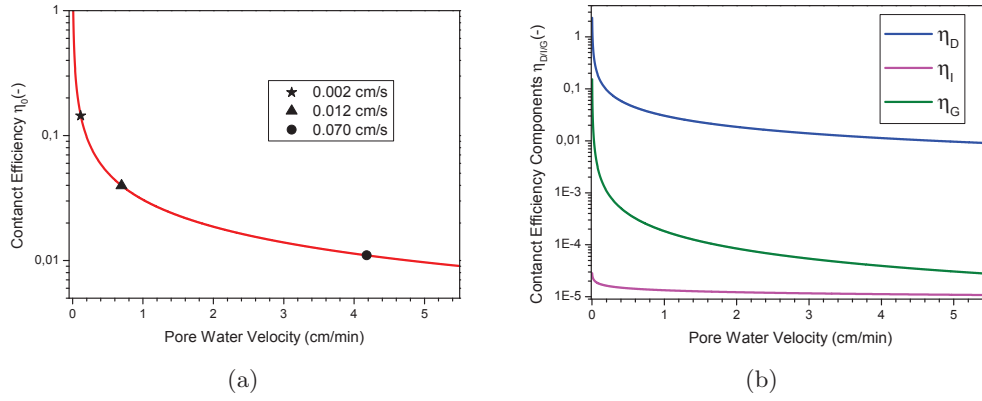


Figure 3.2: a) Single collector efficiency in function of the pore water velocity. Symbols correspond to the adopted velocities. b) Single collector efficiency contributions related to diffusion (D), interception (I) and sedimentation (G).

### 3.1.1.5 SINGLE COLLECTOR EFFICIENCY

The fraction of NP that collide with sand grains, the single collector efficiency  $\eta_0$ , was calculated through the model of Tufenkji and Elimelech (2004), described in Section 1.2.3.2:

$$\eta_0 = \eta_D + \eta_I + \eta_G \quad (3.1)$$

$$\eta_D = 2.4 A_S^{1/3} N_R^{-0.081} N_{Pe}^{-0.0715} N_{vdw}^{0.052} \quad (3.2)$$

$$\eta_I = 0.55 A_S N_R^{1.675} N_A^{-0.125} \quad (3.3)$$

$$\eta_G = 0.22 N_R^{-0.24} N_G^{1.11} N_{vdw}^{0.053} \quad (3.4)$$

Plotting  $\eta_0$  in function of the pore water velocity, we obtain the graphic in Figure 3.2a. The TiO<sub>2</sub> NP single collector efficiency is strongly dependent on water velocity: it decreases when the water velocity increases. Since it represents the probability of contact between a particle and a collector, the larger is the water flow that transport the particle, the harder is for a particle to leave the streamline and enter in contact with a collector. In Figure 3.2b it is evident that, for small size particles, such as NP,  $\eta_0$  is mainly determined from molecular diffusion ( $\eta_D$ ), while interception ( $\eta_I$ ) is dominant for larger particles.



### 3.1.6 BREAKTHROUGH CURVES

Column experiments were performed under two IS and three pore water velocities. Transport of  $\text{TiO}_2$  NP at 3mM KCl results in a weak retention under the smaller water velocity (Figure 3.3a). Instead, under 5 mM KCl, the BTCs show a strong retention that increases when water velocity decreases (Figure 3.3b). This decrease in the NP mass retained by the porous media when water velocity increases is supported by the classical filtration theory (Zamani and Mainibrownian 2009; Yao et al. 1971). The shapes of the elution curves are typical of blocking behavior, associated with a decrease of NP retention in time (Chen et al. 2012). This retention mechanism, resulting in an increase of NP concentration over time in the elution, consists in the progressive saturation of the attachment sites. In Figure 3.3b it can be observed that the BTC at 0.002 cm/s presents an earlier exit time, if compared to the other BTC. Furthermore it is the only BTC that is not monotonic: the presence of two peaks was previously observed in the literature, but still not explained (Liang et al. 2013b).

The occurrence of retention, despite the unfavorable attachment conditions, could be explained by secondary energy minima (Section 1.2.1.3) and by roughness and inhomogeneity of the sand surface. Recent studies, discussed in Section 1.2.3.1, emphasized that the presence of roughness can modify the torque balance, increasing the adhesive torque that the NPs experience and decreasing the hydrodynamic drag (Shen et al. 2014; Bradford et al. 2013). Furthermore, straining can be excluded because the ratio of NP to average grain size (0.0004) is significantly smaller than the 0.005 guideline available in the literature (Bradford et al. 2006).

### 3.1.7 CHALLENGES RELATED TO SATURATED EXPERIMENTS

The repeatability of NP transport experiments under saturated conditions was achieved through a long work. The data used in this study required 74 saturated column experiments to be conducted. Usually in the literature, the repeatability of NP experiments is not matter of discussion or research. Nevertheless, since it has been very difficult to achieve experimental repeatability all along this study, in this section all the faced problems related to reproducibility are analyzed.

**Sand Cleaning Protocol.** In a first time, the sand was only sieved and cleaned through DI water cycles, in order to remove from the sand its natural colloidal fraction. It was soon realized that the total amount of the injected NP was retained under every condition, probably retained from the traces of metal oxides revealed from sand analysis (Section 2.2.1). Different types of sand treatments were tested before finding the adopted protocol (Section 2.2.2). A similar protocol can be found in Solovitch et al. (2010), but the

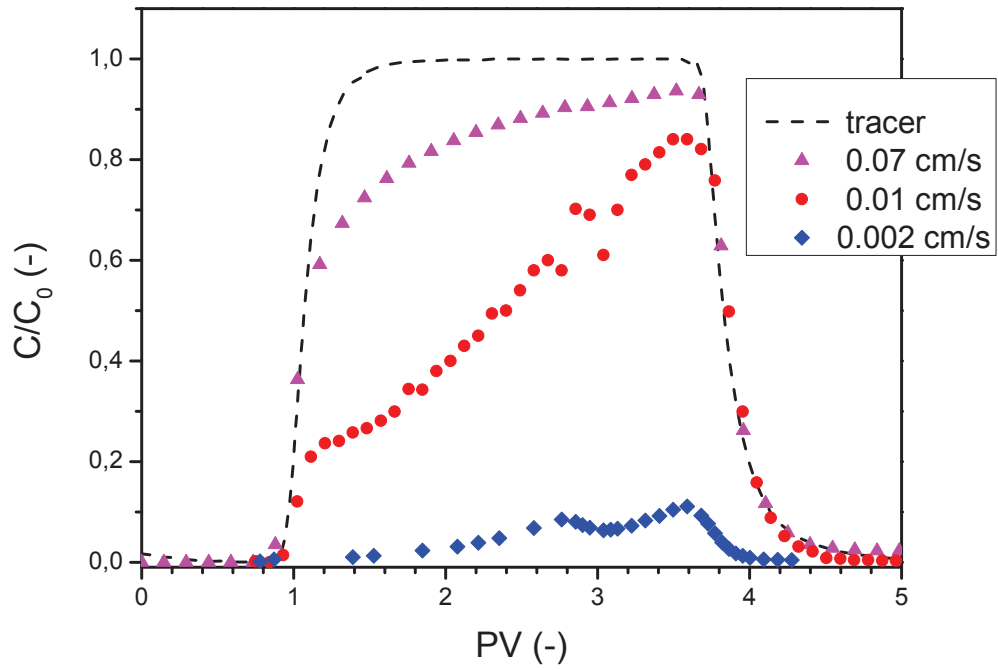
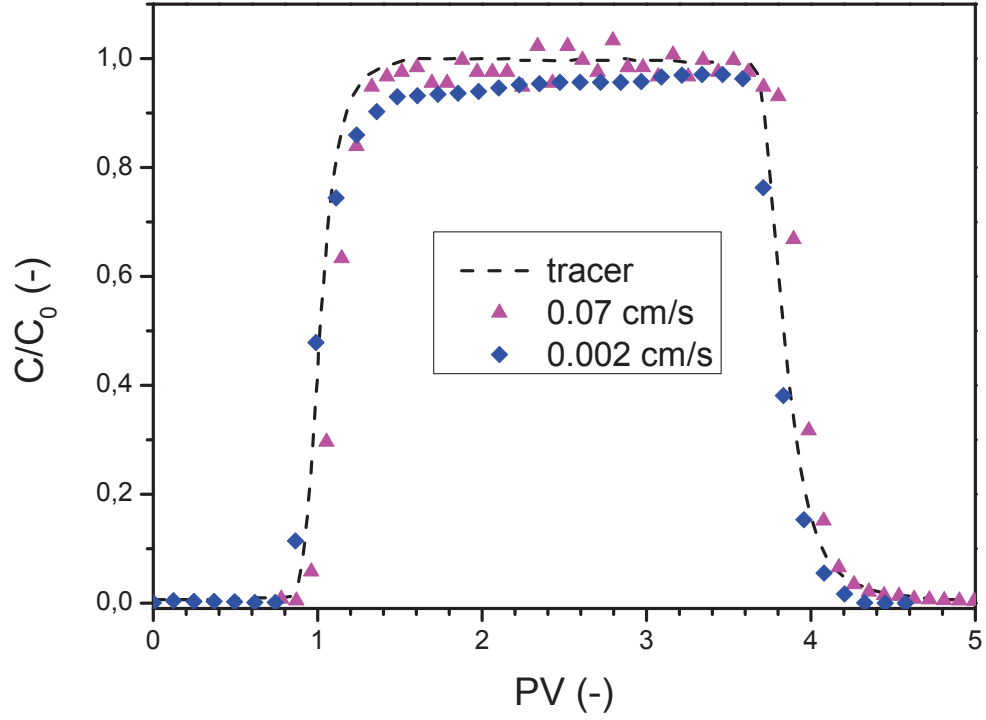


Figure 3.3: Breakthrough curves for 3 mM (a) and 5 mM (b) experiments under different water velocities. The outlet NP concentration is normalised by the inlet concentration. Each BTC is the result of a single experiment and it is not the average of the replicas.

cycle was repeated ten times. Many different protocols are reported in the literature, some of them presenting acidic washings, others presenting acidic and basic washings (Li et al. 2011; Solovitch et al. 2010). Others adopt more aggressive protocols, which include soaking the sand in 12 M HCl and baking it at 800 °C, in order to remove the organic impurities, or boiling the sand in HNO<sub>3</sub> (Redman et al. 2004; Lenhart and Saiers 2002). After several tests, the acidic and basic washings were adopted, with a number of cycles determined through the analysis of the amount of dissolved oxides, as shown in Section 2.2.2.

**Bottom Membrane.** Often in column transport experiments conducted with NP, colloids or virus reported in the literature, the column system presents a membrane at the bottom of the column in order to hold the porous medium in place. It can be a paper filter, a Teflon membrane (Chen et al. 2010) but more often it is a nylon membrane (Wang et al. 2008). In the unsaturated experiments where a vacuum pump is used, a fiber filter (Liang et al. 2013a) or a nylon membrane is normally used as capillary barrier (Knappenberger et al. 2014; Zhuang et al. 2009; Torkzaban et al. 2008). The nylon membrane was reported from Chen et al. (2008) to tend to filter NP, while Torkzaban et al. (2008) stated that it does not filter colloids. Often the bottom membrane is not well documented in experiments description. Sometimes it is not specified, but the presence of a porous plate can be deduced from the pictures (Lanphere et al. 2013).

In this study, the presence of the bottom membrane was identified as responsible for the non reproducibility of many experiments. Several types of filter were tested: 8µm paper filter (ashless, GE Healthcare Whatman), cellulose filters and nylon membranes (20µm, Millipore, Billerica, Massachusetts, United States; 200µm, Fisherbrand, Pittsburg, United States). In order to verify whether a filter perturbs the signal, it was placed on an end-plate of the flow cell and successively joined to another end-plate. A NP solution (as in Section 3.1.3) was then injected and the UV-absorption was measured before and after of the filter. It resulted that all the tested filters perturbed the signal, i.e. retained a large or small amount of NP. Unexpectedly, retention was observed on filters with mesh up to 2000 times larger than the size of the injected NP. NP attachment to the filters could maybe depend on electrostatic charges present on the filter?

In order to reach BTC repeatability, no filter was placed at the bottom of the column. It was replaced by a 2 cm layer of 2 mm glass beads, which diameter is sufficient to prevent their passage through the perforated aluminum support disc. The glass beads were cleaned through the same

protocol used for the sand and it was previously verified that NP do not adhere to them. In order to prevent the mixing of the two porous media during the packing of the column, the column was packed upside-down, the glass beads were added at the end of the packing process and the column was then turned bottom-up, as showed in Section 3.1.2.

**Water Related Problems.** All solutions were prepared from fresh DI water. The DI water was ensured from an Aquadem filter system. The state of consumption of the resins that ensure the water filtration resulted to tend to impact on the stability of the NP suspensions.

Several buffers, e.g.  $\text{NaHCO}_3$ , were tested to adjust the NP solution to pH 10. The use of a buffer simplify the equilibration of the porous medium, since it limits the sand natural buffering power, which tends to acidify the basic solutions that were injected. A buffer can shorten the time needed to have a pH close to the inlet pH at the outlet of the column. All the tested buffer resulted to have some kind of affinity with  $\text{TiO}_2$  NP destabilizing the NP solution and inducing a dramatic increase in NP hydrodynamic diameter. Only KOH and NaOH showed a compatibility with the stability of NP suspensions. KOH was adopted since the tracer transport experiments were already realized with KCl. Since the buffering power of KOH is smaller near the neutral pH due to the carbonation, pH 10 was adopted for the  $\text{TiO}_2$  NP solutions, which is also a good choice to minimize the sand-NP interactions.

## 3.2 MODELING

### 3.2.1 INVERSE PROBLEM RESOLUTION

The transport and retention of  $\text{TiO}_2$  NP through the porous media was simulated using the convection-dispersion equation model coupled with a kinetic retention term (Section 1.3.3):

$$\begin{cases} \frac{\partial \theta C}{\partial t} + \rho \frac{\partial s}{\partial t} = \frac{\partial}{\partial z} \left( \theta D \frac{\partial C}{\partial z} \right) - \frac{\partial q_d C}{\partial z} \\ \rho \frac{\partial s}{\partial t} = \theta k_a \psi C \\ \psi = 1 - \frac{s}{s_{max}} \end{cases} \quad (3.5)$$

NP retention was assumed to be irreversible and time- and concentration-dependent. Accordingly  $\psi$  decreases over time and with an increasing amount of retained NPs. It is a retention function associated with blocking, a retention mechanism related to the filling of porous media attachment sites. Adopting this model, NPs were

supposed to interact with a limited amount of attachment sites ( $s_{\max}$ ) in porous media, such as metal oxide surfaces or roughness of the collector surface. Therefore, as the number of occupied sites is increasing throughout an experiment, the probability of a NP to encounter a free site decreases (Ryan and Elimelech 1996).

In the modeling, hydrodynamic parameters ( $\phi$ ,  $\alpha_L$ ) obtained from tracer experiments were prescribed, while  $k_a$  and  $s_{\max}$  values were optimized to fit the BTC. HYDRUS-1D (Šimunek et al. 2008) (version 4.16) was used to solve both direct and inverse problems, applying the Levenberg-Marquardt algorithm for parameter optimization (Section 1.4.1). The convection-dispersion equation was solved by prescribing the Darcy flux and applying boundary conditions corresponding to the measured inlet concentration (bottom of the column). A zero-concentration gradient condition was applied at the outlet (top of the column). The 15.2 cm profile was discretized into equidistant 501 nodes.

### 3.2.2 OPTIMIZED TRANSPORT PARAMETERS

The adopted retention model, together with optimized parameters, provides a good description of the BTC ( $R^2 > 0.94$ , Table 3.1, Figure 3.4). It should be noted that the parameters at  $v = 0.002$  cm/s, unlike at other velocities, are strongly correlated (-0.94). This large correlation value is attributable to the BTC's poor signal variation nonmonotonic shape, which cannot be properly described by the model (Liang et al. 2013b).

The optimized parameters (Table 3.1) show a strong correlation with pore water velocity. Increases in  $v$  are accompanied by an attachment coefficient  $k_a$  increase and a maximal solid phase concentration  $s_{\max}$  decrease. Thus, higher retention is not associated with a larger attachment kinetics ( $k_a$  is a frequency). In contrast, higher retention is related to smaller kinetics, resulting from a longer residence time. Residence time, determined by the pore water velocity and column length, is therefore a key parameter for NP retention. Considering  $s_{\max}$  as the number of attachment sites accessible to NPs, this behavior could be interpreted as a reduction in the number of sites 'seen' by NPs when the water velocity increases. However, if the kinetic energy of a particle becomes larger, stronger energy bonds are needed to retain the particle after collision. Consequently, the sites that do not have sufficient attractive energy will not interact with the particle, and the  $s_{\max}$  value decreases. According to the DLVO calculations (Figure 2.2), a very weak (-0.13 kBT) secondary minimum is expected in the particle-collector energy profile. A relation between  $s_{\max}$  and this secondary energy minimum could occur, being the secondary energy minima considered responsible for retention under unfavorable conditions (Liang et al. 2013b; Tufenkji and Elimelech 2005b).

$v$ (cm/s)	M (%)	$\eta_0$ (-)	$s_{\max}/C_0$ (cm <sup>3</sup> /g)	$k_a$ ( $\times 10^{-4}$ s <sup>-1</sup> )	Corr (-)	R <sup>2</sup> (-)	O (-)
0.002	95	0.14	$1.2 \pm 0.1$	$5.5 \pm 0.4$	-0.94	0.94	0.002
0.012	45	0.04	$0.31 \pm 0.01$	$13 \pm 1$	-0.07	0.98	0.090
0.07	13	0.01	$0.113 \pm 0.008$	$15 \pm 1$	-0.28	0.98	1.470

Table 3.1: Experimental and optimized parameters for the NP transport experiments at different pore water velocities under 5 mM KCl. Errors represent the 95% confidence interval.  $v$ , average pore water velocity; M, retained mass percentage;  $\eta_0$ , calculated single collector efficiency;  $s_{\max}/C_0$ , maximal solid phase concentration;  $k_a$ , optimized attachment coefficient; Corr, correlation between optimized parameters  $s_{\max}$  and  $k_a$ ; R<sup>2</sup>, Pearson's correlation coefficient for parameter optimization; O, objective function value.

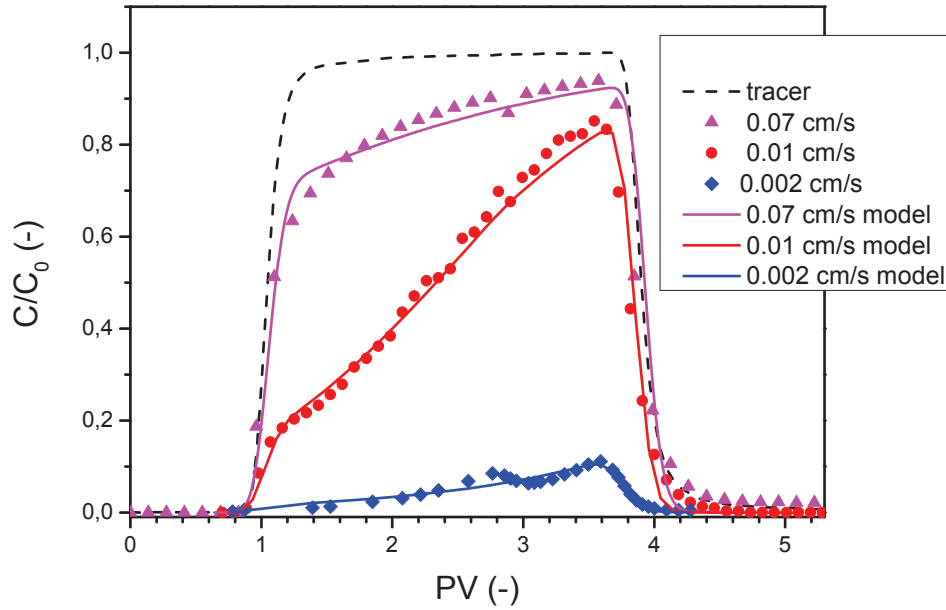


Figure 3.4: Breakthrough curves for 5mM under different water velocities and calibrated model previsions. The outlet NP concentration is normalised by the inlet concentration. Each BTC is the result of a single experiment and it is not the average of the replicas. The two parameters of the retention model ( $k_a$ ,  $s_{\max}$ ) were optimized for each BTC.

$v$ (cm/s)	$k_a$ ( $\times 10^{-4} \text{ s}^{-1}$ )	$R^2$ (-)	O (-)	$\alpha_{pc}$ (-)	$k_{cal}$ ( $\times 10^{-4} \text{ s}^{-1}$ )	$R^2_{cal}$ (-)	$O_{cal}$ (-)
0.002	$5.5 \pm 0.4$	0.94	0.002	0.106	6.20	0.94	0.008
0.012	$13 \pm 1$	0.98	0.090	0.153	10.35	0.96	0.152
0.07	$15 \pm 1$	0.98	1.470	0.103	17.00	0.98	1.518

Table 3.2: Experimental and optimized parameters for the NP transport experiments at different pore water velocities under 5 mM KCl. Errors represent the 95% confidence interval.  $v$ , average water pore velocity;  $k_a$ , optimized attachment coefficient;  $R^2$ , Pearson's correlation coefficient for parameter optimization; O, objective function value;  $\alpha_{pc}$ , calculated attachment efficiency;  $k_{cal}$ , attachment coefficient calculated with  $\alpha_{pc} = \widetilde{\alpha}_{pc} = 0.12$ ;  $R^2_{cal}$ , Pearson's correlation coefficient for new model fit;  $O_{cal}$ , objective function value for new model.

### 3.2.3 ATTACHMENT EFFICIENCY ANALYSIS

According to classical filtration theory, the attachment coefficient  $k_a$  is related to the attachment efficiency  $\alpha_{pc}$  and the single collector efficiency  $\eta_0$  (Section 1.3.3):

$$k_a = \frac{3(1 - \phi)q_D}{2d_c\phi} \alpha_{pc}\eta_0 \quad (3.6)$$

The single collector efficiency  $\eta_0$  represents the fraction of approaching particles that collide with collector grains, while the attachment efficiency  $\alpha_{pc}$  is the fraction of collisions that results in attachment. The product of  $\alpha_{pc}$  and  $\eta_0$  gives the single collector removal efficiency  $\eta$  [-] (Ryan and Elimelech 1996). The value of  $\eta_0$  (Table 3.1) was calculated based on the model of Tufenkji and Elimelech (2004). The value of  $\alpha_{pc}$  was calculated (Table 3.1) from optimized  $k_a$  values and  $\eta_0$  values, previously calculated (Section 3.1.5), through Equation 3.6. The  $\alpha_{pc}$  values obtained under different water velocities are similar (Table 3.2), suggesting that  $\alpha_{pc}$  is a parameter independent of water velocity in the range of adopted velocities. In the literature, the dependence of  $\alpha_{pc}$  on hydrodynamic factors is still a controversial topic. In previous studies,  $\alpha_{pc}$  was assumed to be unaffected by water velocity (Elimelech 1992), while, elsewhere, a decrease (Anders and Chrysikopoulos 2005; Lecoanet et al. 2004) or an increase (Kim and Lee 2014) of  $\alpha_{pc}$  was observed when the water velocity increases. Other studies reported the existence of a critical flow velocity (Shen et al. 2010; He et al. 2009). According to Shen et al. (2010), the attachment efficiency does not change with the increase of water velocity until a critical value is attained. This critical value is not reached under our experimental conditions and therefore, the attachment

efficiency is independent of hydrodynamics.

### 3.2.4 EQUATION FOR WATER VELOCITY EFFECT ON TRANSPORT PARAMETERS

To find tendencies that could help in modeling retention mechanisms, the mutual correlation between retention model parameters and filtration parameters was studied. Linear relations were found for  $k_a$  as a function of  $\eta_0$  (Figure 3.5):

$$k_a = a_1\eta_0 + a_2 \quad (3.7)$$

as for  $s_{max}$  :

$$s_{max} = a_3\eta_0 \quad (3.8)$$

where the empirical parameters  $a_1$  [ $s^{-1}$ ],  $a_2$  [ $s^{-1}$ ] and  $a_3$  [ $cm^3/g$ ] are equal to  $(-9.06 \pm 0.01) \times 10^{-4} s^{-1}$ ,  $(16.00 \pm 0.01) \times 10^{-4} s^{-1}$  and  $8 \pm 0.1 cm^3/g$ . These linear equations accurately describe experimental BTCs and predict NP behavior for any pore water velocity in the studied range, at least under these experimental conditions. Gravity effects are not taken into account since the NP size is smaller than 500 nm (Lazouskaya et al. 2011). Retention mechanisms other than blocking are not considered in the model. Moreover, given the similarity of  $\alpha_{pc}$  values for different water velocities, the attachment efficiency was assumed to be independent of the fluid velocities as discussed in Section 3.2.3 and its arithmetic average value ( $\widetilde{\alpha_{pc}} = 0.12 \pm 0.3$ ) was used in the following. Using this new parameter,  $k_a$  was subsequently recalculated through Equation 3.6:

$$k_{cal} = \frac{3(1-\phi)q_D}{2d_c\phi} \widetilde{\alpha_{pc}}\eta_0 \quad (3.9)$$

where  $k_{cal}$  is an expression for  $k_a$  that does not depend on BTC shape. Recalculated values deviate by 13-22% from optimized values, without a definite trend (3.5). Transport simulations of  $TiO_2$  NP were then repeated with  $k_a = k_{cal}$ , obtaining good fits (Figure 3.5b, Table 3.2). These results imply that Equations 3.8 and 3.9 give a sufficiently good prediction of the optimized parameters. We can also observe that the model is weakly sensitive to the attachment efficiency, the results for  $\alpha_{pc}$  and  $\widetilde{\alpha_{pc}}$  being very similar, and that a rough estimation of this value could be sufficient to obtain a good estimation of NP behavior. A similar lack of sensitivity to attachment efficiency has been also reported in the literature (Quik et al. 2014; Praetorius et al. 2012).

## 3.3 CONCLUSION

Transport experiments with  $TiO_2$  NPs were performed in a saturated porous medium, under a range of ionic strengths and water velocities. A great attention was dedicated to the repeatability of the results.



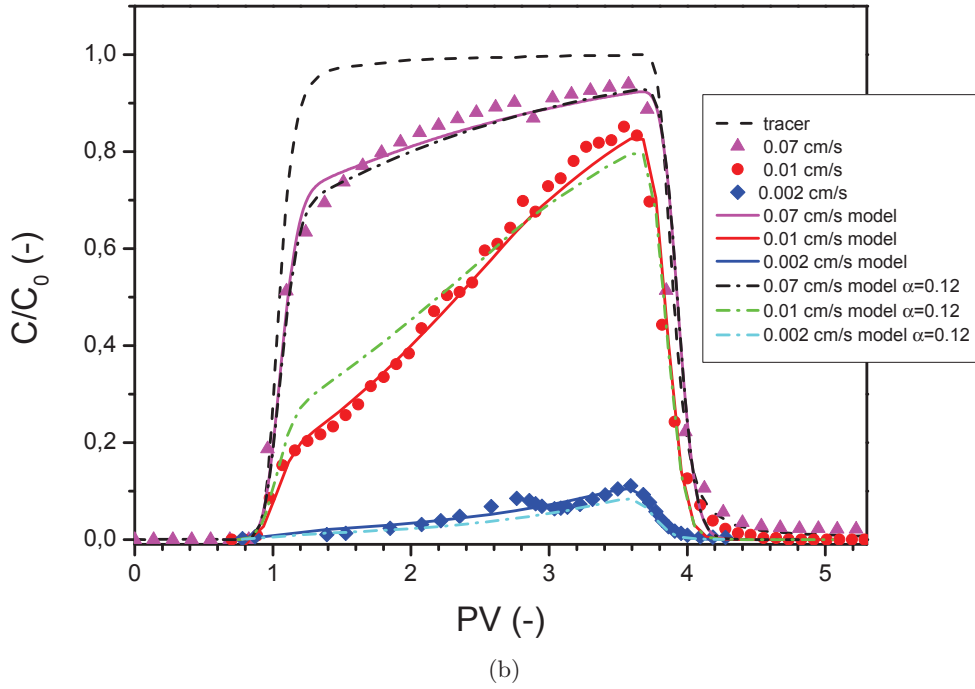
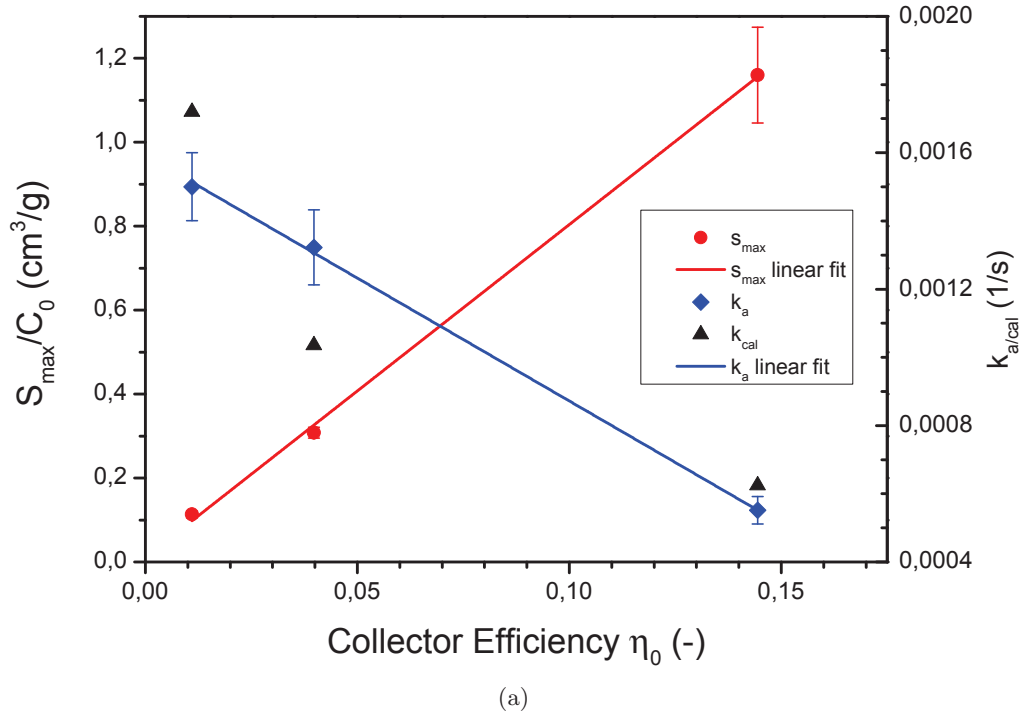


Figure 3.5: a) Model parameters as a function of collector efficiency. Maximal solid phase concentration  $s_{\max}$  and attachment coefficient  $k_a$  are optimized,  $k_{\text{cal}}$  is calculated.  $k_a$  and  $s_{\max}$  are linearly fitted through Equation 3.7 and 3.8. Error bars represent the 95% confidence interval. b) Model predictions for  $\alpha_{pc} = 0.12$  compared to calibrated model.

The breakthrough curves were modeled employing a blocking retention mechanism. A linear behavior as a function of the collector efficiency was observed for the retention parameters of the model. It was also observed that the attachment efficiency does not change with water velocity in the range of studied velocities. The retention model presented in this study, based on empirical relationships between the transport model parameters and the filtration theory parameters, allows the simulation of the transport of  $\text{TiO}_2$  NPs for any pore water velocity in the studied range and, at least, under the experimental conditions described in this study. It is limited to an ionic strength of 5mM KCl.

Future research should investigate the dependence of this retention model on chemical parameters, as pH and ionic strength. The model should be tested with other types of NP too, in order to assess whether the observed behavior is related exclusively to the surface properties of the employed NP and porous material or it can be observed under other conditions.



## CHAPTER 4

---

# TRANSPORT OF NANOPARTICLES IN AN UNSATURATED POROUS MEDIUM

---

### CONTENTS

4.1	Materials and Methods . . . . .	97
4.2	Modeling . . . . .	104
4.3	Conclusion . . . . .	116

---

## 4.1 MATERIALS AND METHODS

### 4.1.1 COLUMN SYSTEM

A COLUMN system with characteristics similar to the one used for the saturated experiments (Section 3.1.1) was used. The flow cell adopted for unsaturated experiments differs by two features: it is longer (3.75 cm in diameter and 30.5 cm in length) and is equipped with two kinds of end-plates: regular end-plates and perforated end-plates, permitting to expose the sand surface to the atmospheric pressure (Figure 4.1).

The water flux was imposed from the top to the bottom of the column, where a 2 cm layer of glass beads held the porous media in place (Figure 4.1c). In order to calculate the pore volume of the columns, the glass beads porosity was assumed to be identical to the sand porosity. The protocol presented in Section 4.1.2 was adopted to prepare the columns for the unsaturated experiments.

Ultraviolet absorption values were measured automatically, every 5 s, throughout the experiments for both inlet and outlet flows by means of on-line sensors. The flow cell was connected to a Monitor UPC-900 (GE Healthcare Bio-Sciences AB, Uppsala, Sweden). In order to ensure a constant water flow and to prevent any tube deformation, the peristaltic pump tube was replaced before each experiment.

Unlike the column system in saturated experiments, pH and conductivity were not measured, since the UV absorption sensor took all the available space at the outlet of the column (14 cm). In fact, in order to control the pressure head boundary condition at the bottom of the column, and thus to control the water content profile of the column, the outlet flow has to be exposed to the atmospheric pressure 14 cm below the lowest sand level (Figure 4.1d). In order to obtain a suitable unsaturated water content profile, the column used in unsaturated experiments was longer than the column used for saturated experiments. In fact, the bottom of the column, i.e. the outlet, must be maintained saturated. This arrangement prevents air from entering the porous media from the outlet of the column, an occurrence that would set to zero the pressure head boundary condition. A longer column ensures an unsaturated profile in the upper half of the porous medium with a progressive increase in water content, until it reaches saturation, in the lower half of the porous medium. A 30 cm column with a -14 cm head lower boundary condition results in 15 cm of stationary unsaturated profile (Section 4.2.1).

#### 4.1.2 EXPERIMENTAL PROTOCOL FOR PREPARATION OF THE UNSATURATED POROUS MEDIUM

- Water flux was imposed from the bottom to the top of the column. A 8  $\mu\text{m}$  paper filter (GE Healthcare Bio-Sciences AB, Uppsala, Sweden) was placed at the bottom of the column, on a regular top, in order to hold the sand in place;
- The column was wet-packed as uniformly as possible with cleaned sand (Section 2.2.2), adding 1 cm of sand at a time, gently tapping the column from time to time and maintaining the water level 1 cm over the sand level throughout the process;
- The last 2 cm of the column were packed with 2 mm glass beads. A regular top was put in place;
- The column was turned upside down and equilibrated at the desired IS and pH 10 with approximately 20 pore volumes (PV) of electrolyte solution;
- Once the outlet of the column sealed with a clamp, the regular top of the column, previously the bottom, was removed together with the paper filter. A perforated top was put in place;
- A water flow of 0.0012 cm/s was then applied, the clamp was removed and the column was let draining with a bottom imposed pressure head of -14

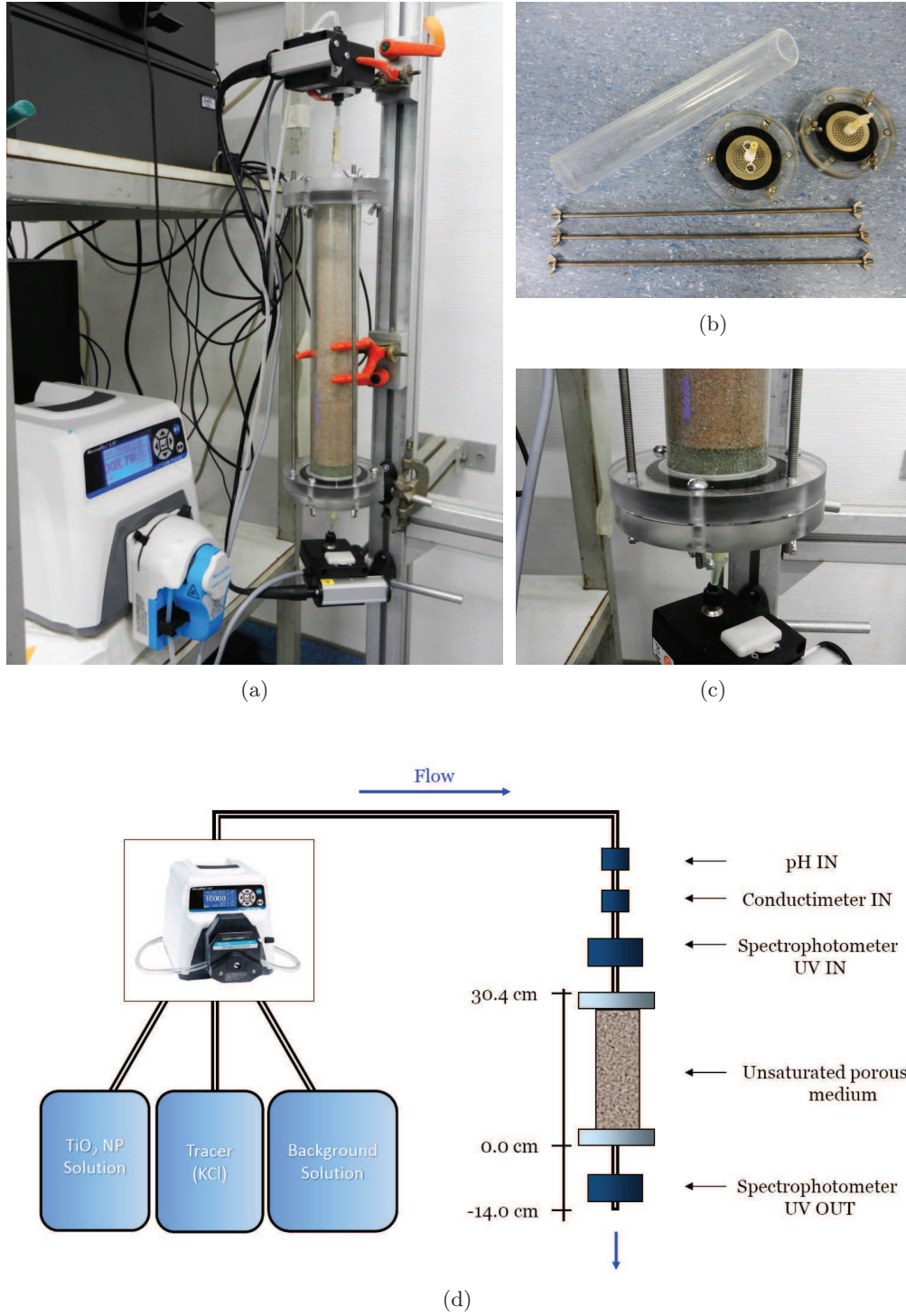


Figure 4.1: (a) Picture of the column set up for unsaturated transport experiments. On the left the peristaltic pump and the UPC monitors can be seen. (b) Flow cell elements. A regular and a perforated end-plate can be seen in the picture. (c) Detail of the glass beads layer that replace the bottom membrane. (d) Experimental set up for the unsaturated experiments.

cm. This operation brings the column from an initial hydrostatic profile to a new time constant saturation profile;

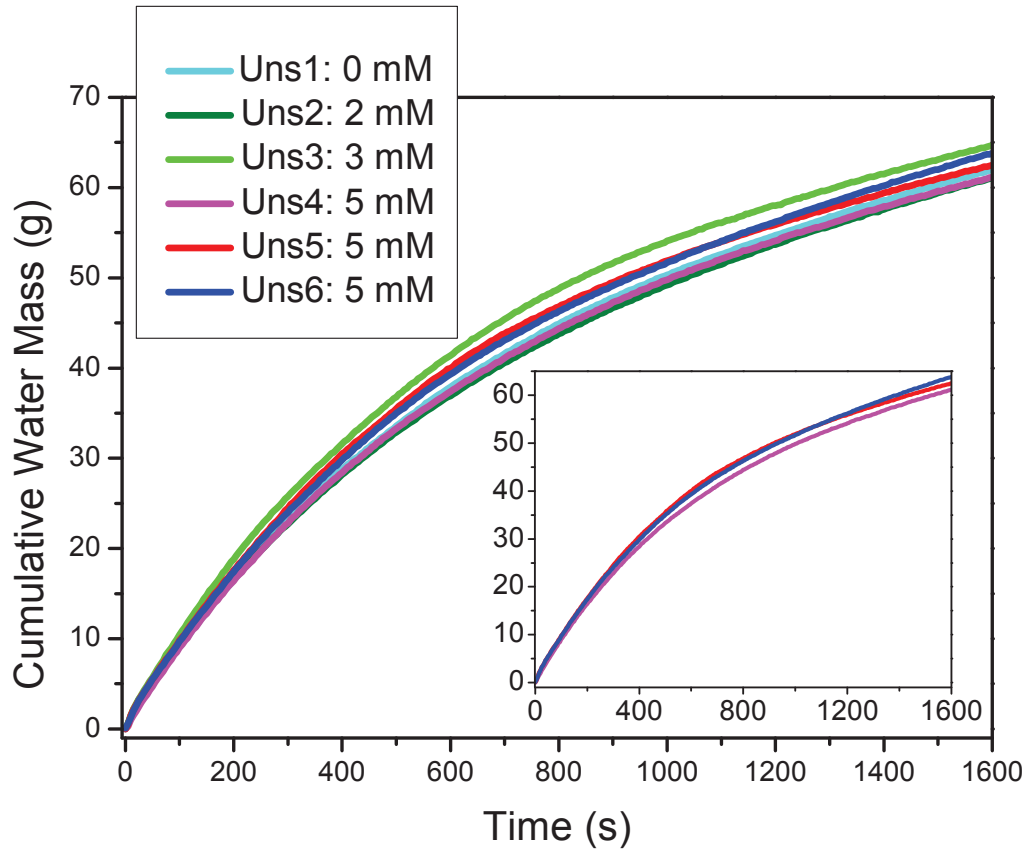
- An unsaturated porous media was obtained, with a flux from the top to the bottom of the column. A 2 cm layer of glass beads held the porous media in place.

#### 4.1.3 EXPERIMENTAL PROTOCOL FOR NANOPARTICLE TRANSPORT UNDER UNSATURATED CONDITIONS

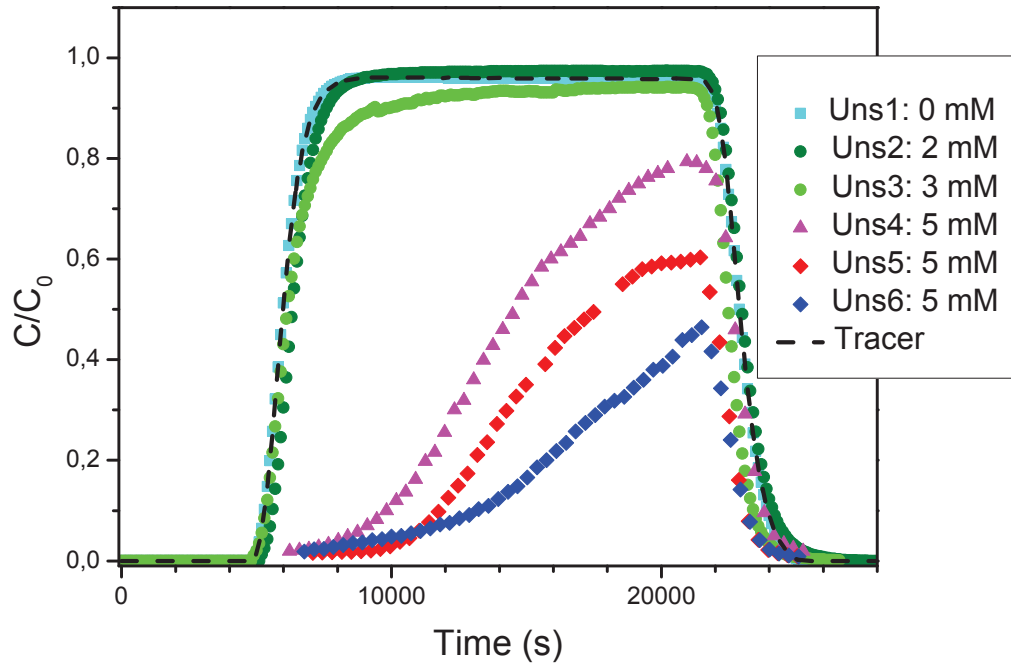
- The column was wet-packed with cleaned sand and prepared according to the protocol;
- 0.5 L of 50 mg/L  $\text{TiO}_2$  fresh suspension was prepared in a graduated glass flask as in Section 3.1.3;
- Each experiment resulted in a 2.5 PV injection of the 50 mg/L  $\text{TiO}_2$  NP suspension, at pH 10. Experiments were conducted with an IS of 0-2-3-5 mM KCl, with an average darcy velocity of 0.0012 cm/s and with an average saturation between 60% and 70%. The NP suspension was stirred throughout the experiments. In order to exclude the possibility that measurements were perturbed due to NP fixed inside the sensors, outlet flow was also sampled by a fraction collector every 6 minutes. When necessary, samples were analysed by a bench top UV-spectrophotometer and the results were compared to online measurements;
- The electrolyte solution was injected until a complete breakthrough curve (BTC) was attained (approximately 2 additional PV);
- The peristaltic pump was turned off and the column totally drained.

#### 4.1.4 CUMULATIVE WATER MASS

Even if all the columns were prepared with the same protocol, the drainages resulted in cumulative water masses differing one another up to 5% (Figure 4.2a). Taking into account that the water velocity and the pressure head imposed at the bottom of the columns are the same for all experiments, the cause can probably be found in the unstable gravitational drainage process and in a heterogeneity of the porous media resulting from the complex packing process. These small differences in the cumulative masses imply the presence of differences in the water content profiles. In Section 4.2.1 the water flow of each experiment is modeled, using the cumulative water mass data and the previously identified Mualem-van Genuchten parameters.



(a)



(b)

Figure 4.2: (a) Cumulative water masses of the transition between the hydrostatic profile and the steady unsaturated profile. In the miniature the data of the 5 mM KCl experiments only were represented. (b) Breakthrough curves of the unsaturated transport experiments with a Darcy velocity of 0.0012 cm/s under an ionic strength of 0-2-3-5 mM KCl. The water content profile differs from a column to another, the average saturation is between 64% and 70%.



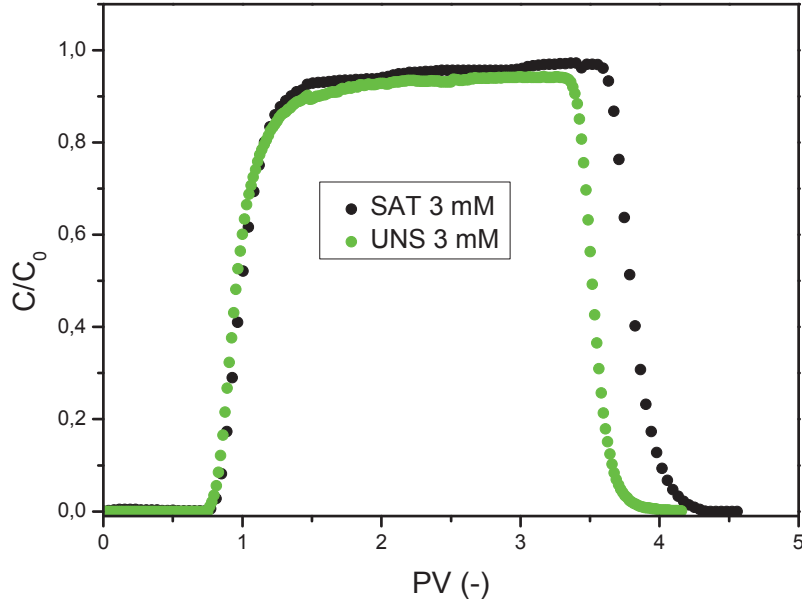


Figure 4.3: Breakthrough curve of the 3 mM KCl saturated experiment with a pore water velocity of 0.002 cm/s (SAT 3 mM) and breakthrough curve of the 3 mM KCl unsaturated experiment (UNS 3 mM, average pore water velocity 0.005 cm/s). The BTC are represented as a function of the eluted pore volumes. The volume of injected NP solution is different for the two BTC: 2.5 pore volumes for the unsaturated experiment and 3 pore volumes for the saturated experiment.

#### 4.1.5 BREAKTHROUGH CURVES

Column experiments were performed under four IS (0-2-3-5 mM KCl). Transport of  $\text{TiO}_2$  NP at 0 and 2 mM KCl does not result in retention. Instead, under 3 and 5 mM KCl the BTCs show a retention that increases as water velocity decreases (Figure 4.2). The experiments with an IS of 0, 2 and 3 mM were conducted at least in duplicata, while the experiments with an IS of 5 mM resulted in different BTC. This lack of repeatability is probably due to the insufficient control obtained on the water content profile, which influences the retention of NP. It can be related to the lack of repeatability of the water cumulative masses of the drainages and to 3D effects. In fact, the gravitational drainage being an unstable process, a different three-dimensional distribution of the water content could be obtained after each drainage, affecting the NP retention.

The fact that under an IS of 0 mM, 2 mM and 3 mM the BTC are reproducible, but not under 5 mM, could be explained assuming that NP are retained from the

interface between air and water (AWI) under 5 mM but not under smaller ionic strengths. Another fact that supports the previous assumption is the following. The BTC of the unsaturated 3 mM experiment and the BTC of the saturated 3 mM experiment with the 0.002 cm/s pore water velocity were represented as a function of the eluted pore volumes (Figure 4.3). It can be observed that, considering the difference in TiO<sub>2</sub> NP solution volume injected (3 PV for the saturated experiment and 2.5 for the unsaturated experiment), the BTC are almost overlapping. The pore water velocities in the two experiments are similar: the saturated experiment have a 0.002 cm/s pore water velocity, while the unsaturated experiment have an average pore water velocity of 0.005 cm/s. This observation allows to affirm that: 1) in both experiments the same retention mechanisms occurs 2) in the 3mM unsaturated experiment retention on the SWI occurs only 3) in 5 mM unsaturated experiments attachment to the AWI likely occurs, producing the observed BTC variability.

As for the saturated experiments, the shapes of the elution curves are typical of blocking behavior. This retention mechanism, resulting in an increase of NP concentration over time in the elution, consists in the progressive saturation of the attachment sites. Considering the unsaturated conditions, in the 5mM experiments a fraction of the available attachment sites is probably positioned on the charged AWI. All BTC shapes are monotonic and show a change in convexity. The exit time of the 5 mM BTC results retarded compared to the tracer BTC and to the BTC at lower IS.

#### 4.1.6 CHALLENGES RELATED TO UNSATURATED EXPERIMENTS

The unsaturated experiments were realized after the saturated experiments. In a first time the arrangements to obtain a good repeatability under saturated conditions were adopted (Section 3.1.7), but problems related to the unsaturated porous medium were faced. The data used in this study required 49 unsaturated column experiments to be conducted.

In order to obtain an unsaturated profile, two protocols were tested. In the first protocol, once equilibrated the porous medium at the desired IS and pH, a drainage was realized, with a null flow rate at the top and with an imposed bottom pressure head of -15 cm. Once steady state is reached, with a very low saturation, the planned flow rate was applied, in order to obtain an average saturation larger than 50%. Therefore, the first protocol implies a drainage and a successive imbibition. The second protocol, that was finally adopted, does not implies the imbibition, because the drainage was realized with a flow rate that

allows to reach a proper unsaturated profile in one step (Section 4.1.2). In the second protocol a -14 cm bottom pressure head was imposed. The difference between -14 cm and -15 cm ensures a larger saturation in the low part of the column, in order to decrease the probability that air enters the porous media from the outlet of the column.

Even if the conditions are the same, the cumulative water masses differ from each other for both protocols. Since the differences were smaller with the second protocol, it was adopted for the following experiments. Moreover, since the first protocol involves a partial drainage and an imbibition, it would be harder to model the water flow. The Mualem-van Genuchten parameters determined in Section 2.3 could not be used and the hysteresis should be taken into account. The parameters would probably be situated between the drainage curve and the imbibition curve that can be seen in Figure 2.7c, on an incomplete process line.

The non-repeatability of the drainages could be related to the column set up of the unsaturated experiments. Since the bottom membrane was replaced with a layer of glass beads during the preparation of the porous medium, the column has to be turned bottom-up. This operation could induce grain re-arrangement in the porous medium, with an impact on the drainages result. In the unsaturated experiments reported in the literature, the hydraulic gradient is controlled by a vacuum pump (Knappenberger et al. 2014; Zhuang et al. 2009; Torkzaban et al. 2008). At the bottom of the column a nylon membrane is placed as capillary barrier. Maybe this technique could ensure a higher repeatability, but the problems faced with any type of membrane prevent its adoption (Section 3.1.7).

## 4.2 MODELING

### 4.2.1 WATER CONTENT PROFILE MODELING AND $K_s$ ESTIMATION

In order to model the water flow of the 5 mM unsaturated experiments, whose water content profiles differ from each other, the cumulative water masses data were used. The Mualem-van Genuchten hydrodynamic parameters  $\alpha$ ,  $\theta_r$ ,  $\theta_s$ ,  $n$  and  $l$ , estimated for the porous medium in Section 2.3.4, were adopted. The saturated hydraulic conductivity  $K_s$  was estimated for the cumulative water mass of each experiment. It should not be possible to optimize all the Mualem-van Genuchten hydrodynamic parameters through the cumulative water content only, due to their mutual correlation. For this purpose the cumulative water mass of the transient part of the porous medium preparation (CWM1) was used together with the cumulative water mass of the total drainage (CMW2) that follows the

end of the BTC exit. The CWM1 data were cut after the time at which the steady unsaturated profile was reached (around 6000 s) and then were joined to the CWM2 data (Figure 4.4a). This arrangement yields to a better estimation of  $K_s$  and to a decrease in its standard error.

The Richards equation (Section 1.3.1), describing the movement of water in an unsaturated porous medium, was solved through HYDRUS 1-D. At the top of the column a variable flux boundary condition was applied, while a constant pressure head of -14 cm was applied at the bottom of the column. The 30.4 cm profile was discretized into equidistant 305 nodes.

The estimated  $K_s$  values range between 0.012178 cm/s and 0.02071 cm/s (Table 4.1). These values are of the same order of magnitude of the  $K_s$  value obtained through the ROSETTA pedotransfer function (Section 2.3.4). Otherwise, the value estimated for the same porous medium from the drainage-imbibition experiment was an order of magnitude larger. It is acknowledged that the degree of accuracy of the  $K_s$  estimation through that kind of experiments cannot be very high (Beydoun and Lehmann 2006). This difference could be due to the different design of the two columns, to the different packing protocols or to the parameter optimization process. It can be observed that the modeled curve of the water content as a function of the pressure head fits better the plateau than the transient parts of the data. Since  $K_s$  controls the dynamic of the water content changes, this could explain the overestimation of the parameter.

The modeled water content profiles, pressure head profiles and pore water velocity profiles can be seen in Figure 4.4. If in the lower half of the profile the curves are overlapping, in the first 15 cm of the profile each experiment has a different saturation. The water content in the first centimeters ranges from 0.13 to 0.17, in terms of saturation from 0.34 to 0.45 (Table 4.2). Therefore, the first half of the columns have a very low degree of saturation. The pore water velocity profile too, which depends on the water content, is different in each experiment. From the bottom to the top of the profile the pore water velocity can increase by up to 3 times.

The data reported in Table 4.2 show that NP retention increases when the saturation decreases. Since the AWI is supposed to increase when saturation decreases, this observation supports the assumption that NP are retained from the AWI.

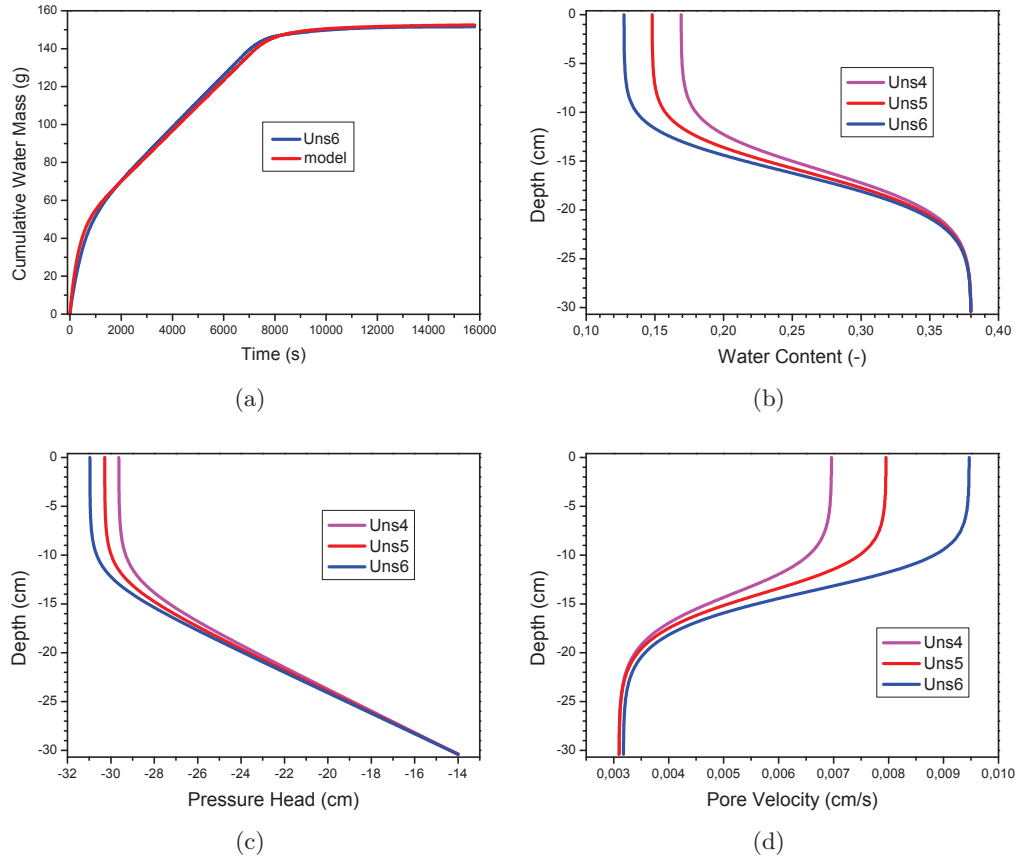


Figure 4.4: (a) Cumulative water mass of the UNS6 unsaturated experiment with the model prediction issued from the  $K_s$  estimation. (b) Modeled water content profiles for the 5 mM unsaturated experiments. (c) Modeled pressure head profiles for the 5 mM unsaturated experiments. (d) Modeled pore water velocity profiles for the 5 mM unsaturated experiments.

	Injection Time	Flow Rate	$K_s$	O	$R^2$
	(s)	(cm/s)	(cm/s)	(-)	(-)
Uns4	16000	0.001177	$0.0121 \pm 0.0003$	440.0	0.9878
Uns5	16000	0.001177	$0.0175 \pm 0.0002$	150.0	0.9924
Uns6	16300	0.001207	$0.0207 \pm 0.0002$	99.0	0.9972

Table 4.1: Estimated  $K_s$  values for the 5 mM unsaturated experiments and their physical parameters. Errors represent the 95% confidence interval.

	$S_{ave}$	$S_{min}$	$\theta_{ave}$	$\theta_{min}$	M
	(-)	(-)	(-)	(-)	(%)
Uns4	0.70	0.45	0.2677	0.1691	54.3
Uns5	0.67	0.39	0.2549	0.148	70.0
Uns6	0.64	0.34	0.2431	0.1275	80.6

Table 4.2: Average ( $S_{ave}$ ,  $\theta_{ave}$ ) and minimum ( $S_{min}$ ,  $\theta_{min}$ ) values of saturation and water content modeled for the 5 mM unsaturated experiments. Percentage of NP mass retained from the porous medium (M).

#### 4.2.2 FORTRAN CODE WITH TRANSPORT PARAMETERS DEPENDENT ON WATER CONTENT AND WATER VELOCITY

The software HYDRUS 1-D allows to choose between several defined retention models, but the only way to take into account the local water content is to divide the porous medium in layers and introduce many retention parameters. Since it is acknowledged that the degree of saturation of a porous medium and the presence of the AWI influence the retention of colloids, virus and NP (Zhang et al. 2012; Torkzaban et al. 2008; Bradford and Torkzaban 2008), the adoption of retention parameters dependent on the water content could yield to a more realistic model and to a better understanding of the physical processes. It is in this perspective that a fortran code was developed, to introduce water content and/or water velocity dependent parameters and, more in general, a greater flexibility in the choice of the retention model.

The same boundary conditions used in HYDRUS 1-D are prescribed, obtaining the same  $\theta$  and  $h$  profile. For the parameter estimation, the routine BCLSF of the IMSL Fortran Numerical Library was used (Visual Numerics 2014). This routine uses a modified Levenberg-Marquardt method with strong convergence

properties, called 'trust region algorithm', to solve nonlinear least squares problems subject to simple bounds on the variables. The Jacobian is not analytically calculated from the routine but estimated through the perturbation method. The following stopping criteria are applied:

1. The norm of the function is less than the absolute function tolerance, defined as  $\max(10^{-20}, \epsilon^2)$ , or  $\max(10^{-40}, \epsilon^2)$ , where  $\epsilon$  is the machine precision;
2. The norm of the scaled gradient is less than the given gradient tolerance, defined as  $\sqrt{\epsilon}$  or  $\sqrt[3]{\epsilon}$ ;
3. The scaled distance between the last two steps is less than the step tolerance  $\epsilon^{2/3}$ .

#### 4.2.3 TRANSPORT MODELING

Once modeled the water flow as in Section 4.2.1, two approaches were used to model the transport and the retention of the  $\text{TiO}_2$  NP under unsaturated conditions. As in the modeling under saturated conditions, the convection-dispersion equation coupled with a retention term was applied (Section 3.2.1):

$$\frac{\partial \theta C}{\partial t} + \rho \frac{\partial s}{\partial t} = \frac{\partial}{\partial z} \left( \theta D \frac{\partial C}{\partial z} \right) - \frac{\partial q_d C}{\partial z} \quad (4.1)$$

This equation, if a single attachment model is applied, depends on two parameters:

$$\rho \frac{\partial s}{\partial t} = \theta C k_a^{uns} \left( 1 - \frac{s}{s_{max}^{uns}} \right) \quad (4.2)$$

where  $k_a^{uns}$  is the frequency of successful collisions between NP and the attachment surfaces and  $s_{max}^{uns}$  is the maximal concentration of NP that can be retained from the porous medium. Two different approaches were used:

- A first approach consisted simply in optimizing the parameters through the software HYDRUS-1D, as in Section 3.2.1. The resulting model, which is dependent on two parameters, is hereinafter referred to as 2P;
- A second approach consisted in applying a model, dependent on three parameters, which describe  $k_a^{uns}$  and  $s_{max}^{uns}$  as a function of the water content and of the pore water velocity, and in optimizing its parameters through the fortran code described in Section 4.2.2. This model is hereinafter referred to as 3P.

#### 4.2.3.1 3P RETENTION MODEL DEPENDENT ON WATER CONTENT AND ON PORE WATER VELOCITY

This model considers  $k_a^{uns}$  and  $s_{max}^{uns}$  (Equation 4.2) as water content and pore water velocity dependent parameters and takes into account the presence of the interface between air and water:

$$\begin{cases} k_a^{uns} = \frac{3(1-\theta)q_D}{2d_c\theta} \widetilde{\alpha}_{pc}\eta_0 + \left( \frac{3q_D}{2d_c\theta} \alpha_{pc}^{AWI}\eta_0 + a_2^{AWI} \right) \left( 1 - \frac{\theta}{\theta_s} \right) \\ s_{max}^{uns} = a_3\eta_0 \left( \frac{\theta}{\theta_s} \right)^{2/3} + a_3^{AWI}\eta_0 \left( 1 - \frac{\theta}{\theta_s} \right)^3 \end{cases} \quad (4.3)$$

where  $\alpha_{pc}^{AWI}$  [-],  $a_2^{AWI}$  [s<sup>-1</sup>] and  $a_3^{AWI}$  [cm<sup>3</sup>/g] are empirical parameters. The parameters  $a_3$  and  $\alpha_{pc}$  are the same used for the modeling under saturated conditions. The first term in the right side of both equations is related to the retention on the sand water interface, while the second term is related to the retention on the air water interface. Once renamed the two terms, 4.3 can be written as:

$$\begin{cases} k_a^{uns} = k_a^{SWI} + k_a^{AWI} \\ s_{max}^{uns} = s_{max}^{SWI} + s_{max}^{AWI} \end{cases} \quad (4.4)$$

Equations 4.3 are developed from the linear relations found for the saturated transport (Section 3.2.1):

$$\begin{cases} k_a^{sat} = \frac{3(1-\phi)q_D}{2d_c\phi} \widetilde{\alpha}_{pc}\eta_0 \\ s_{max}^{sat} = a_3\eta_0 \end{cases} \quad (4.5)$$

where  $k_a$  and  $s_{max}$  are renamed  $k_a^{sat}$  and  $s_{max}^{sat}$ . The idea on which the model 3P is based is to maintain the model developed for NP retention under saturated conditions (Equation 4.5) and to integrate it with a term describing the retention on the AWI. The retention under saturated conditions is thus assumed to be exclusively due to the SWI. In order to take into account the unsaturated conditions, small corrections are made to 4.5. In the  $k_a^{sat}$  equation,  $\theta$  replaces  $\phi$  (Bradford and Torkzaban 2008). Moreover, it must be considered that under unsaturated conditions not the entire surface of the sand grains is accessible to NP, due to the presence of air in some pores. The variation of the accessible portion of the sand surface was assumed similar to the variation of the specific surface  $\bar{s}$  [cm<sup>2</sup>/g] in a porous medium, composed of spheres, subject to porosity variations (Emmanuel and Berkowitz 2005):

$$\bar{s} = \bar{s}_0 \left( \frac{\phi}{\phi_0} \right)^{2/3} \quad (4.6)$$

where  $\bar{s}_0$  is the specific surface area of a porous medium at a porosity  $\phi_0$ . Assuming the water content variations similar to the porosity variations, the contribution of the SWI related attachment sites to  $k_a^{uns}$  and  $s_{max}^{uns}$  can be written



as:

$$\begin{cases} k_a^{SWI} = \frac{3(1-\theta)q_D}{2d_c\theta} \widetilde{\alpha_{pc}} \eta_0 \\ s_{max}^{SWI} = a_3 \eta_0 \left( \frac{\theta}{\theta_s} \right)^{2/3} \end{cases} \quad (4.7)$$

The retention on the interface between sand and water is expected to be proportional to the specific surface of the AWI. The parameter  $s_{max}^{AWI}$  was therefore assumed proportional to  $(1 - \theta/\theta_s)^3$ , equation used in Zhang et al. (2012) to fit the AWI specific surface. Regarding  $k_a^{AWI}$ , its form is inspired from  $k_a^{SWI}$ . The term  $(1 - \theta)$  was replaced with  $(1 - \theta/\theta_s)$  and an offset was introduced, so that  $k_a^{SWI} \rightarrow 0$  for  $\theta \rightarrow \theta_s$ :

$$\begin{cases} k_a^{AWI} = \left( \frac{3q_D}{2d_c\theta} \alpha_{pc}^{AWI} \eta_0 + a_2^{AWI} \right) \left( 1 - \frac{\theta}{\theta_s} \right) \\ s_{max}^{AWI} = a_3^{AWI} \eta_0 \left( 1 - \frac{\theta}{\theta_s} \right)^3 \end{cases} \quad (4.8)$$

The 3P model can be applied to both saturated and unsaturated conditions, in fact:

$$\begin{cases} \lim_{\theta \rightarrow \theta_s} k_a^{uns} = k_a^{sat} \\ \lim_{\theta \rightarrow \theta_s} s_{max}^{uns} = s_{max}^{sat} \end{cases} \quad (4.9)$$

#### 4.2.4 OPTIMIZED TRANSPORT PARAMETERS

In Figure 4.5 the BTCs modeled through the 2P model and through the 3P model are displayed. In Figure 4.7 the results of the two models are compared: both BTC and retention profiles are represented. In Table 4.3, the optimized parameters of the two models are listed, while the details of the inversion problem resolutions can be found in Annexe. While in the 2P model  $k_a$  and  $s_{max}$  are constant on the entire profile of the porous medium, in the 3P model they evolve with the depth. The profiles of  $k_a$  and  $s_{max}$  of the experiments modeled through the  $\theta$  dependent model are shown in Figure 4.6.

If the BTC of Uns6 can be properly described by both models, the BTCs of Uns4 and Uns5, which present a convexity change, are better fitted by the 3P model. More information about the performance of the models can be obtained from a comparison of the AIC and BIC criteria. The 3P values of both AIC and BIC (Table 4.3) are smaller than the 2P values for two of the three experiments. This means that, even penalizing the model for his third parameter, the 3P model data description is better than the 2P model description. With regard to Uns6, since there is very little difference between the two model predictions, the 2P

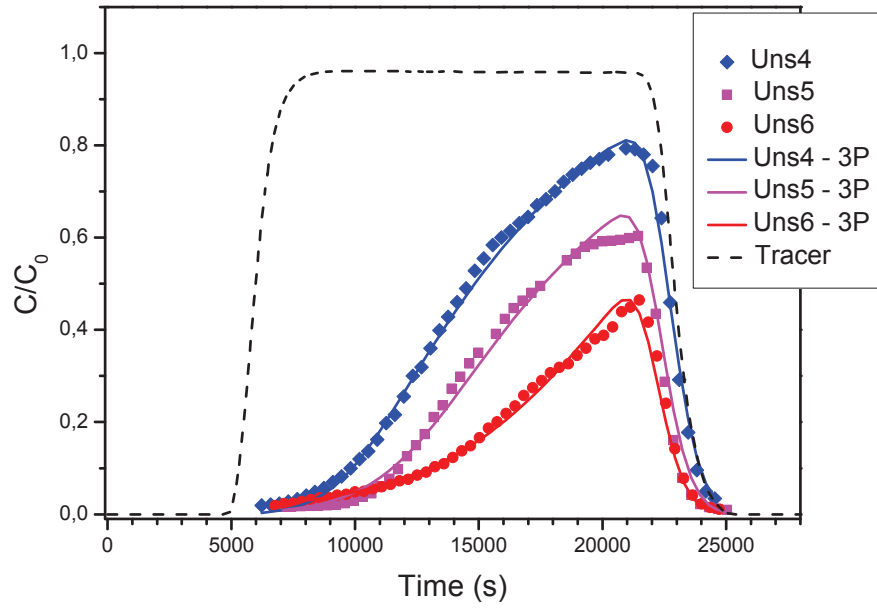
model performance results better because of his smaller number of parameters. The retention profiles predicted by the 2P model are monotonic, with the retained concentration that increases with depth and water content. The retention profiles of the 3P model do not show a unique trend. The profile of Uns6, the experiment with the larger water content, is monotonic, while the profiles of Uns5 and Uns6 are non-monotonic. The larger retention for Uns5 and Uns6 is at the inlet of the column, for Uns4 is at a depth of -20 cm. Since at -20 cm the water content is close to saturation, this behavior suggests that, while in Uns5 and Uns6 a strong retention occurs at the AWI, in Uns4 almost no retention occurs at the AWI.

	$a_2^{AWI}$ ( $\times 10^{-3} \text{ s}^{-1}$ )	$a_3^{AWI}$ ( $\text{cm}^3/\text{g}$ )	$\alpha_{pc}^{AWI}$ (-)	$R^2$ (-)	AIC (-)	BIC (-)	O ( $\times 10^{-3}$ )
Uns4	$0.8 \pm 0.04$	$0.0 \pm 0.04$	$0.2 \pm 0.1$	0.9962	-179	-180	8.46
Uns5	$-5.0 \pm 5.0$	$28.0 \pm 18$	$1.1 \pm 0.7$	0.9894	-148	-149	14.2
Uns6	$1.0 \pm 8.0$	$39.61 \pm 0.08$	$0.0 \pm 1.15$	0.9857	-177	-178	7.5
	$s_{\max}/C_0$ ( $\text{cm}^3/\text{g}$ )	$k_a$ ( $\times 10^{-4} \text{ s}^{-1}$ )	Corr (-)	$R^2$ (-)	AIC (-)	BIC (-)	O (-)
Uns4	$0.22 \pm 0.006$	$3.9 \pm 0.2$	0.035	0.9818	-143	-144	0.0875
Uns5	$0.31 \pm 0.01$	$4.7 \pm 0.4$	-0.2497	0.9538	-119	-120	0.1276
Uns6	$0.4 \pm 0.006$	$6.3 \pm 0.2$	-0.636	0.9867	-180	-181	0.0142

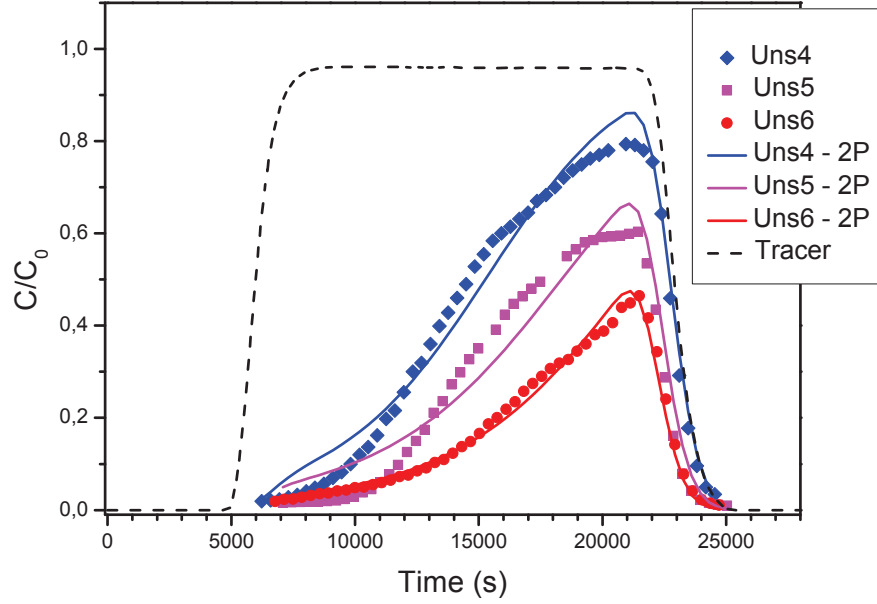
Table 4.3: Optimized parameters of the 3P and 2P models for the unsaturated transport experiments at 5 mM KCl. Errors represent the 95% confidence interval.  $a_2^{AWI}$ ,  $a_3^{AWI}$  and  $\alpha_{pc}^{AWI}$  are the empirical 3P parameters;  $R^2$ , Pearson's correlation coefficient for parameter optimization; AIC, Akaike information criterion; BIC, Bayesian information criterion; O, objective function value;  $s_{\max}/C_0$ , 2P's maximal solid phase concentration;  $k_a$ , 2P's optimized attachment coefficient; Corr, correlation between optimized parameters  $s_{\max}$  and  $k_a$ .

	Uns6			Uns5			Uns4		
	$a_2^{AWI}$	$a_3^{AWI}$	$\alpha_{pc}^{AWI}$	$a_2^{AWI}$	$a_3^{AWI}$	$\alpha_{pc}^{AWI}$	$a_2^{AWI}$	$a_3^{AWI}$	$\alpha_{pc}^{AWI}$
$a_2^{AWI}$	1.000	-0.109	-0.999	1.000	-0.993	-0.9953	1.000	-0.383	0.105
$a_3^{AWI}$	-0.109	1.000	0.103	-0.993	1.000	0.979	-0.383	1.000	-0.190
$\alpha_{pc}^{AWI}$	-0.999	0.103	1.000	-0.995	0.979	1.000	0.1054	-0.190	1.000

Table 4.4: Correlation matrix for the optimization of the 3P model parameters.



(a)



(b)

Figure 4.5: Breakthrough curves of the 5 mM unsaturated experiments modeled by the 3P model (a) and by the 2P model (b). The differences between the BTC are related to the different water content profiles. The average saturation is 70 % for Uns4, 67 % for Uns5 and 64 % for Uns6.

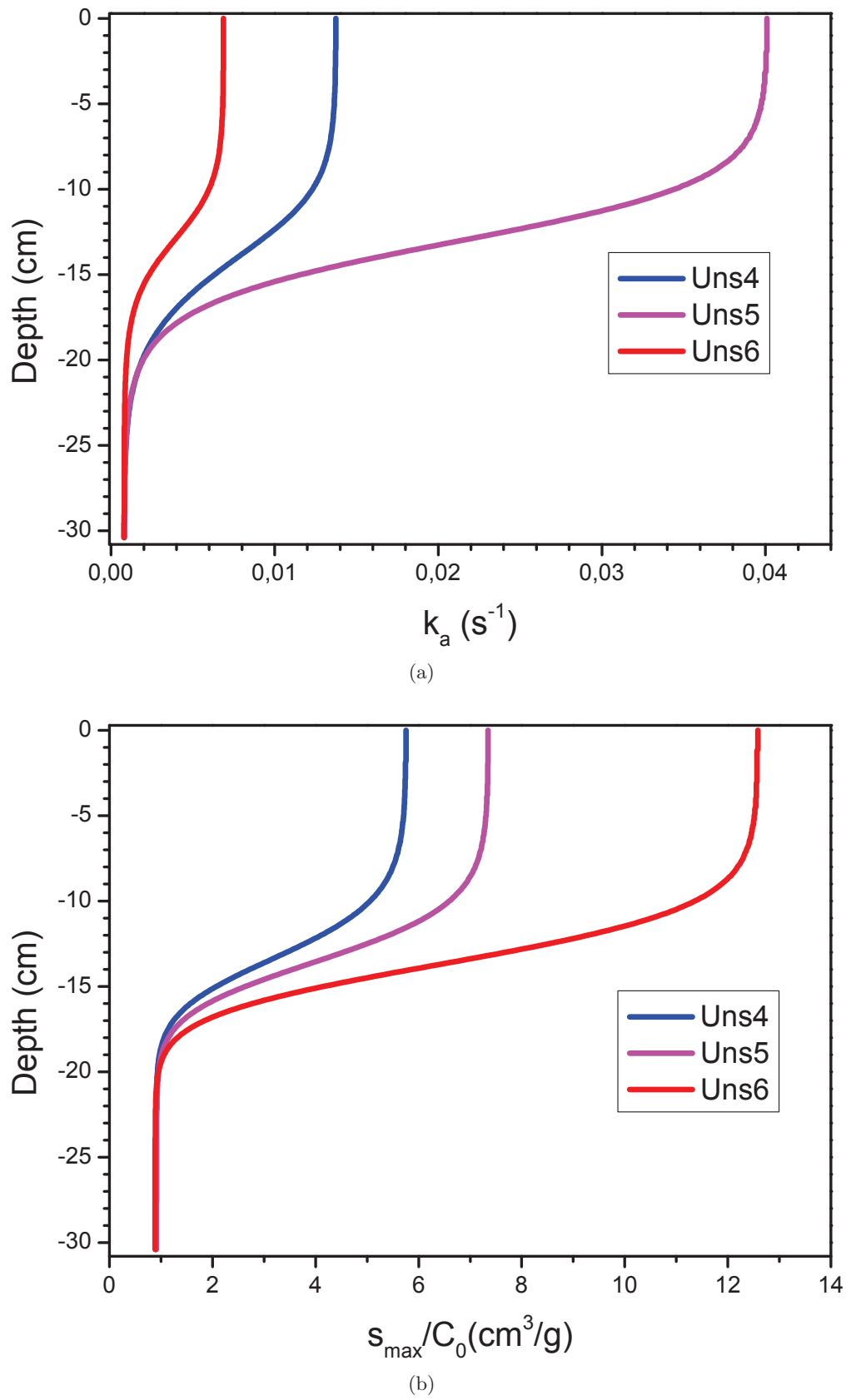


Figure 4.6: Profiles of  $k_a$  (a) and  $s_{max}$  (b) obtained through the 3P model for the unsaturated experiments.

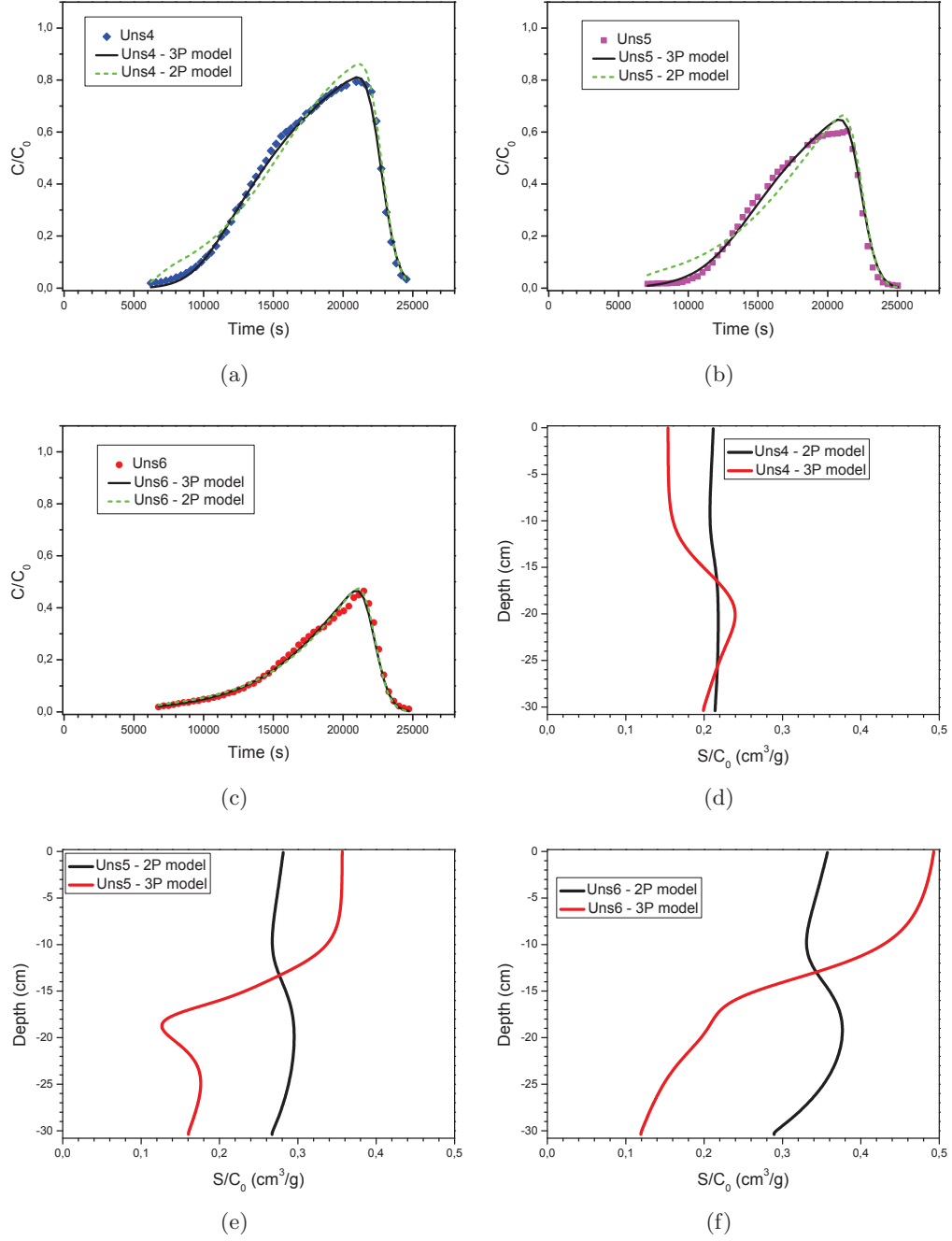


Figure 4.7: Comparison between the predictions of the two models: BTC and retention profiles of the experiments Uns4 (a, d), Uns5 (b, e) and Uns6 (c, f).

### 4.3 CONCLUSION

Transport experiments with  $\text{TiO}_2$  NPs were performed in an unsaturated porous medium, under a range of ionic strengths and water content profile. The NP transport under small ionic strengths ( $< 5$  mM) was not influenced by the water content profile and thus by the interface between air and water. An influence of the water content was observed on the BTCs under an ionic strength of 5 mM KCl. Although a special attention was dedicated to the repeatability of the results, due to a lack of control on the unstable drainage processes, the experiments under 5 mM resulted into different percentages of retained nanoparticles. The BTCs variability could be related to three-dimensional effects too.

The water flow was modeled through the cumulative water mass of the transport experiments and through others specific drainage-imbibition experiments. The breakthrough curves were modeled employing a blocking retention mechanism. Two approaches were used to estimate the retention parameters. The first approach implies to consider the parameters constants along the profile of the porous medium. The second approach implies to consider the parameters as dependent on water content and water velocity. The model 3P was developed following the second approach, obtaining a very good description of the data under an ionic strength of 5mM KCl. This model, taking into account explicitly the water content and the presence of the interface between air and water, allows to better describe the breakthrough curves and to comprehend the role of the AWI as collector of NP.

Since in this study the analysis on the retention profiles were not performed, future research should verify the accuracy of the predicted profiles. The dependence of the 3P model on chemical parameters, as pH and ionic strength should be investigated too. The model should be tested with other types of NP and porous media too, in order to assess whether it could be applied in other contexts.

## CONCLUSION AND PERSPECTIVES

### CONTENTS

5.1	Conclusion . . . . .	117
5.2	Environmental Implications . . . . .	119
5.3	Perspectives . . . . .	121

### 5.1 CONCLUSION

NANOPARTICLES are widely used in the industry due to the properties related to their nanometric size. Since direct and indirect emissions of nanoparticles in the environment occur, leading to a presence of nanoparticles in air, water and soil, it is important to study their impact and their mobility on the environment. Titanium dioxide nanoparticles are among the most manufactured nanoparticles and thus among the most likely present in the environment. This study aimed to understand the behavior of  $\text{TiO}_2$  nanoparticles under saturated and unsaturated conditions, performing column experiments and developing a model to describe the results.

Transport experiments with  $\text{TiO}_2$  nanoparticles were performed, under a range of ionic strengths, water velocities and water contents. A special attention was dedicated to the experimental protocol and to the repeatability of the results. A good repeatability was attained under saturated conditions, while the experiments under unsaturated conditions and large ionic strength (5 mM KCl) resulted into different percentages of retained nanoparticles. The observed variability of the breakthrough curves was probably due to a lack of control on the unstable drainage processes, which yield to a three-dimensional water content distribution. Given the great difficulty of observing and measuring the 3D water content distribution, the porous medium was considered as homogenous in this study.



The breakthrough curves showed an increase in retention when the water content and the water velocity decrease, or when the ionic strength increases. Under unsaturated conditions, the degree of saturation influenced the retention for an ionic strength of 5mM KCl, but not for smaller ionic strengths. It can be deduced that under smaller ionic strengths, the NP are not retained at the interface between air and water. This is an interesting issue, since in the literature it is not clear whether the interface between air and water can retain nanoparticles or not.

The breakthrough curves were modeled through the convective-dispersive equation coupled with a blocking retention term. Two approaches were used to estimate the retention parameters. The first approach implies to consider the parameters constant along the profile of the porous medium. The second approach implies to consider the parameters as dependent on water content and water velocity. The difference between the two approaches can be seen under unsaturated conditions only.

In a first time the breakthrough curves were modeled following the first approach, through the 2P model, optimizing two retention parameters. Under saturated conditions, the 2P model provided a good description of the data. A linear behavior as a function of the single collector efficiency was observed for the retention parameters. It was also observed that under saturated conditions, the attachment efficiency does not change with water velocity in the range of studied velocities. Empirical equations describing the retention parameters under any pore water velocity in the studied range and under the experimental conditions described in this study were developed. These equations are limited to an ionic strength of 5mM KCl. Under unsaturated conditions, the 2P model provided a poor description of the data.

The 3P model, describing the retention parameters as a function of water content and water velocity, was developed following the second approach. The empirical equations found for the saturated conditions, dependent on water velocity, were adapted to this purpose. The equations were modified in order to take into account the reduced accessible specific surface of the sand, due to the unsaturated conditions. They were used to describe the retention at the interface between sand and water. The same equations were modified also in order to take into account the trend that is expected from the retention at the interface between air and water, i.e. to increase when the water content decreases. Three empirical parameters were estimated for this second model, improving the description of the breakthrough curves that was obtained following the first approach. The 3P model can be used under both saturated and unsaturated conditions, since, if the water content tends to the saturation, the model tends to the empirical satu-

rated equations. This second approach, applied to the unsaturated experiments, yields to non monotonic retention profiles, with a larger retention in the zones of the porous medium where the saturation is lower. The first approach, on the contrary, yields to monotonic profiles, with a larger retention in the zones of the porous medium where the saturation is larger.

The 3P model, dependent on water content and water velocity, is a major issue, since it can be used under both saturated and unsaturated conditions, in a quite large range of velocities. Furthermore, it takes directly into account the retention on the interface between air and water. It is yet limited to an ionic strength of 5 mM.

## 5.2 ENVIRONMENTAL IMPLICATIONS

TiO<sub>2</sub> nanoparticles released at the soil surface, under the chemical conditions applied in this study, have small probability to reach the groundwater. In fact, the water table, i.e. the saturated zone of the ground, on average, is positioned few meters under the soil surface. Above the water table is the unsaturated zone, or vadose zone. The water in this zone rises through the soil as a result of capillary force or percolates downward, due to gravity, from the surface to the groundwater. Since, in this study, nanoparticles are strongly retained at the interface between air and water, very small probability exists for them to infiltrate through the unsaturated zone and reach the groundwater.

According to the results of this study, TiO<sub>2</sub> nanoparticles discharged at the soil surface do not represent a risk for the groundwater under average environmental conditions. In the most likely scenario, TiO<sub>2</sub> nanoparticles are retained in the first centimeters of soil. Whether bioavailable, retained TiO<sub>2</sub> nanoparticles could represent a risk for the health of plants, rhizosphere and soil ecosystem in general. A different but unlikely scenario may results from extreme weather conditions, e.g. extreme rainfall events, which may cause the saturation of the vadose zone and the rise of the water table until the soil surface or a dramatically increase in the infiltration water velocity. In this case nanoparticles could be transported at a larger distance, due to the dependence of nanoparticles retention on water velocity and water content. The same could happen under major water bodies, in case of presence of nanoparticles in the water, because rivers and lakes are directly in contact with the groundwater. Moreover, particular soil structures exist that make an aquifer highly vulnerable to pollution, and thus also to nanoparticles pollution, e.g. the fissured aquifers exposed at the surface, where rapid infiltration through fissures can by-pass the unsaturated zone completely

(Chapman et al. 1996).

Environmental predictions based on the results of this study are inaccurate, since issued from a simplified experimental system. The experimental system applied in this study employs quartz sand as porous medium and adopts non-flexible chemical conditions. The following are some remarks on the differences between the simplified system and the environmental conditions:

- In a natural soil the presence of clays and organic matter could enhance the transport of nanoparticles, while the presence of metal oxides could increase their retention;
- The chemistry of the groundwater should also be taken into account. The model developed in this study is valuable for a pH of 10 and an ionic strength of 5 mM KCl. The experimental results showed little retention for an ionic strength smaller than 5 mM KCl. It must be emphasized that for smaller ionic strength no retention was observed at the interface between air and water. For reference, taking into account all dissolved species, the ionic strength of most dilute groundwater is in the range of 10 mM to 1 mM, while seawater has an ionic strength of 700 mM (Deutsch and Siegel 1997). Therefore, an aquifer with a very small concentration of dissolved species could be exposed to nanoparticles contamination, since, according to this study, nanoparticles will be weakly retained from the vadose zone. The type of dissolved species present in the groundwater is of the utmost importance, since nanoparticles have a different affinity with each species;
- The average groundwater pH is 8, but aquifers pH can range from 2 to 12, according to the soil composition (Deutsch and Siegel 1997; Roadcap et al. 2005). The pH, together with the ionic strength, controls the stability of a nanoparticle solution. The closer the groundwater pH is to the nanoparticle isoelectric point, the larger is the nanoparticle hydrodynamic diameter and thus the probability of a mechanical filtration to occur. This trend, in a natural environment, could be countered by the presence of natural organic matter, which works as a surfactant and prevents nanoparticles from homoaggregation;
- The adoption of a real soil, or the performing of field experiments, should be the only way to obtain accurate predictions. At the same time, the measure of the concentration of TiO<sub>2</sub> nanoparticles in the environment is analytically very challenging, since titanium traces are naturally present in soil composition.

## 5.3 PERSPECTIVES

In order to develop a model capable of more accurate predictions, future research should introduce more measures and adopt an experimental system closer to the environmental conditions. Different modeling approaches could also be tested to increase the knowledge of the retention mechanisms.

The measure of the retention profiles and of the nanoparticle hydrodynamic diameters at the outlet of the column system could provide useful information. Retention profiles could be used to test the new developed model and to improve it, obtaining a better identification of the zones of the soil where nanoparticles are expected to be retained. Through the size distribution of the nanoparticles in the breakthrough curves it could be possible to verify if the nanoparticle suspension evolve during the transport or the presence of an eventual filtration of the nanoparticles on the basis of their size.

Even if it could perturb the nanoparticle transport, a measurement of water content and pressure head could be performed in the porous medium during the transport. This could allow the development of a better water flow modeling. In order to study the effects related to the three-dimensional water content distribution, 3D water content measurements could be realized. The gamma-ray tomography or the x-ray tomography techniques could be applied for this purpose.

The dependence of nanoparticle retention on chemical parameters, such as pH and ionic strength, should be investigated. In order to increase the stability of the nanoparticles and approach environmental conditions, natural organic matter could be introduced. In fact, organic matter stabilizes the solution of nanoparticles preventing the flocculation. The model should be tested with other types of nanoparticles too, in order to assess whether the observed behavior is related exclusively to the surface properties of the employed nanoparticles and porous material or whether it can be observed under other conditions.

A progressive complexification of the porous medium could be realized, adding clays, calcium carbonate and organic acids to the quartz sand. The final step should be the study of the transport of nanoparticles in an undisturbed soil sample. This could allow accurate predictions of the mobility of nanoparticles in the vadose zone to be obtained, but it may lead to some analytical problems. In order to conduct experiments in presence of a complex porous medium, a suitable analytical methodology should be identified to measure the nanoparticle concen-

tration in the effluent and in the porous matrix (e.g., ICP-MS).

Once the new experiments performed, the model should be improved by taking into account the effects of the chemical parameters and of the organic matter. Another model could be developed, with a different approach. In the actual model all the nanoparticles are assumed, via the single contact efficiency, to have the same hydrodynamic parameters. In reality, from the hydrodynamic diameter measurements, it results a distribution of particle sizes. The transport of the nanoparticles could be simulated by assigning to each nanoparticle not a size, but a distribution of probability of assuming a certain size. This approach could lead to a more accurate description of the nanoparticle retention and transport in the porous medium.

In order to better describe the retention on the interface between air and water, a 3D retention model could be developed too. Since the gravitational drainage is an unstable process, a different three-dimensional distribution of the water content can be obtained after each drainage, affecting the nanoparticle retention.

---

## NOTATIONS

---

## PHYSICAL CONSTANTS

PARAMETER	VALUE	DESCRIPTION
$\varepsilon_0$	$8.85 \times 10^{-12}$ F/m	Free space permittivity
e	$-1.6 \times 10^{-19}$ C	Electron charge
g	9.81 m/s <sup>2</sup>	Gravitational acceleration
k <sub>B</sub>	$1.38048 \times 10^{-23}$ J/K	Boltzmann constant
N <sub>Av</sub>	$6.022 \times 10^{23}$	Avogadro constant

## ACRONYMS

ACRONYM	DESCRIPTION
2P	Retention model dependent on two parameters
3P	Retention model dependent on three parameters
AWI	Air Water Interface
BTC	BreakThrough Curves
CCC	Critical Coagulation Concetration
CNT	Carbon NanoTubes
DLVO	Derjaguin-Landau-Verwey-Overbeek (Theory)
EDL	Electric Double Layer
IS	Ionic Strength
ISO	International Organization for Standardization
NOM	Natural Organic Matter
NP	NanoParticles
PZC	Point of Zero Charge
REV	Representative Elemental Volume
SEM	Scanning Electron Microscope
SWI	Sand Water Interface

## GREEK LETTERS

PARAMETER	UNITS	DESCRIPTION
$\alpha$	$\text{m}^{-1}$	van Genuchten-Mualem model parameter
$\alpha_{pp}$	-	Attachment coefficient or sticking factor for particle-particle collisions
$\alpha_{pc}$	-	Attachment coefficient for particle-collector collisions
$\alpha_{pc}^{AWI}$	-	Parameter of the 3P model
$\widetilde{\alpha}_{pc}$	-	Average $\alpha_{pc}$ value
$\alpha_L$	m	Longitudinal dispersivity
$\alpha_T$	m	Transverse dispersivity
$\varepsilon_r$	-	Relative permittivity
$\epsilon$	-	Machine precision
$\zeta, \zeta_1, \zeta_2$	V	Zeta potential
$\eta_0$	-	Single collector efficiency
$\eta_D$	-	Diffusion contribution to single collector efficiency
$\eta_I$	-	Interception contribution to single collector efficiency
$\eta_G$	-	Sedimentation contribution to single collector efficiency
$\kappa^{-1}$	m	Debye length
$\kappa_i$	$\text{m}^2$	Intrinsic permeability
$\lambda_d$	m	Characteristic wavelength of the interaction in the Van der Waals potential equations
$\mu$	Pa s	Viscosity
$\rho_f$	$\text{kg}/\text{m}^3$	Fluid density
$\rho_p$	$\text{kg}/\text{m}^3$	Particle density
$\tau$	-	Tortuosity factor
$\phi$	-	Porosity
$\phi_0$	J	Surface potential
$\phi_{dlvo}$	J	DLVO potential
$\phi_{edl}$	J	Electric double layer potential
$\phi_{edl\ s-s}$	J	EDL potential for sphere-sphere interaction
$\phi_h$	J	Helmholtz layer potential
$\phi_{ii}$	J	London interaction between two induced dipoles
$\phi_{pi}$	J	Debye interaction between a dipole and an induced dipole
$\phi_{pp}$	J	Keesom interaction between permanent dipoles
$\phi_{vdw}$	J	Van der Waals potential

$\phi_{vdw\ s-p}$	J	Retarded Van der Waals potential for sphere-plate interaction
$\phi_{vdw\ s-s}$	J	Retarded Van der Waals potential for sphere-sphere interaction
$\theta$	-	Volumetric water content
$\theta_p$	rad	Particle contact angle
$\theta_r$	-	Residual volumetric water content
$\theta_s$	-	Volumetric water content at saturation
$\theta_2$	rad	Second surface contact angle

## LATIN LETTERS

PARAMETER	DIMENSIONS	DESCRIPTION
$a$	-	System-specific constant in the hydrophobic potential equation
$a_1$	-	Parameter of the empirical equation for $k_a$
$a_2$	-	Parameter of the empirical equation for $k_a$
$a_2^{AWI}$	-	Parameter of the 3P model
$a_3$	-	Parameter of the empirical equation for $s_{\max}$
$a_3^{AWI}$	-	Parameter of the 3P model
$A_H$	J	Hamaker constant
$A_{ij}$	J	Hamaker constant of the interaction between two materials i and j in vacuum
$A_{132}$	J	Hamaker constant of the interaction between two materials 1 and 2 immersed in medium 3
$b$	-	System-specific constant in the hydrophobic potential equation
$b_1$	-	Parameter in the retarded equation of Van der Waals potential
$b_2$	-	Parameter in the retarded equation of Van der Waals potential
$C$	kg/L	Solute concentration
$c_0$	-	Parameter of the characterization equation of the ThetaProbes
$C_0$	kg/L	Solute concentration



$c_1$	-	Parameter of the characterization equation of the ThetaProbes
$c_2$	-	Parameter of the characterization equation of the ThetaProbes
$c_i$	mol/L	Ion concentration
$d$	m	Separation distance
$d_c$	m	Collector diameter
$d_m$	m <sup>2</sup> /s	Diffusion coefficient
$d_p$	m	Particle diameter
$D$	m <sup>2</sup> /s	Dispersive term in the CDE
$D_\infty$	m <sup>2</sup> /s	Einstein's molecular diffusion coefficient
$\hat{D}$	m <sup>2</sup> /s	Hydrodynamic tensor
$\hat{D}_L$	m <sup>2</sup> /s	longitudinal component of the hydrodynamic tensor
$\hat{D}_T$	m <sup>2</sup> /s	transverse component of the hydrodynamic tensor
$F_A$	N	Adhesive force
$F_H$	N	Drag force
$h$	m	Pressure head
$\mathbf{h}$	-	Vector of the simulated values
$\hat{\mathbf{h}}$	-	Vector of the measured values
$H$	m	Hydraulic head
$l$	-	Pore connectivity parameter in the in the van Genuchten-Mualem model
$m$	-	van Genuchten-Mualem model parameter
$n$	-	Pore size distribution index in the van Genuchten-Mualem model
$N$	-	Number of values in the inverse problem resolution
$np$	-	Number of parameters in the inverse problem resolution
$K(h)$	m/s	Hydraulic conductivity
$k_a$	s <sup>-1</sup>	Attachment coefficient
$k_a^{AWI}$	s <sup>-1</sup>	Attachment coefficient related to the AWI
$k_a^{sat}$	s <sup>-1</sup>	Attachment coefficient under saturated conditions
$k_a^{SWI}$	s <sup>-1</sup>	Attachment coefficient related to the SWI
$k_a^{uns}$	s <sup>-1</sup>	Attachment coefficient under unsaturated conditions
$k_{cal}$	s <sup>-1</sup>	Calculated attachment coefficient
$K_s$	m/s	Saturated hydraulic conductivity
$O$	-	Objective function
$p$	Pa	Water pressure in the pores of the porous medium
$\mathbf{p}$	-	Vector of the np parameters to be optimized
$p_a$	Pa	Atmospheric pressure
$q_{conv}$	kg/m <sup>2</sup> /s	Convective discharge

$q_D$	m/s	Darcy velocity
$q_{dif}$	kg/m <sup>2</sup> /s	Diffusive discharge
$q_{disp}$	kg/m <sup>2</sup> /s	Dispersive discharge
$R, R_1, R_2$	J	Particle radius
$s$	kg/kg	Particle concentration in the solid phase
$S$	-	Porous medium saturation
$S_e$	-	Porous medium effective saturation
$s_{max}$	kg/kg	Maximum retention capacity of the porous medium
$s_{max}^{AWI}$	kg/kg	Maximum retention capacity of the porous medium related to the AWI
$s_{max}^{sat}$	kg/kg	Maximum retention capacity of the porous medium under saturated conditions
$s_{max}^{SWI}$	kg/kg	Maximum retention capacity of the porous medium related to the SWI
$s_{max}^{uns}$	kg/kg	Maximum retention capacity of the porous medium under unsaturated conditions
$T_{adhesive}$	N m	Adhesive torque
$T_{hydrodynamic}$	N m	Hydrodynamic torque
$U$	V	output tension of the ThetaProbe
$v$	m/s	Pore water velocity
$V_t$	m <sup>3</sup>	Total volume of the porous medium
$V_w$	m <sup>3</sup>	Water volume contained in the porous medium
$z$	m	Soil depth
$z_i$	-	Ion's valence



---

## BIBLIOGRAPHY

---

- Abbaspour, K., R. Schulin, and M. van Genuchten (2001). "Estimating unsaturated soil hydraulic parameters using ant colony optimization." eng. *Advances in Water Resources* 24.8, pp. 827–841.
- Adam, V., S. Loyaux-Lawniczak, and G. Quaranta (2015). "Characterization of engineered TiO<sub>2</sub> nanomaterials in a life cycle and risk assessments perspective." *Environmental Science and Pollution Research*, pp. 1–18.
- Adamczyk, Z., B. Siwek, M. Zembala, and P. Belouschek (1994). "Kinetics of localized adsorption of colloid particles." *Advances in Colloid and Interface Science* 48, pp. 151–280. DOI: [http://dx.doi.org/10.1016/0001-8686\(94\)80008-1](http://dx.doi.org/10.1016/0001-8686(94)80008-1).
- Anders, R. and C. Chrysikopoulos (2009). "Transport of viruses through saturated and unsaturated columns packed with sand." *Transport in Porous Media* 76.1, pp. 121–138. DOI: [10.1007/s11242-008-9239-3](https://doi.org/10.1007/s11242-008-9239-3).
- Anders, R. and C. V. Chrysikopoulos (2005). "Virus fate and transport during artificial recharge with recycled water." *Water Resources Research* 41.10, W10415. DOI: [10.1029/2004WR003419](https://doi.org/10.1029/2004WR003419).
- Auffan, M., J. Rose, M. Wiesner, and J.-Y. Bottero (2009a). "Chemical stability of metallic nanoparticles: A parameter controlling their potential cellular toxicity in vitro." *Environmental Pollution* 157.4, pp. 1127–1133.
- Auffan, M., J. Rose, J.-Y. Bottero, G. Lowry, J.-P. Jolivet, and M. Wiesner (2009b). "Towards a definition of inorganic nanoparticles from an environmental, health and safety perspective." *Nature Nanotechnology* 4.10, pp. 634–641.
- Batley, G. E., J. K. Kirby, and M. J. McLaughlin (2011). "Fate and Risks of Nanomaterials in Aquatic and Terrestrial Environments." *Accounts of Chemical Research* 46.3, pp. 854–862. DOI: [10.1021/ar2003368](https://doi.org/10.1021/ar2003368).
- Bergstrom, L. (1997). "Hamaker constants of inorganic materials." *Advances in Colloid and Interface Science* 70.0, pp. 125–169. DOI: [http://dx.doi.org/10.1016/S0001-8686\(97\)00003-1](http://dx.doi.org/10.1016/S0001-8686(97)00003-1).

- Beydoun, H. and F. Lehmann (2006). "Drainage experiments and parameter estimation in unsaturated porous media." *Comptes Rendus - Geoscience* 338.3, pp. 180–187. DOI: [10.1016/j.crte.2005.12.004](https://doi.org/10.1016/j.crte.2005.12.004).
- Bradford, S. A., J. Simunek, M. Bettahar, M. T. van Genuchten, and S. R. Yates (2006). "Significance of straining in colloid deposition: Evidence and implications." *Water Resources Research* 42.12, W12S15. DOI: [10.1029/2005WR004791](https://doi.org/10.1029/2005WR004791).
- Bradford, S. and S. Torkzaban (2008). "Colloid transport and retention in unsaturated porous media: A review of interface-, collector-, and pore-scale processes and models." *Vadose Zone Journal* 7.2, pp. 667–681.
- Bradford, S., S. Torkzaban, and A. Shapiro (2013). "A theoretical analysis of colloid attachment and straining in chemically heterogeneous porous media." *Langmuir* 29.23, pp. 6944–6952.
- Bradford, S. A., S. Torkzaban, and J. Simunek (2011). "Modeling colloid transport and retention in saturated porous media under unfavorable attachment conditions." *Water Resources Research* 47.10, W10503.
- Brar, S., M. Verma, R. Tyagi, and R. Surampalli (2010). "Engineered nanoparticles in wastewater and wastewater sludge - Evidence and impacts." *Waste Management* 30.3, pp. 504–520.
- Camesano, T. A., M. U. Kenneth, and E. L. Bruce (1999). "Blocking and ripening of colloids in porous media and their implications for bacterial transport." *Colloids and Surfaces A: Physicochemical and Engineering Aspects* 160.3, pp. 291–307. DOI: [http://dx.doi.org/10.1016/S0927-7757\(99\)00156-9](http://dx.doi.org/10.1016/S0927-7757(99)00156-9).
- Chapman, D., Unesco, World Health Organization, and United Nations Environment Programme (1996). *Water Quality Assessments: A Guide to the Use of Biota, Sediments, and Water in Environmental Monitoring*. E & FN Spon.
- Chen, G., X. Liu, and C. Su (2011). "Transport and Retention of TiO<sub>2</sub> Rutile Nanoparticles in Saturated Porous Media under Low-Ionic-Strength Conditions: Measurements and Mechanisms." *Langmuir* 27.9, pp. 5393–5402. DOI: [10.1021/la200251v](https://doi.org/10.1021/la200251v).
- (2012). "Distinct Effects of Humic Acid on Transport and Retention of TiO<sub>2</sub> Rutile Nanoparticles in Saturated Sand Columns." *Environmental Science & Technology* 46.13, pp. 7142–7150. DOI: [10.1021/es204010g](https://doi.org/10.1021/es204010g).
- Chen, K. L. and M. Elimelech (2006). "Aggregation and Deposition Kinetics of Fullerene (C<sub>60</sub>) Nanoparticles." *Langmuir* 22.26, pp. 10994–11001. DOI: [10.1021/la062072v](https://doi.org/10.1021/la062072v).
- Chen, L., D. Sabatini, and T. Kibbey (2008). "Role of the air-water interface in the retention of TiO<sub>2</sub> nanoparticles in porous media during primary drainage." *Environmental Science & Technology* 42.6, pp. 1916–1921.

- (2010). “Retention and release of TiO<sub>2</sub> nanoparticles in unsaturated porous media during dynamic saturation change.” *Journal of Contaminant Hydrology* 118.3-4, pp. 199–207.
- Chowdhury, I., Y. Hong, R. Honda, and S. Walker (2011). “Mechanisms of TiO<sub>2</sub> nanoparticle transport in porous media: Role of solution chemistry, nanoparticle concentration, and flowrate.” *Journal of Colloid and Interface Science* 360.2, pp. 548–555.
- Chowdhury, I., D. M. Cwiertny, and S. L. Walker (2012). “Combined Factors Influencing the Aggregation and Deposition of nano-TiO<sub>2</sub> in the Presence of Humic Acid and Bacteria.” *Environmental Science & Technology* 46.13, pp. 6968–6976. DOI: [10.1021/es2034747](https://doi.org/10.1021/es2034747).
- Chrysikopoulos, C. and V. Syngouna (2014). “Effect of gravity on colloid transport through water-saturated columns packed with glass beads: Modeling and experiments.” *Environmental Science & Technology* 48.12, pp. 6805–6813.
- Corapcioglu, M. and H. Choi (1996). “Modeling colloid transport in unsaturated porous media and validation with laboratory column data.” *Water Resources Research* 32.12, pp. 3437–3449.
- Cornelis, G., L. Pang, C. Doolette, J. K. Kirby, and M. J. McLaughlin (2013). “Transport of silver nanoparticles in saturated columns of natural soils.” *Science of The Total Environment* 463-464, pp. 120–130. DOI: <http://dx.doi.org/10.1016/j.scitotenv.2013.05.089>.
- Costanza-Robinson, M. S. and M. L. Brusseau (2002). “Air-water interfacial areas in unsaturated soils: Evaluation of interfacial domains.” *Water Resources Research* 38.10, pp. 13–1–13–17. DOI: [10.1029/2001WR000738](https://doi.org/10.1029/2001WR000738).
- Crist, J., Y. Zevi, J. McCarthy, J. Throop, and T. Steenhuis (2005). “Transport and retention mechanisms of colloids in partially saturated porous media.” *Vadose Zone Journal* 4.1, pp. 184–195.
- Dane, J. and G. Topp (2002). *Methods of Soil Analysis Part - 4 Physical Methods: SSSA Book Series - 5*. Soil Science Society of America.
- Darbha, G. K., C. Fischer, J. Luetzenkirchen, and T. Schafer (2012). “Site-Specific Retention of Colloids at Rough Rock Surfaces.” *Environmental Science & Technology* 46.17, pp. 9378–9387. DOI: [10.1021/es301969m](https://doi.org/10.1021/es301969m).
- DeNovio, N., J. Saiers, and J. Ryan (2004). “Colloid movement in unsaturated porous media: Recent advances and future directions.” *Vadose Zone Journal* 3.2, pp. 338–351.
- Derjaguin, B. and L. Landau (1941). “Theory of the stability of strongly charged lyophobic sols and of the adhesion of strongly charged particles in solutions of electrolytes.” *Acta Physicochimica URSS* 43, pp. 633–662. DOI: [http://dx.doi.org/10.1016/0079-6816\(93\)90013-L](http://dx.doi.org/10.1016/0079-6816(93)90013-L).

- Deutsch, W. and R. Siegel (1997). *Groundwater Geochemistry: Fundamentals and Applications to Contamination*. Taylor & Francis.
- El Badawy, A. M., A. Aly Hassan, K. G. Scheckel, M. T. Suidan, and T. M. Tolaymat (2013). "Key Factors Controlling the Transport of Silver Nanoparticles in Porous Media." *Environmental Science & Technology* 47.9, pp. 4039–4045. DOI: [10.1021/es304580r](https://doi.org/10.1021/es304580r).
- Elimelech, M. (1992). "Predicting collision efficiencies of colloidal particles in porous media." *Water Research* 26.1, pp. 1–8.
- Elimelech, M., J. Gregory, X. Jia, and R. A. Williams (1995). *Particle deposition & aggregation*. Butterworth-Heinemann. DOI: [http://dx.doi.org/10.1016/B978-075067024-1/50000-5](https://dx.doi.org/10.1016/B978-075067024-1/50000-5).
- Emmanuel, S. and B. Berkowitz (2005). "Mixing-induced precipitation and porosity evolution in porous media." *Advances in Water Resources* 28.4, pp. 337–344. DOI: [http://dx.doi.org/10.1016/j.advwatres.2004.11.010](https://dx.doi.org/10.1016/j.advwatres.2004.11.010).
- Fang, J., X. quan Shan, B. Wen, J. ming Lin, and G. Owens (2009). "Stability of titania nanoparticles in soil suspensions and transport in saturated homogeneous soil columns." *Environmental Pollution* 157.4, pp. 1101–1109. DOI: [10.1016/j.envpol.2008.11.006](https://doi.org/10.1016/j.envpol.2008.11.006).
- Fang, J., M. jia Xu, D. jun Wang, B. Wen, and J. yi Han (2013). "Modeling the transport of TiO<sub>2</sub> nanoparticle aggregates in saturated and unsaturated granular media: Effects of ionic strength and pH." *Water Research* 47.3, pp. 1399–1408. DOI: [10.1016/j.watres.2012.12.005](https://doi.org/10.1016/j.watres.2012.12.005).
- Freeze, R. A. and J. A. Cherry (1979). *Groundwater*. Hemel Hempstead: Prentice-Hall International.
- Godinez, I. and C. Darnault (2011). "Aggregation and transport of nano-TiO<sub>2</sub> in saturated porous media: Effects of pH, surfactants and flow velocity." *Water Research* 45.2, pp. 839–851.
- Godinez, I. G., C. J. Darnault, A. P. Khodadoust, and D. Bogdan (2013). "Deposition and release kinetics of nano-TiO<sub>2</sub> in saturated porous media: Effects of solution ionic strength and surfactants." *Environmental Pollution* 174.0, pp. 106–113. DOI: [10.1016/j.envpol.2012.11.002](https://doi.org/10.1016/j.envpol.2012.11.002).
- Gregory, J. (1981). "Approximate expressions for retarded van der waals interaction." *Journal of Colloid and Interface Science* 83.1, pp. 138–145. DOI: [http://dx.doi.org/10.1016/0021-9797\(81\)90018-7](https://dx.doi.org/10.1016/0021-9797(81)90018-7).
- Hamaker, H. (1937). "The London-van der Waals attraction between spherical particles." *Physica* 4.10, pp. 1058–1072.
- He, F., M. Zhang, T. Qian, and D. Zhao (2009). "Transport of carboxymethyl cellulose stabilized iron nanoparticles in porous media: Column experiments and modeling." *Journal of Colloid and Interface Science* 334.1, pp. 96–102.

- Hill, M. C. (1998). *Methods and Guidelines for Effective Model Calibration*. U.S. Geological Survey, Water-Resources Investigations Report 98-4005. DOI: [10.1061/40517\(2000\)18](https://doi.org/10.1061/40517(2000)18).
- Hillel, D. (1982). *Introduction to Soil Physics*. Academic Press Inc.
- Hogg, R., T. Healy, and D. Fuerstenau (1966). "Mutual coagulation of colloidal dispersions." *Transactions of the Faraday Society* 62, pp. 1638–1651.
- Huang, P. M., Y. Li, and M. E. Sumner (2012). *Handbook of Soil Sciences - Second Edition*. CRC Press.
- Israelachvili, J. N. (1985). *Intermolecular and Surface Forces*. Academic Press. DOI: <http://dx.doi.org/10.1016/B978-0-12-375182-9.10001-6>.
- Johnson, W. P., X. Li, and G. Yal (2007). "Colloid Retention in Porous Media: Mechanistic Confirmation of Wedging and Retention in Zones of Flow Stagnation." *Environmental Science & Technology* 41.4, pp. 1279–1287. DOI: [10.1021/es061301x](https://doi.org/10.1021/es061301x).
- Johnston, R. L. (2012). "Chapter 1 - Metal Nanoparticles and Nanoalloys." *Metal Nanoparticles and Nanoalloys*. Vol. 3. Frontiers of Nanoscience. Elsevier. Chap. 1, pp. 1–42. DOI: [10.1016/B978-0-08-096357-0.00006-6](https://doi.org/10.1016/B978-0-08-096357-0.00006-6).
- Kahru, A. and H.-C. Dubourguier (2010). "From ecotoxicology to nanoecotoxicology." *Toxicology* 269.2-3, pp. 105–119. DOI: <http://dx.doi.org/10.1016/j.tox.2009.08.016>.
- Kim, C. and S. Lee (2014). "Effect of seepage velocity on the attachment efficiency of TiO<sub>2</sub> nanoparticles in porous media." *Journal of Hazardous Materials* 279.0, pp. 163–168. DOI: <http://dx.doi.org/10.1016/j.jhazmat.2014.06.072>.
- Knappenberger, T., M. Flury, E. D. Mattson, and J. B. Harsh (2014). "Does Water Content or Flow Rate Control Colloid Transport in Unsaturated Porous Media?" *Environmental Science & Technology* 48.7, pp. 3791–3799. DOI: [10.1021/es404705d](https://doi.org/10.1021/es404705d).
- Kumahor, S. K., P. Hron, G. Metreveli, G. E. Schaumann, and H.-J. Vogel (2015). "Transport of citrate-coated silver nanoparticles in unsaturated sand." *Science of The Total Environment* 0. DOI: <http://dx.doi.org/10.1016/j.scitotenv.2015.03.023>.
- Lanphere, J., C. Luth, and S. Walker (2013). "Effects of solution chemistry on the transport of graphene oxide in saturated porous media." *Environmental Science & Technology* 47.9, pp. 4255–4261.
- Lazouskaya, V., L.-P. Wang, H. Gao, X. Shi, K. Czymmek, and Y. Jin (2011). "Pore-scale investigation of colloid retention and mobilization in the presence of a moving air-water interface." *Vadose Zone Journal* 10.4, pp. 1250–1260.



- Lecoanet, H., J.-Y. Bottero, and M. Wiesner (2004). "Laboratory assessment of the mobility of nanomaterials in porous media." *Environmental Science & Technology* 38.19, pp. 5164–5169.
- Lenhart, J. and J. Saiers (2002). "Transport of silica colloids through unsaturated porous media: Experimental results and model comparisons." *Environmental Science & Technology* 36.4, pp. 769–777.
- Li, Z., E. Sahle-Demessie, A. Hassan, and G. Sorial (2011). "Transport and deposition of CeO<sub>2</sub> nanoparticles in water-saturated porous media." *Water Research* 45.15, pp. 4409–4418.
- Liang, Y., S. Bradford, J. Simunek, M. Heggen, H. Vereecken, and E. Klumpp (2013a). "Retention and remobilization of stabilized silver nanoparticles in an undisturbed loamy sand soil." *Environmental Science & Technology* 47.21, pp. 12229–12237.
- Liang, Y., S. A. Bradford, J. Simunek, H. Vereecken, and E. Klumpp (2013b). "Sensitivity of the transport and retention of stabilized silver nanoparticles to physicochemical factors." *Water Research* 47.7, pp. 2572–2582. DOI: [10.1016/j.watres.2013.02.025](https://doi.org/10.1016/j.watres.2013.02.025).
- Lin, D., X. Tian, F. Wu, and B. Xing (2010). "Fate and transport of engineered nanomaterials in the environment." *Journal of Environmental Quality* 39.6, pp. 1896–1908.
- Liu, Y. (2010). "Elimination de nanoparticules d'effluents liquides." PhD thesis. INSA Toulouse.
- Lowry, G. V., K. B. Gregory, S. C. Apte, and J. R. Lead (2012). "Transformations of Nanomaterials in the Environment." *Environmental Science & Technology* 46.13, pp. 6893–6899. DOI: [10.1021/es300839e](https://doi.org/10.1021/es300839e).
- Lyklema, J (2005). "The bottom size of colloids." *Technical Sciences* 53.4.
- Ma, H., J. Pedel, P. Fife, and W. P. Johnson (2009). "Hemispheres-in-Cell Geometry to Predict Colloid Deposition in Porous Media." *Environmental Science & Technology* 43.22, pp. 8573–8579. DOI: [10.1021/es901242b](https://doi.org/10.1021/es901242b).
- Maraqa, M. A., R. B. Wallace, and T. C. Voice (1997). "Effects of degree of water saturation on dispersivity and immobile water in sandy soil columns." *Journal of Contaminant Hydrology* 25.3-4, pp. 199–218. DOI: [http://dx.doi.org/10.1016/S0169-7722\(96\)00032-0](http://dx.doi.org/10.1016/S0169-7722(96)00032-0).
- Marquardt, D. W. (1963). "An algorithm for least-squares estimation of nonlinear parameters." *Journal of the Society for Industrial & Applied Mathematics* 11.2, pp. 431–441.
- Mitropoulou, P. N., V. I. Syngouna, and C. V. Chrysikopoulos (2013). "Transport of colloids in unsaturated packed columns: Role of ionic strength and sand grain size." *Chemical Engineering Journal* 232.0, pp. 237–248. DOI: <http://dx.doi.org/10.1016/j.cej.2013.07.093>.

- Najafi, A. S., J. Drelich, A. Yeung, Z. Xu, and J. Masliyah (2007). “A novel method of measuring electrophoretic mobility of gas bubbles.” *Journal of Colloid and Interface Science* 308.2, pp. 344–350. DOI: <http://dx.doi.org/10.1016/j.jcis.2007.01.014>.
- Navarro, E., F. Piccapietra, B. Wagner, F. Marconi, R. Kaegi, N. Odzak, L. Sigg, and R. Behra (2008). “Toxicity of Silver Nanoparticles to *Chlamydomonas reinhardtii*.” *Environmental Science & Technology* 42.23, pp. 8959–8964. DOI: [10.1021/es801785m](http://dx.doi.org/10.1021/es801785m).
- Nowack, B. and T. D. Bucheli (2007). “Occurrence, behavior and effects of nanoparticles in the environment.” *Environmental Pollution* 150.1, pp. 5–22. DOI: <http://dx.doi.org/10.1016/j.envpol.2007.06.006>.
- Nutzmann, G., S. Maciejewski, and K. Joswig (2002). “Estimation of water saturation dependence of dispersion in unsaturated porous media: experiments and modelling analysis.” *Advances in Water Resources* 25.5, pp. 565–576. DOI: [http://dx.doi.org/10.1016/S0309-1708\(02\)00018-0](http://dx.doi.org/10.1016/S0309-1708(02)00018-0).
- Ouyang, G., K. Wang, and X. Y. Chen (2012). “TiO<sub>2</sub> nanoparticles modified polydimethylsiloxane with fast response time and increased dielectric constant.” *Journal of Micromechanics and Microengineering* 22.7, p. 074002.
- Petosa, A., S. Brennan, F. Rajput, and N. Tufenkji (2012). “Transport of two metal oxide nanoparticles in saturated granular porous media: Role of water chemistry and particle coating.” *Water Research* 46.4, pp. 1273–1285.
- Praetorius, A., M. Scheringer, and K. Hungerbühler (2012). “Development of Environmental Fate Models for Engineered Nanoparticles - A Case Study of TiO<sub>2</sub> Nanoparticles in the Rhine River.” *Environmental Science & Technology* 46.12, pp. 6705–6713. DOI: [10.1021/es204530n](http://dx.doi.org/10.1021/es204530n).
- Press, W. H., S. A. Teukolsky, W. T. Vetterling, and B. P. Flannery (1992). *Numerical recipes in Fortran 77: the art of scientific computing*. Cambridge University Press.
- Quik, J., I. Velzeboer, M. Wouterse, A. Koelmans, and D. van de Meent (2014). “Heteroaggregation and sedimentation rates for nanomaterials in natural waters.” *Water Research* 48.0, pp. 269–279. DOI: <http://dx.doi.org/10.1016/j.watres.2013.09.036>.
- Redman, J., S. Walker, and M. Elimelech (2004). “Bacterial Adhesion and Transport in Porous Media: Role of the Secondary Energy Minimum.” *Environmental Science & Technology* 38.6, pp. 1777–1785.
- Riva, M., M. Panzeri, A. Guadagnini, and S. P. Neuman (2011). “Role of model selection criteria in geostatistical inverse estimation of statistical data- and model-parameters.” *Water Resources Research* 47.7, W07502. DOI: [10.1029/2011WR010480](http://dx.doi.org/10.1029/2011WR010480).

- Roadcap, G. S., W. R. Kelly, and C. M. Bethke (2005). "Geochemistry of Extremely Alkaline (pH > 12) Ground Water in Slag-Fill Aquifers." *Groundwater* 43.6, pp. 806–816.
- Roth, K. (2012). *Soil Physics Lecture Notes*. Institute of Environmental Physics, Heidelberg University.
- Russo, D., W. A. Jury, and G. L. Butters (1989). "Numerical analysis of solute transport during transient irrigation: 1. The effect of hysteresis and profile heterogeneity." *Water Resource Research* 25.10, pp. 2109–2118. DOI: [doi : 10.1029/WR025i010p02109](https://doi.org/10.1029/WR025i010p02109).
- Ryan, J. N. and M. Elimelech (1996). "Colloid mobilization and transport in groundwater." *Colloids and Surfaces A: Physicochemical and Engineering Aspects* 107.0, pp. 1–56. DOI: [http://dx.doi.org/10.1016/0927-7757\(95\)03384-X](http://dx.doi.org/10.1016/0927-7757(95)03384-X).
- Schaap, M. G., F. J. Leij, and M. T. van Genuchten (2001). "ROSETTA: a computer program for estimating soil hydraulic parameters with hierarchical pedotransfer functions." *Journal of hydrology* 251.3, pp. 163–176.
- Schafer, A., H. Harms, and A. J. B. Zehnder (1998). "Bacterial Accumulation at the Air-Water Interface." *Environmental Science & Technology* 32.23, pp. 3704–3712. DOI: [10.1021/es980191u](https://doi.org/10.1021/es980191u).
- Shellenberger, K. and B. E. Logan (2002). "Effect of Molecular Scale Roughness of Glass Beads on Colloidal and Bacterial Deposition." *Environmental Science & Technology* 36.2, pp. 184–189. DOI: [10.1021/es015515k](https://doi.org/10.1021/es015515k).
- Shen, C., Y. Huang, B. Li, and Y. Jin (2010). "Predicting attachment efficiency of colloid deposition under unfavorable attachment conditions." *Water Resources Research* 46.11, W11526. DOI: [10.1029/2010WR009218](https://doi.org/10.1029/2010WR009218).
- Shen, C., Y. Jin, B. Li, W. Zheng, and Y. Huang (2014). "Facilitated attachment of nanoparticles at primary minima by nanoscale roughness is susceptible to hydrodynamic drag under unfavorable chemical conditions." *Science of The Total Environment* 466-467, pp. 1094–1102. DOI: <http://dx.doi.org/10.1016/j.scitotenv.2013.07.125>.
- Šimuněk, J., M. T. van Genuchten, and M. ě<sub>2</sub>ejna (2008). "Development and Applications of the HYDRUS and STANMOD Software Packages and Related Codes." *Vadose Zone Journal* 7.2, pp. 587–600. DOI: [10.2136/vzj2007.0077](https://doi.org/10.2136/vzj2007.0077).
- Šimuněk, J., R. Kodešová, M. M. Gribb, and M. T. van Genuchten (1999). "Estimating hysteresis in the soil water retention function from cone permeameter experiments." *Water Resources Research* 35.5, pp. 1329–1345.
- Solovitch, N., J. Labille, J. Rose, P. Chaurand, D. Borschneck, M. Wiesner, and J.-Y. Bottero (2010). "Concurrent aggregation and deposition of TiO<sub>2</sub> nanoparticles in a sandy porous media." *Environmental Science & Technology* 44.13, pp. 4897–4902.

- Tian, Y., B. Gao, C. Silvera-Batista, and K. Ziegler (2010). "Transport of engineered nanoparticles in saturated porous media." *Journal of Nanoparticle Research* 12.7, pp. 2371–2380.
- Toloni, I., F. Lehmann, and P. Ackerer (2014). "Modeling the effects of water velocity on TiO<sub>2</sub> nanoparticles transport in saturated porous media." *Journal of Contaminant Hydrology* 171.0, pp. 42–48. DOI: <http://dx.doi.org/10.1016/j.jconhyd.2014.10.004>.
- Topp, G. C., J. L. Davis, and A. P. Annan (1980). "Electromagnetic determination of soil water content: Measurements in coaxial transmission lines." *Water Resources Research* 16 (3), pp. 574–582. DOI: [10.1029/WR016i003p00574](https://doi.org/10.1029/WR016i003p00574).
- Toride, N., F. J. Leij, and M. T. van Genuchten (1995). *The CXTFIT code for estimating transport parameters from laboratory or field tracer experiments*. Version 2.0. Research Report No. 137, U. S. Salinity Laboratory, USDA, ARS, Riverside, CA.
- Torkzaban, S., S. A. Bradford, and S. L. Walker (2007). "Resolving the Coupled Effects of Hydrodynamics and DLVO Forces on Colloid Attachment in Porous Media." *Langmuir* 23.19, pp. 9652–9660. DOI: [10.1021/la700995e](https://doi.org/10.1021/la700995e).
- Torkzaban, S., S. A. Bradford, M. T. van Genuchten, and S. L. Walker (2008). "Colloid transport in unsaturated porous media: The role of water content and ionic strength on particle straining." *Journal of Contaminant Hydrology* 96.1â4, pp. 113–127. DOI: [10.1016/j.jconhyd.2007.10.006](https://doi.org/10.1016/j.jconhyd.2007.10.006).
- Tosco, T., J. Bosch, R. U. Meckenstock, and R. Sethi (2012). "Transport of Ferrihydrite Nanoparticles in Saturated Porous Media: Role of Ionic Strength and Flow Rate." *Environmental Science & Technology* 46.7, pp. 4008–4015. DOI: [10.1021/es202643c](https://doi.org/10.1021/es202643c).
- Tscharnuter, W. (2000). *Photon correlation spectroscopy in particle sizing*. Wiley Online Library.
- Tufenkji, N. and M. Elimelech (2004). "Correlation Equation for Predicting Single-Collector Efficiency in Physicochemical Filtration in Saturated Porous Media." *Environmental Science & Technology* 38.2, pp. 529–536.
- (2005a). "Breakdown of colloid filtration theory: Role of the secondary energy minimum and surface charge heterogeneities." *Langmuir* 21.3, pp. 841–852.
- Tufenkji, N. and M. Elimelech (2005b). "Reply to Comment on Breakdown of Colloid Filtration Theory: Role of the Secondary Energy Minimum and Surface Charge Heterogeneities." *Langmuir* 21.23, pp. 10896–10897. DOI: [10.1021/la051621e](https://doi.org/10.1021/la051621e).
- van Genuchten, M. T. (1980). "A Closed-form Equation for Predicting the Hydraulic Conductivity of Unsaturated Soils." *Soil Science Society of America Journal* 44.5, pp. 892–898.

- Vanderborght, J. and H. Vereecken (2007). “Review of dispersivities for transport modeling in soils.” *Vadose Zone Journal* 6.1, pp. 29–52.
- Verwey, E. J. W. and J. T. G. Overbeek (1948). *Theory of the stability of lyophobic colloids*. Elsevier.
- Visual Numerics (2014). *IMSL Fortran Numerical Library: User’s Guide. Version 7.0*.
- Vitorge, E., S. Szenknect, J. M. F. Martins, and J.-P. Gaudet (2013). “Size- and concentration-dependent deposition of fluorescent silica colloids in saturated sand columns: transport experiments and modeling.” *Environ. Sci.: Processes Impacts* 15 (8), pp. 1590–1600. DOI: [10.1039/C3EM30860J](https://doi.org/10.1039/C3EM30860J).
- Wang, C., A. D. Bobba, R. Attinti, C. Shen, V. Lazouskaya, L.-P. Wang, and Y. Jin (2012). “Retention and Transport of Silica Nanoparticles in Saturated Porous Media: Effect of Concentration and Particle Size.” *Environmental Science & Technology* 46.13, pp. 7151–7158. DOI: [10.1021/es300314n](https://doi.org/10.1021/es300314n).
- Wang, Y., Y. Li, J. Fortner, J. Hughes, L. Abriola, and K. Pennell (2008). “Transport and retention of nanoscale C60 aggregates in water-saturated porous media.” *Environmental Science & Technology* 42.10, pp. 3588–3594.
- Wollschlaeger, U., T. Pfaff, and K. Roth (2009). “Field-scale apparent hydraulic parameterisation obtained from TDR time series and inverse modelling.” *Hydrology and Earth System Sciences* 13.10, pp. 1953–1966.
- Yao, K.-M., M. Habibian, and C. O’Melia (1971). “Water and waste water filtration: Concepts and applications.” *Environmental Science & Technology* 5.11, pp. 1105–1112.
- Ye, M., P. D. Meyer, and S. P. Neuman (2008). “On model selection criteria in multimodel analysis.” *Water Resources Research* 44.3, W03428. DOI: [10.1029/2008WR006803](https://doi.org/10.1029/2008WR006803).
- Yoon, R.-H., D. Flinn, and Y. Rabinovich (1997). “Hydrophobic interactions between dissimilar surfaces.” *Journal of Colloid and Interface Science* 185.2, pp. 363–370. DOI: [10.1006/jcis.1996.4583](https://doi.org/10.1006/jcis.1996.4583).
- Yukselen-Aksoy, Y. and A. Kaya (2011). “A study of factors affecting on the zeta potential of kaolinite and quartz powder.” *Environmental Earth Sciences* 62.4, pp. 697–705. DOI: [10.1007/s12665-010-0556-9](https://doi.org/10.1007/s12665-010-0556-9).
- Zamani, A. and B. Mainibrownian (2009). “Flow of dispersed particles through porous media: Deep bed filtration.” *Journal of Petroleum Science and Engineering* 69.1&2, pp. 71 –88. DOI: <http://dx.doi.org/10.1016/j.petrol.2009.06.016>.
- Zhang, Q., S. M. Hassanizadeh, A. Raoof, M. T. van Genuchten, and S. M. Roels (2012). “Modeling virus transport and remobilization during transient partially saturated flow.” *Vadose Zone Journal* 11.2.

- Zhuang, J., J. S. Tyner, and E. Perfect (2009). "Colloid transport and remobilization in porous media during infiltration and drainage." *Journal of Hydrology* 377.1&2, pp. 112–119. DOI: <http://dx.doi.org/10.1016/j.jhydrol.2009.08.011>.



---

## CURRICULUM VITAE

---

### PERSONAL

**Ivan Toloni**

+33 (0) 368850538

ivan.toloni@etu.unistra.fr

toloni.ivan@gmail.com

Laboratory of Hydrology and Geochemistry of Strasbourg

University of Strasbourg / EOST, CNRS

1, rue Blessig

67000 Strasbourg

Born on August 27, 1986.

Italian Citizen.

### EDUCATION

**PhD in Earth Sciences, University of Strasbourg, 2015.**

*Thesis:* Transport of TiO<sub>2</sub> nanoparticles in saturated and unsaturated porous media: experiments and modeling

*Advisors:* Philippe Ackerer, François Lehmann

*Location:* Laboratory of Hydrology and Geochemistry of Strasbourg

*Funding:* French National Research Agency

**MSc in Environmental Physics, University of Milan, 2011.**

*Thesis:* Methodological and experimental study of the transport of nanoparticles in an unsaturated porous medium

*Advisor:* Mauro Giudici

*Internship:* Laboratory of Hydrology and Geochemistry of Strasbourg  
6 months

*Funding:* Erasmus Programme



**BSc in Physics, University of Milan - Bicocca, 2009.**

*Thesis:* Radioactivity analysis in liquid samples by  
evaporation residue

*Advisor:* Ezio Previtali

*Internship:* Department of Physics, University of Milan - Bicocca  
3 months

## PUBLICATIONS AND PRESENTATIONS

**Toloni, I.**, F. Lehmann, and P. Ackerer. “Transport of TiO<sub>2</sub> nanoparticles in unsaturated porous media: water content effects”. *In preparation*.

**Toloni, I.**, F. Lehmann, and P. Ackerer (2014). “Modeling the effects of water velocity on TiO<sub>2</sub> nanoparticles transport in saturated porous media”. *Journal of Contaminant Hydrology* 171.0, pp. 42-48.

**Toloni I.**, Lehmann F., Ackerer P. “Behaviour of TiO<sub>2</sub> nanoparticles in saturated porous media under different water velocities: measurements and modeling”. *Talk Presented to the European Geosciences Union - General Assembly 2014*. Vienna, Austria, May 2014.

**Toloni I.**, Lehmann F., Ackerer P. “Transport and retention of manufactured nanoparticles in water-saturated porous media under different conditions: measurements and modeling”. *Talk presented to TRePro III, Workshop on Modelling of Coupled Reactive and Transport Processes*. Karlsruhe, Germany, March 2014.

**Toloni I.**, Lehmann F., Ackerer P. “Water velocity effects on TiO<sub>2</sub> nanoparticle transport in porous media: measurements and modeling”. *Talk presented to the International Workshop on Nanoparticles in Soils and Waters: Fate, Transport and Effects*. Landau in der Pfalz, Germany, March 2014.

## EXPERIMENTAL SKILLS

**Technical:** Malvern Zetasizer, TDR probe, tensiometer probe, UV-spectrophotometer, sound level meter, semiconductor HpGe detector (basic).

**Topics:** nanoparticles, hydrology, porous media, environmental physics, air pollution, environmental radioactivity.

## INFORMATICS SKILLS

**Languages:** Fortran, C++, Python (basic)

**Software:** Origin, HYDRUS-1D, R, ROOT, LaTeX, JabRef

## LANGUAGE SKILLS

**Italian:** Mother tongue

**French:** Advanced professional proficiency (C1)

**English:** General professional proficiency (B2)

*TOEIC Listening and Reading score: 890/990, June 2015*

## REFERENCES

**Philippe Ackerer**

(PhD advisor)

LHyGeS

University of Strasbourg

1, rue Blessig

67084 Strasbourg Cedex

`ackerer@unistra.fr`

+33 (0) 3688550561

**Mauro Giudici**

(MSc thesis advisor)

Department of Earth Sciences

University of Milan

via Cicognara, 7

20129 Milano (MI)

`mauro.giudici@unimi.it`

+39 0250318478